Numerical modeling of long flexible fibers in inertial flows.

Deepak Kunhappan

Communauté
UNIVERSITÉ Grenoble Alpes

THÈSE

Pour obtenir le grade de

DOCTEUR DE LA COMMUNAUTE UNIVERSITE GRENOBLE ALPES

Spécialité : **Mécanique des fluides Energétique, Procédés**

Arrêté ministériel : 25 mai 2016

Présentée par

KUNHAPPAN Deepak

Thèse dirigée par **Guillaume BALARAC,** Maître de Conférences, Université Grenoble Alpes
et codirigée par **Pierre DUMONT,** Professeur**,** Université de Lyon,
Barthélémy HARTHONG, Maître de Conférences, Université Grenoble Alpes
et **Bruno CHAREYRE,** Maître de Conférences, Université Grenoble Alpes
préparée au sein du **Laboratoire des Ecoluments, Géophysiques et Industriels et Laboratoire Sols, Solides, Structures**
dans **l'École Doctorale I-MEP2 - Ingénierie - Matériaux, Mécanique, Environnement, Energétique, Procédés, Production**

Modélisation numérique de l'écoulement suspensions de fibres souples en régime inertiel

Numerical modeling of long flexible fibers in inertial flows

Thèse soutenue publiquement le **15 juin 2018**,
devant le jury composé de :

Monsieur Guillaume BALARAC
Maître de Conférences, Université Grenoble Alpes, Directeur de thèse
Monsieur Eric CLIMENT
Professeur, INP-ENSEEIHT, Institut de Mécanique des Fluides de Toulouse, Rapporteur
Monsieur Patrice LAURE
Directeur de Recherche, Centre National de la Recherche Scientifique, Nice, Rapporteur
Monsieur Franck NICOUD
Professeur, Université de Montpellier, Président du Jury
Monsieur Laurent ORGÉAS
Directeur de Recherche, Centre National de la Recherche Scientifique, Grenoble, Examinateur
Monsieur Pierre DUMONT
Professeur, Institut National des Sciences Appliquées es de Lyon, Co-directeur de thèse
Monsieur Barthélémy HARTHONG
Maître de Conférences, Université Grenoble Alpes, Invité
Monsieur Bruno CHAREYRE
Maître de Conférences, Université Grenoble Alpes, Invité

Abstract

A numerical model describing the behavior of flexible fibers under inertial flows was developed by coupling a discrete element solver with a finite volume solver. Each fiber is discretized into several beam segments, such that the fiber can bend, twist and rotate. The equations of the fiber motion were solved using a 2^{nd} order accurate explicit scheme (space and time). The three dimensional Navier-Stokes equations describing the motion of the fluid phase was discretized using a 4^{th} th order accurate (space and time) unstructured finite volume scheme. The coupling between the discrete fiber phase and the continuous fluid phase was obtained by a pseudo immersed boundary method as the hydrodynamic force on the fiber segments were calculated based on analytical expressions. Several hydrodynamic force models were analyzed and their validity and short-comings were identified. For Reynolds numbers (Re) at the inertial regime ($10^{-2} \leq Re \leq 10^2$, Re defined at the fiber scale), non linear drag force formulations based on the flow past an infinite cylinder was used. For rigid fibers in creeping flow, the drag force formulation from the slender body theory was used. A per unit length hydrodynamic torque model for the fibers was derived from explicit numerical simulations of shear flow past a high aspect ratio cylinder. The developed model was validated against several experimental studies and analytical theories ranging from the creeping flow regime (for rigid fibers) to inertial regimes. In the creeping flow regime, numerical simulations of semi dilute rigid fiber suspensions in shear were performed.The developed model was able to capture the fiber-fiber hydrodynamic and non-hydrodynamic interactions. The elasto-hydrodynamic interactions at finite Reynolds was validated with against two test cases. In the first test case, the deflection of the free end of a fiber in an uniform flow field was obtained numerically and the results were validated. In the second test case the conformation of long flexible fibers in homogeneous isotropic turbulence was obtained numerically and the results were compared with previous experiments. Two numerical studies were performed to verify the effects of the suspended fibers on carrier phase turbulence and the numerical model was able to reproduce the damping/enhancement phenomena of turbulence in channel and pipe flows as a consequence of the micro-structural evolution of the fibers.

Résumé

Un modèle numérique décrivant le comportement de fibres souples en suspension dans un écoulement de fluide en régime inertiel a été développé au moyen d'un couplage entre la méthode des éléments discrets et la méthode des volumes finis. Chaque fibre est discrétisée en plusieurs éléments de type poutre permettant de prendre en compte une déformation (flexion, torsion, allongement) et un mouvement de corps rigide. Les équations du mouvement des fibres sont résolues au moyen d'un schéma explicite du second ordre (temps et espace). Le mouvement de la phase fluide est décrit par les équations de Navier-Stokes, qui sont discrétisées et résolues au moyen d'un schéma aux volumes finis non structurés, d'ordre 4 (temps et espace). Le couplage entre la phase solide (discrète) et la phase fluide (continue) est obtenue par une pseudo méthode IBM (Immersed Boundary Method) dans laquelle l'effort hydrodynamique est calculé analytiquement. Plusieurs modèles de force hydrodynamique issus de la littérature sont analysés et leur validité ainsi que leurs limites sont identifiées. Pour des nombres de Reynolds (Re) correspondant au régime inertiel ($10^{-2} \leq Re \leq 10^2$, Re défini à l'échelle de la fibre), des formulations non-linéaires de la force hydrodynamique exercée par un écoulement uniforme sur un cylindre infini sont utilisées. Le couplage a aussi été utilisé pour des fibres rigides en écoulement de Stokes, en utilisant l'expression de la force de traînée issue de la théorie des corps élancés ('slender body theory'). Une expression du moment hydrodynamique par unité de longueur est obtenu à partir de simulations numériques par volumes finis de l'écoulement autour d'un cylindre élancé.

Le modèle développé a été validé par comparaison avec plusieurs résultats expérimentaux et analytiques, du régime de Stokes (pour des fibres rigides) jusqu'aux régimes inertiels. Dans

le cas du régime de Stokes, des simulations numériques du cisaillement de suspensions de fibres semi-diluées ont été réalisées. Le modèle développé permet de capturer les interactions hydrodynamiques et non-hydrodynamiques entre les fibres. Les interactions élasto-hydrodynamiques pour Re fini ont été validées dans deux cas. Dans le premier cas, la flèche d'une fibre encastrée-libre dans un écoulement uniforme a été obtenu par calcul numérique et le résultat validé par comparaison aux résultats expérimentaux de la littérature. Dans le second cas, la conformation de fibres élancées et très déformables dans un écoulement turbulent homogène et isotrope a été obtenu par calcul numérique et le résultat validé par comparaison aux résultats expérimentaux de la littérature. Deux études numériques ont été réalisées pour étudier l'effet de la présence de fibres en suspension sur la turbulence au sein du fluide suspensif. Le modèle numérique a permis de reproduire le phénomène de réduction/amplification de la turbulence dans un écoulement en canal ou en conduite, dû à l'évolution microstructurale de la phase fibreuse.

Acknowledgements

I would like to thank my supervisors (in alphabetical order) : Barthélémy, Bruno, Guillaume and Pierre for providing me the opportunity to pursue this thesis. This thesis had benefited greatly from their continuous valuable suggestions and advices. To be specific, Bart for his patience in answering my silly and fundamental questions on solid mechanics and Discrete Element Methods, Bruno for his guidance on the programming parts and working with YADE, Guillaume for teaching me turbulence and occasional help with the YALES2 code and Pierre in providing insights on the physics of fiber suspensions. Special thanks to Patrick (LEGI) for his advices and ideas on the code coupling, implementation and helping with the HPC facilities. Rémi (3SR) for assisting and solving the computer related issues during my time at 3SR lab. If it wasn't for these people, this thesis would not have materialized!

I would like to thank my office mates Abdelali and Aleksandr (Sasha) for the frequent entertainment, jokes, coffee breaks and discussions during the tough times. If it was not for these guys I would have lost my sanity long ago (that being said, you guys are still crazy!). Special thanks to Payam for listening to my complaints and cynical comments on almost everything, helping me with paper works and the french bureaucracy, I shall always remain indebted to you! Outside the lab, I would like to thank Keshav for the long thought provoking discussions with coffee and some other things, Hengdi for the weekend dinners, Didier for introducing me to the Metal scene at Grenoble and the weekly guitar jams, Brigitte for the french lessons. I would also like to thank Anish, Harsha, Joe, Vishwa, Mathew (G!), Vedaj and Godson for the frequent inquiries on my well being.

Finally I would like to thank my parents, my brother, my sister and my niece for their unconditional encouragement, love and support and for being with me all the time (I have no words to describe this). Thank you very much!

CONTENTS

CHAPTER 1

INTRODUCTION

Introduction

This thesis is mainly concerned with the numerical modeling of high aspect ratio flexible fibers in fluid flows. These fibers are usually long and thin, i.e, their length is many times greater than their width.

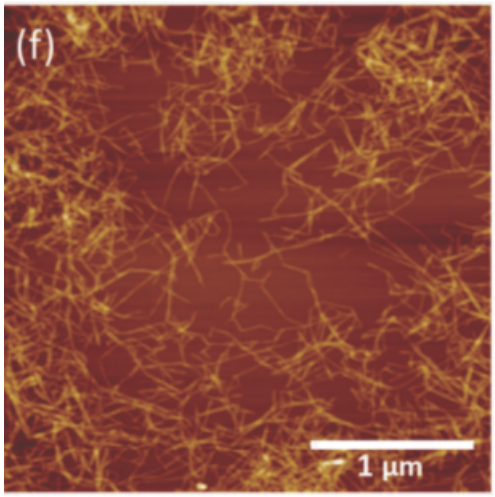

Figure 1.1: Optical micrograph (obtained from Atomic Force Microscopy (AFM)) of cellulose nanofibril suspension adapted from Martoïa *et al.* [111]

Figure 1.1 shows an optical micrograph of cellulose nanofibril suspension with 0.001% concentration by weight. This low concentration was used for imaging long cellulose nanofibrils and usually the suspensions are used with 1% volume concentration. From the figure one can notice the complex geometry of these slender fibers The flow of suspensions involving long flexible fibers are quite complex and arise in several industrial applications such as in the manufacturing of paper (pulp fibers) [106], bio based composite materials [50]. In addition to industrial applications, suspensions of long thin filaments are also encountered in several bio-physical phenomena, such as in cell division [118], swimming of microorganisms [90] and sperm cells [125]. In the manufacturing of composite materials involving fibers, the structure of the fiber network and the orientation distribution of the fibers (the microstructure) play a crucial role in the resulting mechanical properties of these composite materials. Figure 1.2 from Dumont *et al.* [51] shows the resulting fiber microstructure of bundle fiber suspensions after compression tests. The fiber

volume fraction is 0.15 (15%) and two specimens were considered : one with a random initial in-plane (in the e_1 direction) microstructure ($A_{11}^{init} \approx 0.5$) and oriented in-plane microstructure $A_{11}^{init} \approx 0.6$. The parameter A^{init} is the initial fiber orientation tensor. From the figure it is observed that the suspension with preferential orientation exhibit lower axial Cauchy stress. The deformed specimens are shown in the right hand side of figure.

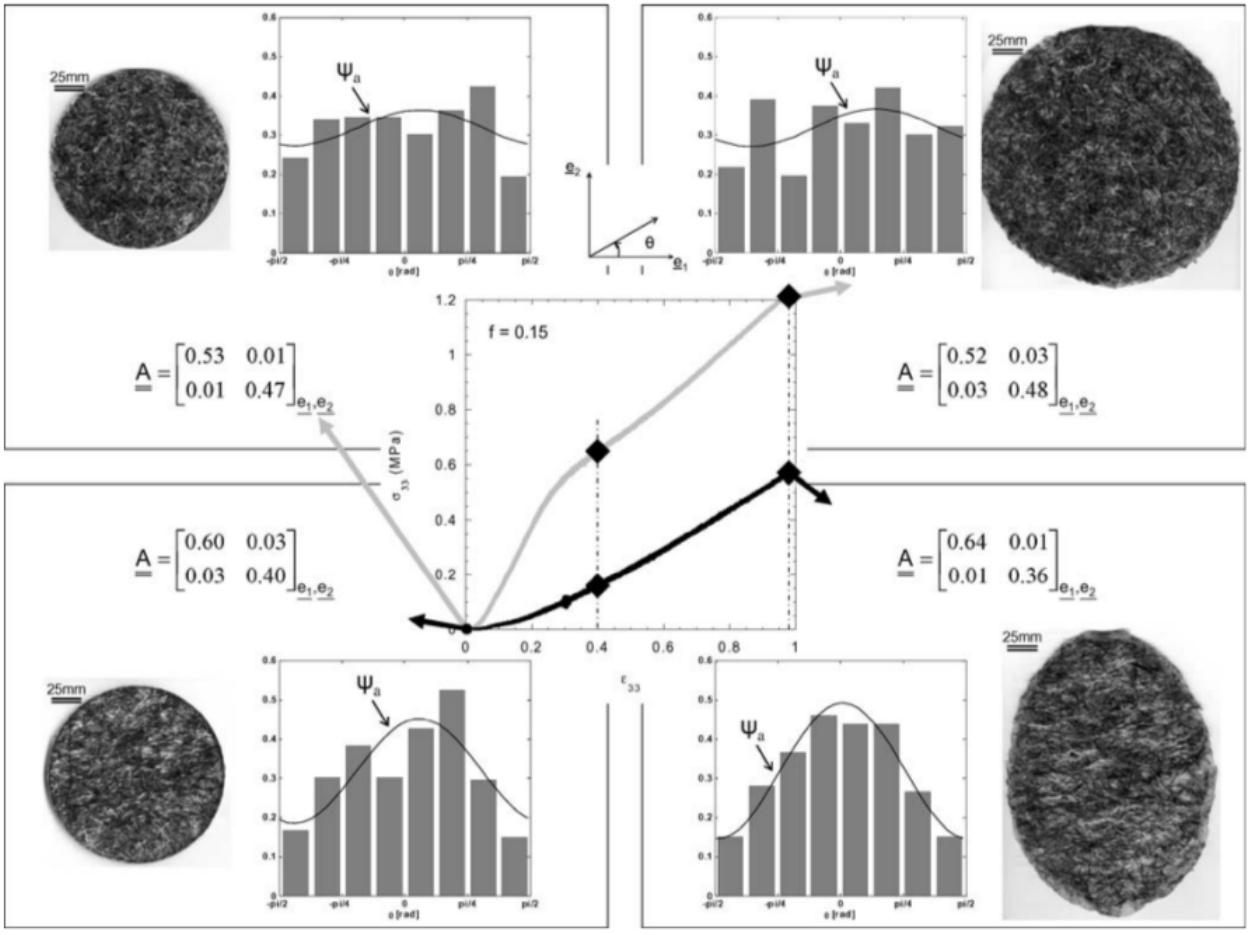

Figure 1.2: Fiber microstructure after compression tests of two samples of bundle fiber suspensions. Two specimens with initial random ($A_{11}^{init} \approx 0.5$, upper part) and oriented ($A_{11}^{init} \approx 0.6$, lower part) microstructures. The graph at the center gives the recorded axial Cauchy stress and logarithmic strains. Adapted from Dumont *et al.* [51]

Furthermore it is necessary to understand the key mechanisms on the formation of clusters within in fiber networks i.e. floc formation. Another interesting phenomena in these complex flows is the deformation of the suspended fibers, that is there is an elasto-hydrodynamic interaction between the suspended fibers and carrier flow and how the fiber networks in turn affect the flow behavior of the carrier phase.

Objectives

The objective of this thesis is to develop a numerical model through which can one can study the flow of suspensions of fibers for variety of flow situations. In this thesis, the fibers are considered as discrete Lagrangian beams that can deform and the fluid phase is considered as an Eulerian field. The motion and mechanical behaviour of the discrete fiber beams are modeled using an Discrete Element (DEM) solver and the Navier-Stokes equations governing the fluid motion

are solved using a Finite Volume solver (FVM). The fiber-fiber hydrodynamic and mechanical interactions and the fluid-fiber hydrodynamic force and torque are taken into account in the fiber mechanical model. The resulting hydrodynamic force from the fiber is introduced into the Navier-Stokes equations as line force distribution.

Thesis outline

- Chapter 2 introduces the concept of hydrodynamic force and torque on non-spherical particles. The scales of motion in the particle phase and the fluid phase are explained. The Chapter closes with a brief review on the computational methods for modeling particle laden multiphase flows.
- Chapter 3 introduces the solvers used in the present study. This Chapter primarily deals with the description of the numerical methods and schemes used in the present study. The governing equations of the fiber motion and its discretization are presented, followed by a section on the finite volume discretization. Finally the coupling methodology between the solvers developed in this study is presented.
- Discussion on three types of hydrodynamic force models and their shortcomings such as the effect of the fiber discretization and the validity of the force models in the stokesian and inertial regimes are explained in Chapter 4. First part of this Chapter presents basic results obtained from a commonly used (the prolate spheroid model) hydrodynamic force model for low Reynolds number flows (at the fiber scale). The remaining part of the Chapter deals with examination of previously derived analytical expressions for the hydrodynamic force for various Reynolds numbers (at the fiber scale). In the last section of the Chapter, a hydrodynamic torque model based on a 'per unit length' fashion has been originally formulated from explicit numerical simulations of a slender cylinder in shear flow.
- Chapter 5 consists of validation studies of the coupled numerical method. These studies are performed in the inertial regime (finite Reynolds number at the fiber scale.). The validation tests include :
  - Uniform flow past a high aspect ratio fiber with one of its ends fixed with the other end free to bend. The numerically obtained deflection is compared with previous experimental results and an analytical expression.
  - The conformation of flexible fibers in homogeneous isotropic turbulent flow. The results are compared with experimental studies.
  - Turbulent channel flow of concentrated (volume fraction = 1%) fiber suspension. The numerically obtained flow behavior is compared with experimental results.
- In Chapter 6 numerical study on the rheological behavior of semi-dilute suspensions of rigid fibers are presented. In this Chapter, a Stokesian force model is used to describe the hydrodynamic interaction between the fiber and the fluid. The developed model is validated against available analytical theories and experimental studies hence validating the developed coupled numerical model at low Reynolds numbers.
- Chapter 7 deals with the numerical study of turbulent pipe flow of semi dilute fiber suspensions. Preliminary qualitative results on the drag reducing effects the suspension are presented
- Chapter 8 gives an overall conclusion of the present work, discussing possible improvements and drawbacks of the developed coupled numerical model.

CHAPTER 2

REVIEW OF COMPUTATIONAL METHODS FOR PARTICULATE MULTIPHASE FLOWS

Contents

2.1 Introduction

The present Chapter gives an introduction to the field of particulate multiphase flow in the context of fiber suspension flows. Some important results and historical development in the field of microhydrodynamics are presented, in particular the drag force on spherical and spheroidal particles in Stokes flows. The properties, theorems and solution methods to Stokes flow problems have been omitted and for such details, the reader is advised to see the following references [88, 66, 64]. In the next part, popular methods used for the numerical study of multiphase particulate flows are presented. The Chapter closes with discussion on the modelling of fiber suspensions and rheological and microstructural behaviour of rigid non Brownian fiber suspensions.

2.2 Microhydrodynamics

The motion of a particle suspended in a quiescent fluid is governed by the hydrodynamic force exerted by the fluid on the particle boundaries, the equation of motion for an incompressible fluid (Navier-Stokes equations) reads as

$$\nabla \cdot \vec{U}_f = 0 \tag{2.1a}$$

where in equation (2.1a) is the incompressibility constraint, $\vec{U}_f$ is the fluid velocity. The momentum equation reads as

$$\frac{\partial \vec{U}_f}{\partial t} + \vec{\nabla}\left(\vec{U}_f \otimes \vec{U}_f\right) = -\frac{\vec{\nabla} P}{\rho} + \nu \vec{\nabla}^2 \vec{U}_f \tag{2.1b}$$

where, ρ is the fluid density, p the pressure and ν the kinematic viscosity of the fluid.
In order to characterize the effects of particle inertia suspended in the fluid, two non-dimensional numbers viz. the Stokes (St) and particle Reynolds number (Re_p) are frequently used. The Stokes number is defined as

$$St = \frac{|\vec{U}_f|\tau_p}{l_p}, \tag{2.2}$$

where in equation (2.2) l_p is the characteristic length scale of the particle and τ_p is the particle relaxation time:

$$\tau_p \propto \frac{\rho_p l_p^2}{\mu_f}. \tag{2.3}$$

The Reynolds number is defined as

$$Re_p = \frac{|U_f| l_p}{\nu}. \tag{2.4}$$

The Reynolds number is the ratio of inertial forces to viscous forces, and the Stokes number is defined as the ratio of characteristic time scale of the suspended particle to the characteristic time scale of the fluid flow. For low Stokes numbers ($St << 1$), the suspended particle follow the streamlines of the flow and for higher St, the particles detach from the flow and do not necessarily follow the fluid streamlines. When the particle Reynolds number is very small ($Re << 1$) the equation (2.1b) can be simplified by neglecting the convective and transient part to obtain linear Stokes equation, hence

$$\frac{\vec{\nabla} P}{\rho} = \nu \vec{\nabla}^2 \vec{U}_f \tag{2.5}$$

Since the Stokes equations are linear (2.5), it is possible to derive analytical solutions by the use of several mathematical methods such as Green's functions [80, 66] or by boundary integral methods [186] and singularity methods [131]. Stokes [159] derived the frictional resistance or the 'drag' force experienced by a sphere having radius r moving in a quiescent fluid, the expression reads as

$$\vec{F}_{\mathrm{d}} = 6\pi\mu r \vec{U}_f. \tag{2.6}$$

For a rigid spherical particle suspended in an unbounded Newtonian quiescent fluid, Faxén [57] derived general expressions for the force and torque relating to the particle translational and rotational velocity

$$\vec{F}_{\mathrm{hyd}} = 6\pi\mu r \left[\left(1 + \frac{r^2}{6}\vec{\nabla}^2\right)\vec{u}' - (\vec{U} - \vec{U}_f^{\infty})\right] \tag{2.7a}$$

$$\vec{T}_{\mathrm{hyd}} = 8\pi\mu r^3 \left[\frac{1}{2}\left(\vec{\nabla} \times \vec{u}'\right) - \left(\vec{\Omega} - \vec{\Omega}_f^{\infty}\right)\right] \tag{2.7b}$$

where in equations (2.7a) and (2.7b), $\vec{u}'$ is the disturbance velocity caused by the particle.
Batchelor [14] extended Faxén's law by the concept of stresslet. The stresslet $\mathbf{S}$ is the symmetric part of the first moment of force [64]. The stresslet relates the stress induced by the particles in the suspesnion [64], it is in fact the resistance of the particle deformation in strainig motion. The equation for the stresslet for a sphere is:

$$\mathbf{S} = \frac{10}{3}\left[2\mathbf{E}^{\infty} + \left(1 + \frac{1}{10}r^2\vec{\nabla}^2\right)(\vec{\nabla}\vec{u}' + (\vec{\nabla}\vec{u}')^{\mathrm{T}})\right]. \tag{2.8}$$

Jeffery [70] derived equations of motion for a neutrally buoyant ellipsoid in an unbounded stokes flow. For an ellipsoid having b as the length of the semi-minor axis, and a as the semi-major axis, with aspect ratio r_p defined as a/b, the time period of rotation for the ellipsoid immersed in a shear flow at $Re \to 0$ is

$$t_p = \frac{2\pi\dot{\gamma}}{r_p + \frac{1}{r_p}} \tag{2.9}$$

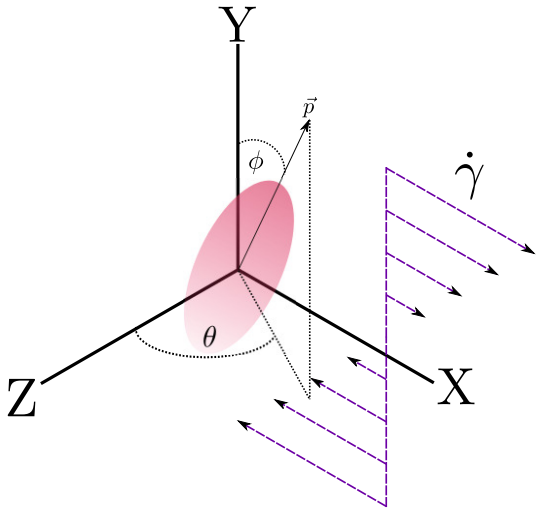

Figure 2.1: Rotation of a spheroidal object in shear flow (shear in XY plane).

In equation (2.9), $\dot{\gamma}$ is the shear rate (see figure 2.1). Considering $\vec{p}$ being the orientation vector of the symmetric axis of the ellipsoid, ϕ and θ being the angles $\vec{p}$ makes with velocity gradient direction and vorticity direction (see fig. 2.1), the expressions for the angular velocity of the ellipsoid is

$$\frac{d\phi}{dt} = \frac{\dot{\gamma}}{r_p^2 + 1}(r_p^2\cos^2\phi + \sin^2\phi) \tag{2.10}$$

$$\frac{d\theta}{dt} = \frac{\dot{\gamma}}{4}\left(\frac{r_p^2 - 1}{r_p^2 + 1}\right)\sin 2\theta \sin 2\phi \tag{2.11}$$

with the angles ϕ and θ given as

$$\tan\phi = r_p \tan\left(\frac{\dot{\gamma}t}{r_p + \frac{1}{r_p}} + k\right) \tag{2.12}$$

$$\tan\theta = \frac{Cr_p}{\sqrt{r_p^2\cos^2\phi + \sin^2\phi}} \tag{2.13}$$

where C and k are constants depending upon the initial orientation of the ellipsoid.
In addition to the motion of the ellipsoid in a quiscent fluid, Jeffery derived an expression for the effective viscosity for a dilute suspension of spheroidal particles largely influenced from Einstein's work [56]. Concerning cylindrical particles, Burgers [30] derived the hydrodynamic force and torque constants on a cylindrical particle, drawing inspiration from the work of Oberbeck [120].

Burgers had postulated that the disturbance induced by a long ellipsoid of revolution could be represented as a line force of magnitude acting along the axis of symmetry of the particle. Broersma [26, 27] improved the work of Burgers [30], however the results of both Burgers and Broersma were not asymptotically accurate. Mason and co-workers [167, 112] experimentally showed that neutrally buoyant rigid rod like particles tend to follow orbits similar to Jeffery orbits and in fact the expression (2.9)- (2.13) could be used for the prediction of the motion provided that the aspect ratio of the rod r_p is replaced by an effective aspect ratio r_e, ($r_e = 0.8r_p$). Bretherton [24] theoretically showed that the motion of axisymmetrical particles would exhibhit motion similar to Jeffery's predictions. Cox [41] by the method of Matched Asymptotic Expansions (MAE) derived the transverse and axial force per unit length on a high aspect aspect ratio cylindrical particle known as the slender body theory. Batchelor [12] extended the formualtion of Cox for slender bodies with non-circular cross sections. The slender body theory was further improved by Keller and Rubinow [77] and later Johnson [71] introduced a non local drag formulation in the slender body theory.

2.2.1 Resistance and Mobility Tensors

The solution to microhydrodynamics problems can be classified into two types : the resistance problem and the mobility problem. In the resistance problem, the fluid and particle velocities are set as the boundary conditions and one seeks for the hydrodynamic force, torque and stresslet the fluid applies on the particle [23].

$$\begin{pmatrix} \vec{F}_{\text{hyd}} \\ \vec{T}_{\text{hyd}} \\ \boldsymbol{S}_{\text{hyd}} \end{pmatrix} = \mu \begin{pmatrix} \boldsymbol{A} & \boldsymbol{B} & \boldsymbol{G} \\ \boldsymbol{B} & \boldsymbol{C} & \boldsymbol{H} \\ \boldsymbol{G} & \boldsymbol{H} & \boldsymbol{M} \end{pmatrix} \cdot \begin{pmatrix} \vec{U}_f - \vec{U}_p \\ \vec{\Omega}_f - \vec{\Omega}_p \\ \boldsymbol{E}_\infty \end{pmatrix} \tag{2.14}$$

where in equation (2.14) $\boldsymbol{A}$, $\boldsymbol{B}$, and $\boldsymbol{C}$ are second rank tensors, $\boldsymbol{G}$ and $\boldsymbol{H}$ are third order tensors and $\boldsymbol{M}$ is a fourth order tensor, μ is the fluid dynamic viscosity. The square matrix in (2.14) is usually known as the 'grand resistance' matrix. Expanding the equation (2.14), leads to the following set of expressions [23]. The expression of the hydrodynamic force on the particle reads as

$$F_{\text{hyd}i} = \mu \left[A_{ij} \left(U_j^f - U_j^p \right) + \tilde{B}_{ij} \left(\Omega_j^f - \Omega_j^p \right) + G_{ijk} E_{jk}^\infty \right] \tag{2.15}$$

The expression for the hydrodynamic torque reads as:

$$T_{\text{hyd}i} = \mu \left[B_{ij} \left(U_j^f - U_j^p \right) + C_{ij} \left(\Omega_j^f - \Omega_j^p \right) + H_{ijk} E_{jk}^\infty \right] \tag{2.16}$$

and the expression for the particle stresslet is

$$S_{\text{hyd}ij} = \mu \left[G_{ijk} \left(U_k^f - U_k^p \right) + H_{ijk} \left(\Omega_k^f - \Omega_k^p \right) + M_{ijkl} E_{kl}^\infty \right] \tag{2.17}$$

The tensors appearing in equations (2.14) to (2.17) are called the hydrodynamic resistance tensors. The hydrodynamic resistance tensors can be derived for any particle and it primarily depends upon the particle size and shape. The derivation of resistance tensors has been presented in the works of Brenner. In ref [21, 22], Brenner presents the method of derivation and in ref [23], the hydrodynamic resistance tensors of various slender axissymmetric particles have been presented. Furthermore, analytical expressions for the specific viscosity, rotary diffusion and other microstructural properties of Newtonian suspensions (dilute to semi-dilute) regime has been reviewed.

The mobility problem aims to derive the solution of the particle motion in response to prescribed forces and torques under an ambient flow. Based on the linearity of the Stokes equations, equation (2.14) can be written as

$$\begin{pmatrix} \vec{U}_f - \vec{U}_p \\ \vec{\Omega}_f - \vec{\Omega}_p \\ \mu^{-1}\boldsymbol{S} \end{pmatrix} = \begin{pmatrix} \boldsymbol{a} & \boldsymbol{b} & \boldsymbol{g} \\ \boldsymbol{b} & \boldsymbol{c} & \boldsymbol{h} \\ \boldsymbol{g} & \boldsymbol{h} & \boldsymbol{m} \end{pmatrix} \cdot \begin{pmatrix} \mu^{-1}\vec{F}_{\text{hyd}} \\ \mu^{-1}\vec{T}_{\text{hyd}} \\ \boldsymbol{E}^{\infty} \end{pmatrix} \tag{2.18}$$

where in equation (2.18), $\boldsymbol{a}$, $\boldsymbol{b}$ and $\boldsymbol{c}$ are second order tensors. $\boldsymbol{g}$ and $\boldsymbol{h}$ are third order tensors. $\boldsymbol{m}$ is a fourth order tensor. The square matrix in the righjt hand side of (2.18) is called the mobility matrix. The components of the mobility matrix can be derived from the resistance matrix, for details see [80] pages 109-115.

2.2.2 Higher Reynolds numbers

The formulation of hydrodynamic forces and torques presented in the previous section are only valid in the Stokes regime. Furthermore, the drag force on an infinite cylinder in the limit of low Reynolds numbers ($Re \to 0$) cannot be derived using the Stokes equations (Stokes paradox) [88]. In this section we discuss some of the analytical and empirical expressions for the hydrodynamic forces and torques on spherical and non-spherical particles when the particle Reynolds numbers are in the inertial regime. Oseen [121] derived an expression for the hydrodynamic force on a sphere for finite inertia. The solution was derived by linearizing the convective part of the NS equations,

$$U_{x_1}\frac{\partial u_i}{\partial x_1} = -\frac{1}{\rho}\frac{\partial p}{\partial x_i} + \nu\frac{\partial^2 u_i}{\partial x_j \partial x_j} \tag{2.19}$$

where in eqaution (2.19) U_{x_1} is the uniform velocity in the stream-wise direction (x_1), far from the particle in an unbounded domain, $\vec{u}$ is the disturbance in the flow velocity induced by the particle. The boundary conditions for the problem are

At the particle surface, the boundary condition reads:

$$u = U \tag{2.20a}$$

and at the far field, the boundary conditions are:

$$u \to 0 \text{ and} \tag{2.20b}$$

$$p \to p_\infty \text{ for } r \to \infty \tag{2.20c}$$

where in equation (2.20c), r is the distance from the particle and p_∞ is the free stream pressure. The expression of the drag force on a sphere was derived as [121]

$$\vec{F}_{\text{hyd}} = 6\pi\mu r\vec{U}\left(1 + \frac{3}{16}Re\right) \tag{2.21}$$

The Oseen's equations (2.19) and (2.20) are not entirely correct. Due to the linearization of the NS eqautions and the no-slip boundary condition on the surface, the inertial terms tend to zero at the particle surface. At some distances away from the particle, The inertial forces dominate and at the farfield viscous terms tend to zero, which implies that neither the Stokes equations or the Oseen equations are valid throughout the domain, this is called the Whitehead paradox. Nevertheless Oseen's linearization technique has been widely used to study problems in microhydrodynamics at finite Reynolds numbers. With the method of Matched Asymptotic Expansions (MAE), Proudman and Pearson [133] derived exact analytical expression on the drag force of a sphere with more accuracy, their expression reads as

$$\vec{F}_{\text{hyd}} = 6\pi\mu r\vec{u}\left(1 + \frac{3}{16}Re + \frac{9Re^2\ln(Re/2)}{160} + O(Re^2)\right) \tag{2.22}$$

The method of MAE has been extensively used to derive the drag force per unit length on an infinite cylinder by Proudman and Pearson [133], Kaplun and Lagerstrom [75, 74] and Skinner [153]. Hydrodynamic drag and lift forces for flow past infinite cylinders have been derived semi-empirically for higher Reynolds numbers by Taylor [163]. Taylor [163] used these results for analyzing the swimming and motion of long, axisymmetric animals [163]. Similar results for low Reynolds $Re \approx O(10^{-3})$ was derived by Tomotika *et al.* [164]. Breif details on the derivation of these solutions are presented in Chapter 4. Junk and Illner [73] re-derived Jeffery's equation based on asymptotic expansions and the solution was extended to particles of general shape and finite Reynolds numbers. Recent studies by Einarsson *et al.* [55] and Rosen [138], analyzed the motion of spheroidal and ellipsoidal particles in simple shear flows for finite shear Reynolds numbers. Their study was primarily based on perturbation and expansion methods complemented by Direct Numerical Simulation (DNS) reuslts using Lattice Boltzmann methods. In the work of Einarsson *et al.*, the orientation motion of neutrally buoyant spheroids were studied. The effect of inertia on the Jeffery orbits and the mechanics of particle rolling and tumbling were studied. In the work of Rosen *et al.* [138] the effect of inertia on the motion of triaxial ellipsoids were analyzed and studied. Several drag models for non-spherical particles in higher Reynolds number have been presented and most of these drag models are semi-empirical derived from experiments and Direct Numerical Simulations (DNS) (see section 2.3). Clift *et al.* [39] presented various drag models for non-spherical particles with short aspect ratios for various particle Reynolds numbers, these models were composed of analytical models for low Reynolds numbers and models from experimental fitted data. Holzer and Sommerfeld [67] gave the following expression for the drag coefficient for a nonspherical particle

$$C_D = \frac{8}{Re}\frac{1}{\sqrt{\phi_{\parallel}}} + \frac{16}{Re}\frac{1}{\sqrt{\phi}} + \frac{3}{\sqrt{Re}}\frac{1}{\phi^{\frac{3}{4}}} + 0.4210^{0.4(-\log\phi)^{0.2}}\frac{1}{\phi_{\perp}} \tag{2.23}$$

where in equation (2.23) C_D is the drag coefficient, defined as

$$C_D = \frac{|\vec{F}_D|}{0.5\rho|\vec{U}|^2\frac{\pi d^2}{4}} \tag{2.24}$$

The expression of the drag coefficient presented in equation (2.23) includes a term ϕ called the sphericity of the particle. Sphericity of a non-spherical particle is defined as the ratio of the surface of the volume equivalent sphere to the surface area of the non-spherical particle. The parameter $\phi_{\perp}$ is the cross-wise sphericity, defined as the ratio of the cross-sectional area of the volume equivalent sphere to the projected cross-sectional area of the non-spherical particle perpendicular to the flow direction. The parameter $\phi_{\parallel}$ is the lengthwise sphericity defined as the ratio of the cross-sectional area of the volume equivalent sphere to the cross-sectional area of the non-spherical particle projected parallel to the flow direction. This model of the drag coefficient was developed by combining the correlations obtained from the experimental studies in refs. [93, 60, 166].

Figure 2.2 shows the variation of the drag-coefficient C_D with respect to Reynolds number for various Reynolds numbers from the experimental data of [93, 60, 166]. Drag coefficients of non-spherical particles have also been obtained from DNS. Zastawny *et al.* [189] performed direct numerical simulations for ellipsoids, disc and fiber shapes. From these numerical simulations particle drag, lift and moment coefficients were derived. Holzer and Sommerfeld [68] also presented the drag and lift coefficients of nonspherical particles by DNS using the Lattice Boltzmann Method (LBM). Most of the drag models are valid for short aspect ratio particles and as the sphericity of the particle tends to lower values, i,e. as the particles approach slender shapes, these drag models do not perform well.

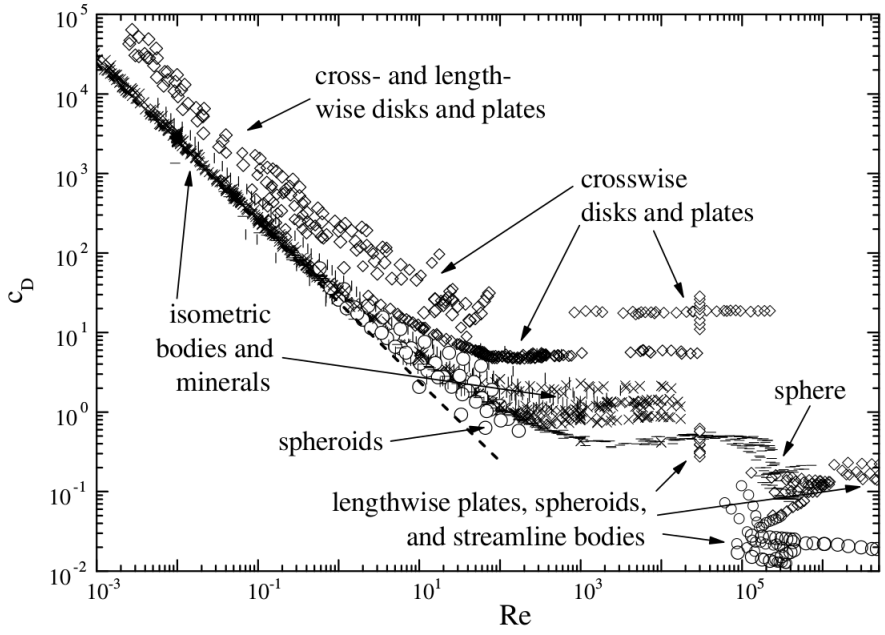

Figure 2.2: Drag coefficient vs. Reynolds numbers for various particle shapes, from [68].

2.3 Computational modelling of particulate multiphase flows

In this section some computational approaches pertaining to the numerical simulations of particulate multiphase flows are presented. The discussion is restricted to Eulerian-Lagrangian approaches or pure Lagrangian methods. The Eulerian approach for describing the dispersed phase is not considered in the present work. An overview of several methods namely Stokesian dynamics, Lagrangian point force method, Force Coupling Method (FCM) and Fully Resolved Lagrangian methods are presented.
Figure 2.3 shows a 'map' of the particle concentration with respect to the coupling approach. In the case of dilute suspensions, the fluid flow affects the particle motion and the momentum exchange from the dispersed particle phase to the fluid is not considered. The particle Reynolds numbers are usually in the creeping regime and the particles do not detach from the flow streamlines. In the two-way coupled approach, the dispersed particulate phase affects the carrier flow, however the particle concentration is so low, that the particle-particle hydrodynamic and non-hydrodynamic interactions are negligible. When the particle concentration increases, the particle-particle hydrodynamic interactions become dominant, these hydrodynamic interactions could be short range such as lubrication forces between particles or long range such as when the motion of a given particle would be affected by the wake of another particle. Understanding the particle and fluid length and time-scales are of importance when it comes to modelling of particulate flows. Based on the flow Reynolds number, the fluid would exhibit a range of length scales and time scales of motion.

2.3.1 Simulation of the fluid phase

In the case of turbulent flows, the fluid exhibits varieties of length and time scales accompanied by the transfer of energy between the scales (Figure 2.4). Full Resolution of the Navier Stokes equations [Direct Numerical Simulations (DNS)] for turbulent flows remain a challenge to this day as the number of grid points required scales to almost the cube of Reynolds number. Large Eddy Simulations (LES) resolves the larger scales of the fluid motion and the smaller scales are modelled. This is achieved based on temporal and spatial averaging by means of a 'filter' which

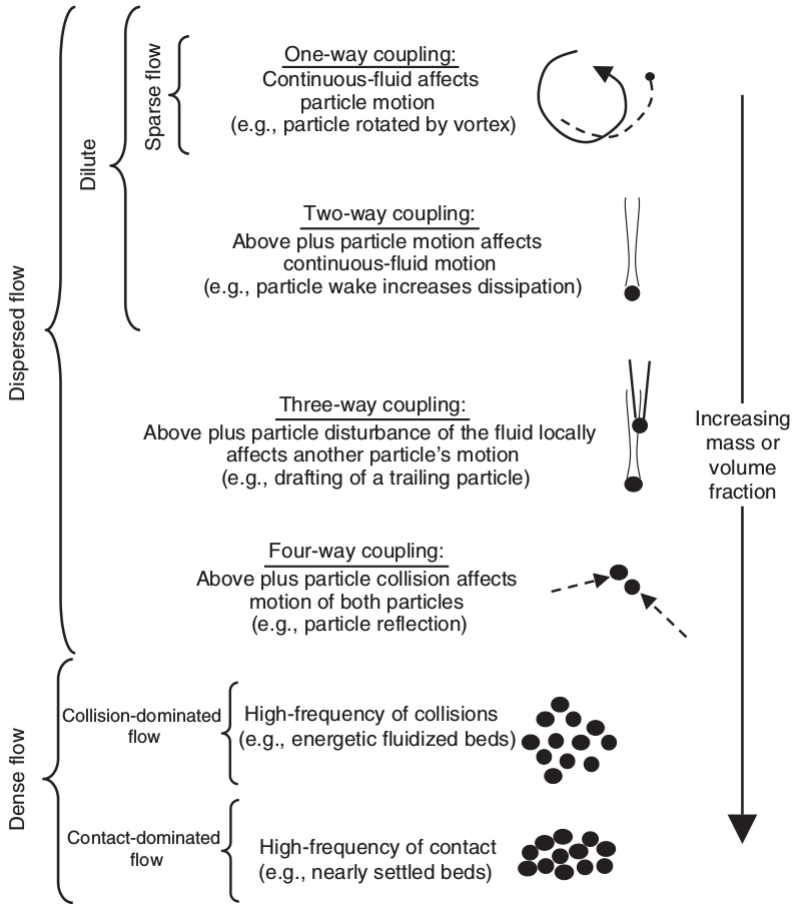

Figure 2.3: Particle concentration and fluid-particle coupling. By Loth *et al.* [104].

removes the information of the small scales. The subgrid scales and the associated turbulent stresses are then modelled using eddy viscosity models such as Smagorinsky model (constant eddy viscosity) [155] or dynamic eddy viscosity models [61].

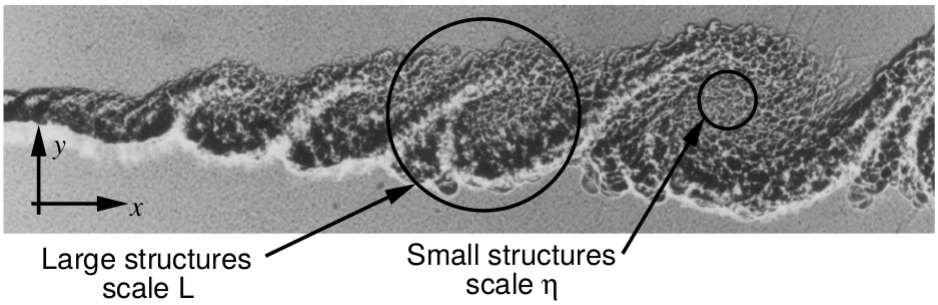

Figure 2.4: Turbulent structures in a mixing layer flow from Brown and Roshko [29]. [1]

Another approach of simulating turbulent flows is based on the Reynolds Averaged Navier Stokes equations (RANS). These equations are the time averaged Navier Stokes equations, in which the instantaneous velocity is decomposed into a mean velocity field and the fluctuating velocity

[1] Adapted from a report by U.Piomelli titled 'A primer on DNS and LES'.

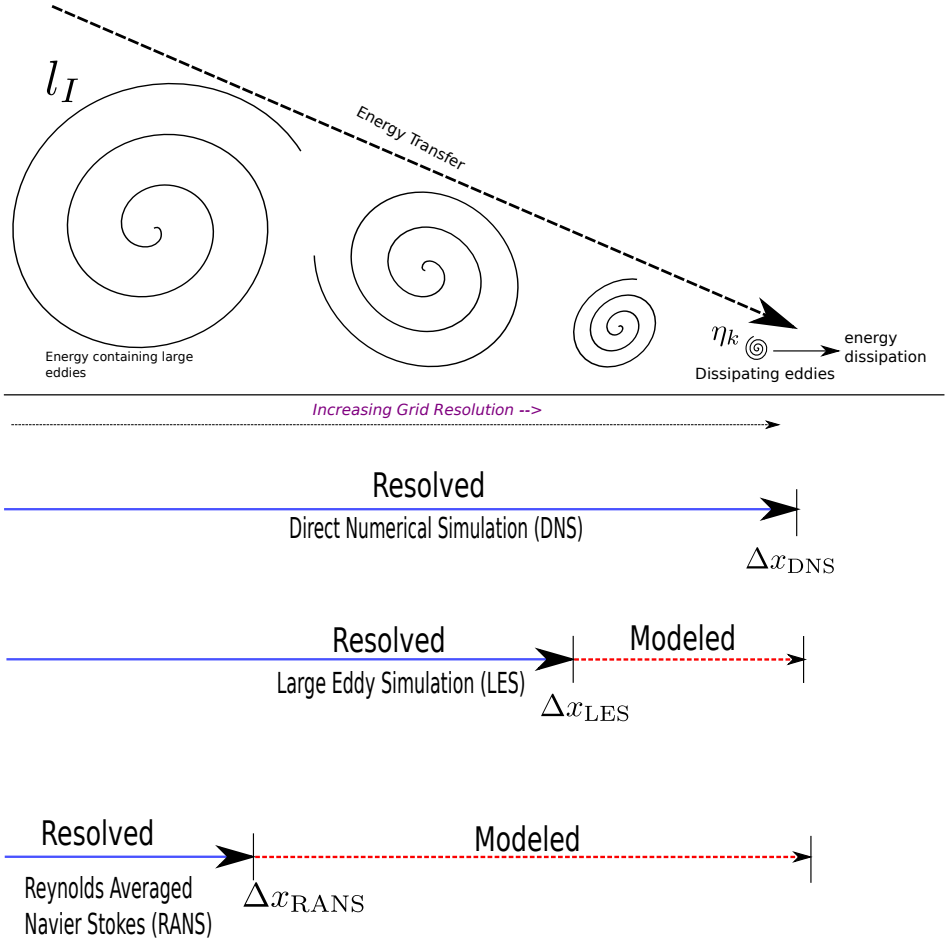

Figure 2.5: Comparison of resolution requirements in various turbulence simulation approaches. Δx refers to the grid spacing.

field. In RANS modeling, one seeks for the solution of the mean velocity field and the stresses induced by the fluctuating velocity is modeled. Several RANS models have been developed and most of these RANS models involve additional transport equations for solving the turbulent kinetic energy/turbulent viscosity or in the case of the seven equation Reynolds Stress Model (RSM) six individual components of the turbulent stresses are solved and one transport equation for the turbulent dissipation is solved. RANS models involve several semi-empirical constants derived from experimental studies and boundary layer theory [178]. Figure 2.5 shows the various turbulence modelling approaches and the associated grid requirements.

2.3.2 Simulation of particle laden flows

Stokesian Dynamics (SD) is a simulation framework initially used for rigid spherical suspensions for both dilute and dense suspensions [20] similar to Molecular Dynamics methods. The key idea in Stokesian Dynamics is to construct resistance matrices (described in section 2.2.1, equation (2.14)) for the given particle configuration in space. The method is capable of taking into account the non-hydrodynamic interparticle interactions such as Brownian forces and colloidal forces. Swan and Brady extended the method of SD to include particle wall interactions [162]. Typical SD simulations have the computational complexity of $O\left(N^3\right)$ where N is the number of spheres. Sierou and Brady [150] introduced an efficient SD method which reduces the computational complexity to $O(N\ \log N)$. Various studies on colloidal and non-colloidal suspensions based on the SD method can be found in the following refs. [84, 19, 151]

The Lagrangian point force approach is one of the most commonly used methods and has been in use since the late 80s. In this method, the motion of individual particles or cloud of particles are tracked in the simulation domain and the fluid velocities from the Eulerian grid are interpolated to the particle position. The drag force on the particle is calculated by the Stokes drag equation and the motion of the particle is calculated based on Newton's second law as

$$m\frac{d\vec{U}_p}{dt} = \vec{F}_{\mathrm{d}}. \tag{2.25}$$

Yeung and Pope [184, 185] presented a Lagrangian particle tracking algorithm for inertialess particles in isotropic turbulence with respect to spectral methods. This method was based on one-way coupling between the dispersed phase and carrier phase and it was used to study the Lagrangian statistics of velocity, acceleration and dissipation in isotropic flow fields. Eaton [52] presented a critical review on the point-particle approach within the context of particle laden flows. A detailed comparison between several experimental and numerical results were also presented. From the comparison between the numerical and experimental studies, it was shown that the Lagrangian point force method was able to reproduce the experimental results in one-way coupled simulations with good agreement. However, for two-way coupled simulations, the numerical results differed significantly from the experimental ones especially for the studies involving higher particle Reynolds numbers ($Re_p \approx 100$) and high Stokes numbers. This discrepancy was due to the fact that at higher particle Reynolds numbers, the effect of the particle unsteady wake is significant and the point force methods are not able to describe these features very well and little to no turbulence modulation was observed in the numerical studies. Balachandar and Eaton [11] presented a critical review on various approaches for modelling turbulent dispersed flows.

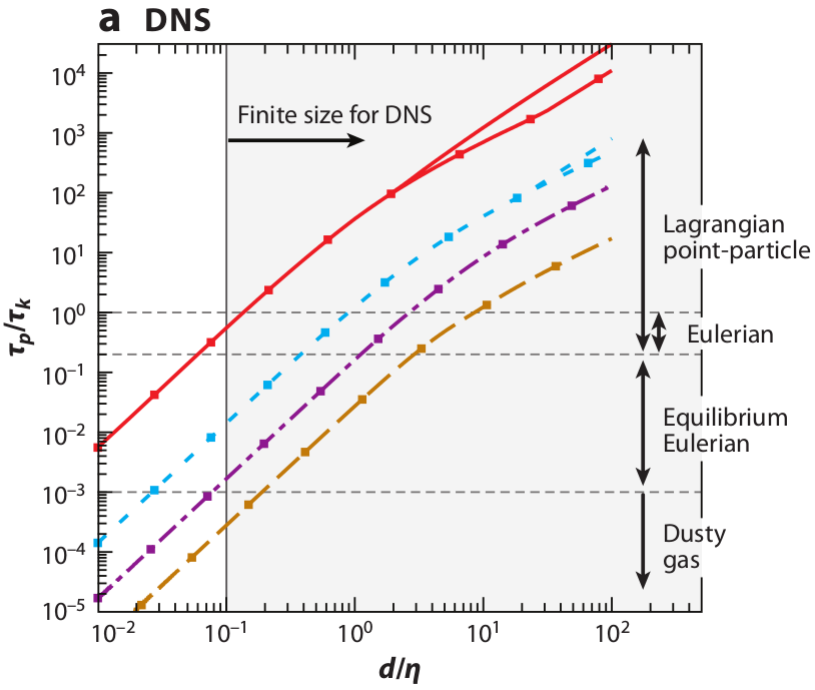

Figure 2.6: Applicability of various coupling approaches from [11]. τ_k is the Kolmogorov time scale, the time scale of the smallest eddies in the carrier flow and η is the smallest length scale (Kolmogorov length scale). d is the particle length scale

Figure 2.6 shows a plot of the time scale ratio (τ_p/τ_k) versus the particle size ratio (d/η_k) and presents the applicability of various coupling approaches. The particle relaxation time or time

scale is represented by τ_p and τ_k is the Kolmogorov time scale, i,e. the time scale of the smallest eddies. d is the particle length scale and η is the Kolmogorov length scale.
The Force Coupling Method (FCM) [40, 102] is another approach to model the coupling between the carrier phase and the dispersed phase. In this method, the presence of the particle is represented by a force distribution in the NS equations. This body force is represented as multipole expansion of the particle force [102]:

$$f_i(x,t) = \sum_{n=1}^{N_p} F_i \Delta\left(x - Y^n(t)\right) + \sum_{n=1}^{N_p} G_{ij}^n \frac{\partial}{\partial x_j} \Delta^{'}\left(x - Y^n(t)\right) \tag{2.26}$$

where in equation (2.26), the first term on the RHS F_i is the force monopole, that the particle exerts on the fluid which is comprised of the inter-particle interaction forces, particle inertia and other external forces. $Y^n(t)$ is the position of the particle at time t. The second term in the RHS G_{ij} is the force dipole related to the moment of the forces acting on the fluid, consisting of symmetric part and an anti-symmetric part. The anti-symmetric part corresponds to the hydrodynamic torque and the symmetric part corresponding to the stresslet. The information about the particle size enters equation (2.26) via the Gaussian envelopes $\Delta(x)$ for the monopole and $\Delta^{'}(x)$ for the force dipole as

$$\Delta(x) = (2\pi\sigma^2)^{-3/2} \exp\left(-\frac{|x|}{2\sigma^2}\right) \tag{2.27a}$$

and

$$\Delta^{'}(x) = (2\pi\sigma^{'2})^{-3/2} \exp\left(-\frac{|x|}{2\sigma^{'2}}\right) \tag{2.27b}$$

where $\sigma = a/\sqrt{(\pi)}$ and $\sigma' = a/(6\sqrt{\pi})^{1/3}$, a is the particle radius.
The FCM method introduces a spatially filtered velocity which leads to higher accuracy compared to conventional point force approaches especially when the turbulence in the carrier medium is resolved by Direct Numerical Simulations [11]. In fact FCM is nearly exact for low particle Reynolds numbers $\approx O(10)$ and has been extensively used to study turbulence modulation by spherical particles in channel flows [101], turbulent shear flows [175], sedimentation of spherical particles in Stokes flows [114] and micro-swimmer suspensions [45, 46].

Glowinski *et al.* [62] developed a fictitious domain method known as the Distributed Lagrangian Multiplier method (DLM/FD). The equations of fluid and particle motions are combined into a weak formulation by a 'combined velocity space' (page 766 in [62]). The fluid flow equations are enforced inside the particle constrained to a rigid body motion by means of Lagrange multipliers. The multiplier represents an additional body force per unit volume to maintain the rigid body motion in the interior of the particle. The equations are discretized based on a finite element framework. A 'fine' mesh is used to solve the fluid velocity and a coarser mesh is used for the pressure field. The particle is represented by another finite element mesh. Time advancement of the combined system is performed based on operator splitting techniques (Marchuk-Yamenko) similar to the method of Chorin [35]. The Lagrange multipliers are used as force densities in the last step of the fractional step of the time advancement. Singh *et al.* [152] and Patankar *et al.* [124] presented a modified version of the DLM method, with improved collision physics between the particles similar to a soft sphere approach, where the particles can overlap each other. Within the context of spectral finite element methods, Dong *et al.* [48] presented a DLM method. Studies on settling of spheres under gravity in a fluid column has been published using this method [152, 62, 187].

Immersed Boundary methods (IBM) and its variants have been popular in simulating particulate multiphase flows. Peskin [126, 128, 127] presented one of the first IBM approaches for studying the fluid dynamics of heart valves. In this method, the NS equations are solved on a fixed cartesian grid and the discretization of the NS equations can be based on finite difference

methods/volumes or elements and the solid object is represented by discrete Lagrangian marker 'fibers'. The relative displacement of these lagrangian markers by the fluid velocity is used to calculate the elastic response of the fibers. The no slip boundary condition on these marker points is enforced by setting the velocity of the marker points to the velocity of the fluid in the grid points in the vicinity of the marker. Based on Peskin's IB method, Uhlmann [169] developed a direct forcing IB formulation. This formulation utilizes the regularized delta functions of Peskin [127] to interpolate the fluid velocity to the Lagrangian marker points and in 'spreading' the feed back force from the particle to the fluid grid. The key idea in Uhlmann's method [169] is to evaluate a body force term in the Lagrangian marker points at an intermediate time level between t^n and t^{n+1} :

$$\vec{F}^{n+1/2} = \frac{\vec{U}^d - \vec{U}^n}{\Delta t} - \mathrm{RHS}^{n+1/2} \tag{2.28a}$$

where in equation (2.28a), $\vec{U}^d$ is the velocity at the Lagrangian marker, RHS is the right hand side of the NS equations including the viscous terms and the pressure gradient term. The expression for $\vec{U}^d$ reads:

$$\vec{U}^d(X_l^i) = \vec{u}_c^i + \vec{\omega}_c^i \times \left(X_l^i - x_c^i\right) \tag{2.28b}$$

where x_c is the geometric center of the particle, $\vec{u}_c^i$ the velocity at the center of the particle and $\vec{\omega}_c^i$ the rotational velocity of the particle center. The velocity $\vec{U}^n$ is interpolated from the fluid grid using the following expression:

$$\vec{U}_n = \sum \vec{u}_f \delta_h \left(x_\mathrm{f} - X_l\right) h^3 \tag{2.28c}$$

in equation δ_h is a discrete dirac-delta function and h is the grid spacing. Details of this function can be found in the work of Roma *et al.* [136]. The feed back force is then interpolated back to the fluid grid using an expression similar to (2.28c). Breugem [25] improved the IB framework of Uhlmann [169] by including a multidirect forcing scheme for better approximation of the no-slip boundary condition on the particle interface. Additional improvements were made in reducing the grid dependency on the IB scheme ('estimation of the effective particle diameter') and the overall numerical stability of the IB scheme was improved. The aforementioned IB scheme was modified by Ardekani *et al.* [8, 9] by including particle-particle interactions for various particle shapes (ellipsoids, spheroids). The method was used to study the influence of particle concentration and shape in drag reducing turbulent flows.

Within context of Lattice Boltzmann Methods (LBM), the 'standard bounce back' model and the 'external boundary forcing methods' were applied to study particle laden flows. A detailed review has been presented by Aidun and Clausen [2] and a detailed method for the simulation of suspensions using the LB framework has been derived by Ladd [85, 86]. A recent review on numerical methods for the simulation for particle laden multiphase methods has been presented by Maxey [113]. The review covers several other methods such as the Arbitrary Lagrangian Eulerian (ALE) approach and the PHYSALIS methods [190, 149] for the simulation of multiphase flows.

2.4 Numerical modeling of rigid and flexible fibers

Rigid fibers Based on the point force coupling approach, several studies on the orientation behavior and preferential concentration in turbulent channel flows for various Stokes numbers and fiber aspect ratios have been presented in refs [33, 108, 192, 191, 119]. In these studies, the fibers were modeled as Lagrangian points, utilizing the hydrodynamic force and torque models

based on Jeffery's theory [70]. The relaxation time of the fiber was calculated using the expression derived from the experimental studies of Shapiro and Goldenberg [145],

$$\tau_p = \frac{2Da^2 \ln\left(r_p + \sqrt{r_p^2 - 1}\right)}{9\nu\sqrt{r_p^2 - 1}} \tag{2.29a}$$

In equation (2.29a) D is the ratio of particle density to fluid density, r_p the aspect ratio. The associated Stokes number is

$$St = \frac{\tau_p u_\tau^2}{\nu} \tag{2.29b}$$

where u_τ is the turbulent friction velocity. Shin and Koch [147] used the slender body theory of Khayat and Cox [79] valid at finite Reynolds numbers (Reynolds based on the fiber length) for studying the rotational diffusion of long rigid fibers in isotropic turbulence. The integral equations were solved using a pseudo-spectral method [148]. A similar method was used by Lopez and Guazzelli [103] for studying the settling of fibers under a vortical flow. Saintillan *et al.* [140] used particle mesh Ewald summation algorithm to simulate settling of fiber suspensions.
Flexible fibers: In the framework of simulating flexible fibers, Tornberg and Shelley [165] derived a non-local SBT (slender body theory) formulation [77, 71] coupled with the Euler-Bernoulli beam theory to yield integral expressions for the center-line velocity of high aspect ratio filaments. Their numerical model included the hydrodynamic interactions between multiple fibers and the effect of fibers on the background fluid. Li et al [94] used a variation of the numerical method proposed by Tornberg and Shelley [165] to study the sedimentation of flexible filaments. A detailed review of SBT concerning modeling fibers has been presented by Lindner and Shelley [96]. Stockie and Green [158] used Peksin's method to simulate the dynamics of a single flexible fiber and they were able to reproduce the deformed fiber shapes observed experimentally by Forgac & Mason [58]. Wiens and Stockie [177] developed a parallel scalable IBM based on a Kirchoff's rod model proposed by Lim et *et al.* [95]. Aidun [180, 181, 141] and coworkers used an IBM within the LBM framework known as 'external boundary forcing' method to study the effect of fiber stiffness and rotational diffusion of semi-dilute sheared fiber suspensions. Immersed Boundary Methods/Fictitious Domain Methods, aim to fully resolve the flow-field around a fiber and are therefore computationally expensive.
In bead/rod models, a fiber is represented by an array of spheres or prolate spheroids. Yamamoto & Matsuoka [183] developed a flexible fiber mechanical model where a fiber consisted of spheres that are bonded to each other. The mechanical properties of the fiber were determined based on the bending, twisting and stretching constants. Their model was validated against low Reynolds number flows such as the motion of a single fiber in shear flow with respect to Jeffery's predictions [70] and to the deformation of fibers observed experimentally by Forgacs & Mason [58]. Their study only considered one way coupling, ignoring the action of fibers on the fluid. Joung *et al.* [72] developed a similar model where a fiber was represented by a chain of spheres with inextensible connectors thereby allowing the bending and twisting dynamics of the fibers and the model was used to study the behavior of Newtonian suspensions and predict the viscosity of a flexible fiber suspension. Delmotte *et al.* [44] improved the model of Yamamoto and Matsuoka [183] by implementing Lagrange multipliers and a new contact model between the spheres known as the Gears model to define the twisting and bending behavior. The model was validated with Jeffery's predictions, [70] sedimentation of a flexible fiber, dynamics of an actuated filament and swimming of microorganisms.
Schmid *et al.* [144] developed a model for flexible fibers in which the hydrodynamic force of the fiber was represented as a chain of prolate spheroids (hereby referred to as PS model) and included the contact forces between the fibers. Their model was used to study the formation of flocs in fiber suspensions, effect of fiber equilibrium shapes on the viscosity of fiber suspensions, however their simulations were still based on one-way coupling. Lindström and Uesaka [97] improved

the numerical stability of the model proposed by Schmid *et al.* [144] and also implemented a two-way coupling scheme. Moreover a hydrodynamic force model for the inertial regime was proposed. The model was used for the study of semi-dilute non-brownian fiber suspensions [98]. The same model of Lindström & Uesaka [97] was used by Andrić *et al.* [6, 5, 7] for studying the behavior of dilute suspensions and motion of fibers in inertial flows. However the hydrodynamic force presented by Lindström & Uesaka [97] are not accurate for intermediate inertial Reynolds numbers and for low angles of attack past the fiber, the component of force parallel to the fiber symmetric axis was neglected. A detailed review of such models have been presented by Lindner and Shelley [96] and Hämäläinen *et al.* [65].

2.5 Objectives of the present work

In this Chapter, an introduction to particulate multiphase flows have been presented. The formulation of hydrodynamic forces and torques on non spherical particles from the creeping regime to inertial regimes have been explained, followed by short descriptions on computational methods to simulate particulate flows have been presented. From the discussions presented in this Chapter, it is evident that the behavior of dilute and semi-dilute suspensions in inertial flows are not fully understood. This thesis aims at developing a Eulerian Lagrangian method to numerically simulate the collective behavior of several thousands of fibers in creeping and inertial flows. The fluid phase is solved by Finite Volume Method (FVM) and the motion of the fibers are solved based on the Discrete Element Method (DEM). The coupling between the phases is based on a 'pseudo' immersed boundary method, as the fibers are discretized into several segments and the length of each segment is comparable to the cell edge length of the fluid domain. The drag force on the fiber segments are obtained via analytical expressions and drag correlation formulae. In Chapter 3, the governing equations of motion and the numerical methods for the fluid and fiber are discussed. Chapter 4 presents an analysis on the use of hydrodynamic force and torque models relevant to long fibers (fibers with aspect ratio $r_p > 10$). In Chapter 5 the developed numerical framework is tested for fibers in inertial flows. Chapter 6 deals with fibers in the Stokes regime, i.e. a numerical study on semi dilute rigid fiber suspensions in shear is presented. This study highlights the ability of the developed numerical model to reasonably capture and describe the many body hydrodynamic interactions between the fibers. In Chapter 7, preliminary results of the drag reducing effects in semi-dilute fiber suspensions in turbulent pipe flows are presented.

CHAPTER 3

NUMERICS AND COUPLING METHODOLOGY

Contents

3.1 Introduction

This chapter describes the governing equations for the fiber and fluid motions, and the momentum exchange between the two phases. Two separate solvers are used to solve the equations of motion of the fibers and the fluid. The equations of motion of the fibers are solved using the open source Discrete Element Method (DEM) code YADE. The fibers are discretized into several beam segments, with each segment being composed of a pair of nodes (fig. 8.2). The equations of motion for the nodes are solved by a 2^{nd} order explicit accurate scheme (time and space). The high-fidelity finite volume code YALES2 is used to solve three dimensional incompressible Navier-Stokes equations. The fluid domain is discretized using a 4^{th} order accurate (space and time) explicit finite volume scheme. Momentum exchange between the phases is included via the source term in the Navier-Stokes equations.

This chapter begins with a brief outline of the discrete element method and the solver. It is followed by a description of the mechanical model of the fiber and its discretization. An outline

of the fluid solver YALES2 and the finite volume discretization is presented. The chapter closes with coupling methods used to exchange data between the solvers.

3.2 Discrete element solver

YADE (Yet Another Dynamic Engine) is an open-source DEM solver primarily intended to solve problems arising in granular materials. This code includes a variety of contact laws to describe the interaction physics between particles (spherical, non-spherical and polyhedral shapes). Written primarily in C++, YADE includes Python wrappers for the C++ classes and the user defines a simulation case in a Python script, calling the required 'engines'. Within the context of this thesis, the contact laws between fiber segments have been modified to include the lubrication terms. Furthermore several C++ and Python functions were written in order to facilitate coupling and data exchange with YALES2.
Figure 3.1 shows a typical simulation work flow in the DEM solver YADE. Initially the particles with their associated shape, material, translational and rotational velocities and their axis-aligned bounding boxes are initialized. A collision detection algorithm checks for potential contacts via a sweep and prune and insertion sort algorithms [174]. Once a potential contact between a particle pair is identified, geometric parameters that define the 'indentation depth' or deformation are calculated. Forces and torques based on the specified contact laws are calculated for each contact pair and stored for the current timestep.

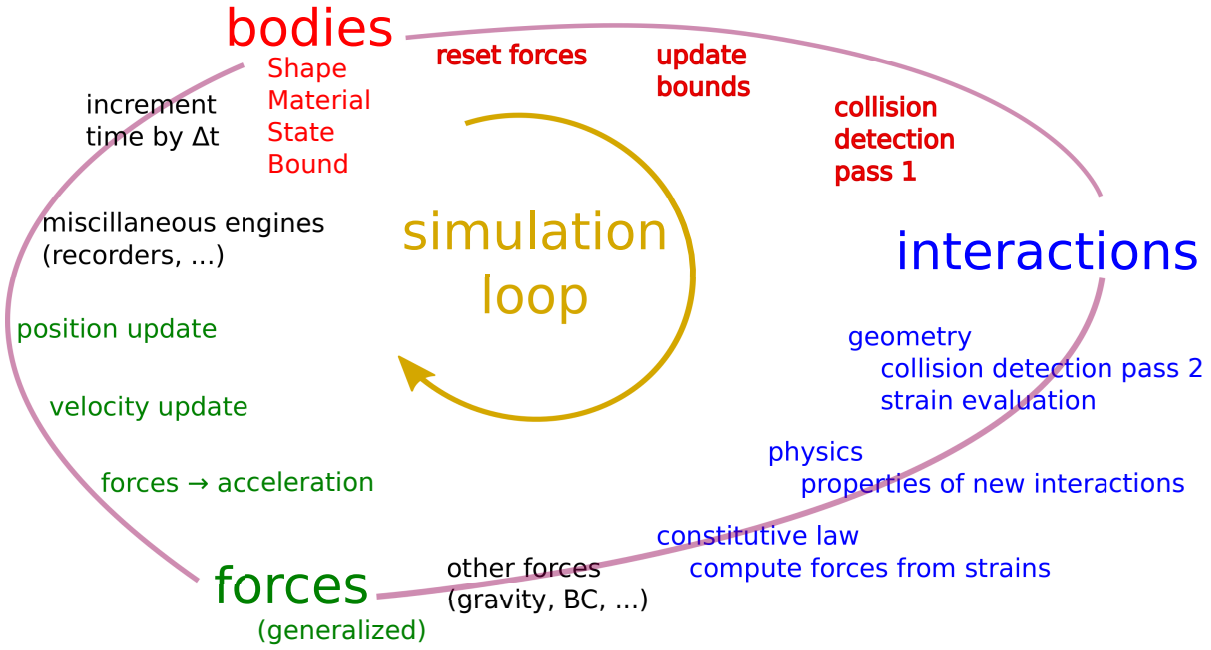

Figure 3.1: Simulation loop from YADE documentation [174].

For the sake of simplicity, the particles considered in this section are spherical. Acceleration (translational and rotational) of the spheres are calculated from the respective forces and torques. Using a 2nd order accurate explicit verlet-velocity integration like scheme, new particle velocities and positions are calculated. The following set of equations can be written for a sphere. Representing the position of the center of mass of a sphere n as $\vec{O}_n$, the translational acceleration at time t can be written as

$$\ddot{\vec{O}}_n(t) = \vec{F}(t)/m_n \tag{3.1}$$

where in equation (3.1), $\vec{F}(t)$ is the sum of all interaction forces on the sphere n. Similar to

equation (3.1), the rotational acceleration $\vec{\dot{\omega}}_n$ for sphere n with moment of inertia J_n is written as

$$\vec{\dot{\omega}}_n(t) = \vec{T}(t)/J_n \tag{3.2}$$

where in equation (3.2), $J_n = 2/5 m_n r_n^2$. In these equations, m_n is the mass of the sphere and r_n the radius.
For a nonspherical particle, the torque equation (3.2) reads:

$$\frac{d}{dt}(\mathbf{J}\vec{\omega}_n(t)) = \vec{T}(t) \tag{3.3}$$

In equation (3.3), $\mathbf{J}$ is the moment of inertia tensor.
From equations (3.1), an expression for the position of the particle at $t + \Delta t$ can be obtained by Taylor expansion along the particle coordinate $\vec{O}_n(t)$ as follows:

$$\vec{O}_n(t + \Delta t) = \vec{O}_n(t) + \Delta t \underbrace{\left[\vec{\dot{O}}_n(t) + (\Delta t/2)\vec{\ddot{O}}_n(t)\right]}_{\text{T1}} \tag{3.4}$$

where in equation (3.4), the term T1 is the the Taylor expansion of the velocity $\vec{\dot{O}}_n(t)$ about $\Delta t/2$, i.e $\vec{\dot{O}}_n(t + \Delta t/2)$. Hence the leapfrog integration equations are

$$\vec{\dot{O}}_n(t + \Delta t/2) = \vec{\dot{O}}_n(t - \Delta t/2) + \Delta t\, \vec{\ddot{O}}_n(t) \tag{3.5}$$

$$\vec{O}_n(t + \Delta t) = \vec{O}(t) + \Delta t\, \vec{\dot{O}}_n(t + \Delta t/2) \tag{3.6}$$

The leapfrog equations for updating the particle orientation is analogous to equations (3.5) and (3.6) for spherical particles. However for non-spherical particles, the numerical integration is quite involved as its local reference frame is not inertial [174]. Details of the rotation integration can be found in ref [174].

3.2.1 Fiber mechanical model

The mechanical model of the fiber in the present work has been previously used to study various problems in geomechanics/geotextiles [34, 18, 53]. Geometrically, a single fiber segment is represented by a sphero-cylinder, obtained by the Minkowski sum of a sphere and line. Consider a fiber $\mathcal{F}$, as shown in figure 8.2, composed of $\{b_1, b_2, b_3, ..., b_n\}$ fiber segments,$\{c_1, c_2, c_3, ..., c_{n+1}\}$ are the nodes on the fiber segments. $\{\vec{O}_1, \vec{O}_2, \vec{O}_3, ..., \vec{O}_{n+1}\}$ are the position vectors of these nodes and $\vec{Ze}$ is the end to end vector of the fiber . (e_x, e_y, e_z) forms an orthonormal basis that is fixed on the fiber segment and $\vec{p}$ is the orientation vector of a given fiber segment. The length of a fiber segment is defined as $l = ||\vec{O}_n - \vec{O}_{n-1}||$
The fiber segments are massless and the masses are concentrated on the nodes. The equations of motion for a fiber node c_n, while neglecting the gravity effects, read as

$$\vec{F}_{\text{HYD}_{c_n}} + \vec{F}_{\text{int}} + \sum_{i=1}^{m} \vec{F}_{\text{con}_{c_n,c_i}} + \sum_{i=1}^{m} \vec{F}_{\text{lub}_{c_n,c_i}} = m_{c_n} \vec{\ddot{O}}_{c_n} \tag{3.7}$$

$$\vec{T}_{\text{HYD}_{c_n}} + \vec{M}_{\text{int}} + \sum_{i=1}^{m} \vec{M}_{\text{con}_{c_n,c_i}} = \mathbf{J}_{b_n} \vec{\dot{\omega}}_{c_n} \tag{3.8}$$

where in equation (3.7), $\vec{F}_{\text{HYD}_{c_n}}$ is the hydrodynamic force, $\vec{F}_{\text{int}}$ is the internal force of the fiber segment which consists of a normal force component $\vec{F}_{N_{c_n}}$ and shear force component $\vec{F}_{S_{c_n}}$. $\vec{F}_{\text{con}_{c_n,c_i}}$ the contact force applied by contacting fiber segments and $\vec{F}_{\text{lub}_{c_n,c_i}}$ is the lubrication

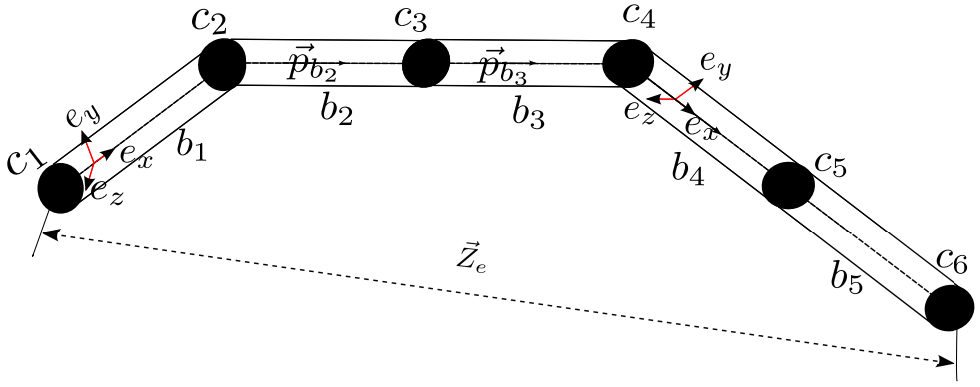

Figure 3.2: Fiber geometry.

force between the fiber segments. The position vector $\vec{O}$ refers to the center of mass of the fiber nodes.
In equation (3.8), $\vec{T}_{\mathrm{HYD}_{c_n}}$ is the hydrodynamic torque, $\vec{M}_{\mathrm{int}}$ is the internal moment consisting of a bending moment $\vec{M}_{B_{c_n}}$ and a twisting moment $\vec{M}_{T_{c_n}}$. $\mathbf{J}_{b_n}$ is the inertia tensor, and $\vec{\omega}_{c_n}$ the angular acceleration. $\vec{M}_{\mathrm{con}_{c_n,c_i}}$ is the moment at the nodes due to the contact forces. The moments are calculated at the point O_n.
From equations (3.7) and (3.8), the equation of forces and moments on a fiber segment b_i having the nodes c_n and c_{n-1} are as follows :

1. The normal force $\vec{F}_N$

$$\vec{F}_{N_{c_n}} = k_n(l - l_o)\vec{p}_{b_i}, \tag{3.9}$$

where l_o refers to the length of the fiber segment at the stress free configuration, l the length in the actual configuration and k_n is the elastic stiffness associated to the normal force defined as

$$k_n = \frac{\pi E r_f^2}{l}, \tag{3.10}$$

where in expression (3.10), E is the tensile modulus of the beam material and r_f the radius of the fiber segment.

2. The twisting moment $\vec{M}_T$ between the nodes

The relative rotation between the nodes is used to define the bending and twisting components. Using a rotational vector representation, the relative rotation $\vec{\Omega}_{n-1,n}$ between the nodes c_{n-1} and c_n is defined as

$$\vec{\Omega}_{c_{n-1},c_n} = \vec{\Omega}_{c_n} - \vec{\Omega}_{c_n-1} \tag{3.11}$$

The component of twist between the nodes is

$$\vec{\Omega}^T_{c_{n-1},c_n} = (\vec{\Omega}_{c_{n-1},c_n}.\vec{p_{b_i}}).\vec{p_{b_i}} \tag{3.12}$$

and the equation for twisting moment is

$$\vec{M}_T = k_t\vec{\Omega}^T_{c_{n-1},c_n}. \tag{3.13}$$

where k_t is the stiffness associated to the twisting moment defined as

$$k_t = \frac{\pi G r_f^4}{2l}, \tag{3.14}$$

where G is the shear modulus of the beam material.

3. The shear force $\vec{F}_S$ and bending moment $\vec{M}_B$

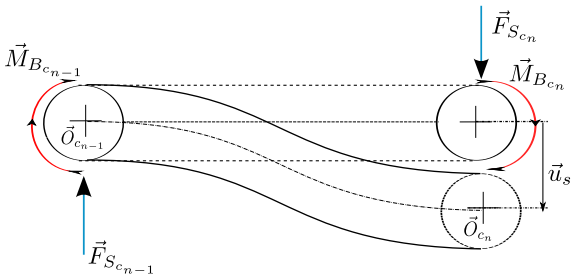

Figure 3.3: Definition of the shear displacement $\vec{u}_s$ in a fiber segment subjected to pure shear.

The bending moment and shear force (figure 3.3) are mechanically coupled. Their rates of change are linearly dependent on the rotational and translational velocities of the nodes and can be expressed by introducing a matrix similar to the stiffness matrix of a beam element [193] in structural mechanics [18]

$$\begin{pmatrix} \dot{\vec{F}}_{S_{c_n}} \\ \dot{\vec{M}}_{B_{c_n}} \\ \dot{\vec{F}}_{S_{c_{n-1}}} \\ \dot{\vec{M}}_{B_{c_{n-1}}} \end{pmatrix} = -\frac{\pi E r_f^4}{4l^3} \begin{pmatrix} 12 & 6l & -12 & 6l \\ 6l & 4l^2 & -6l & 2l^2 \\ -12 & -6l & 12 & -6l \\ 6l & 2l^2 & -6l & 4l^2 \end{pmatrix} \begin{pmatrix} \vec{u}_{s_{c_n}} \\ \vec{\omega}_{B_{c_n}} \\ \vec{u}_{s_{c_{n-1}}} \\ \vec{\omega}_{B_{c_{n-1}}} \end{pmatrix} \tag{3.15}$$

where in equation (3.15), $\vec{u}_{s_{c_n}}$ is the shear velocity (orthonormal component of the velocity) of the node defined as

$$\vec{u}_{s_{c_n}} = (\mathbf{I} - \vec{p}_{b_i} \otimes \vec{p}_{b_i}) \cdot \dot{\vec{O}}_{c_n} \tag{3.16}$$

and $\vec{\omega}_{B_{c_n}}$ is the rotational velocity associated to the bending, defined as

$$\vec{\omega}_{B_{c_n}} = \vec{\omega}_{c_n} - (\vec{\omega}_{c_n} \cdot \vec{p}_{b_i}) \cdot \vec{p}_{b_i} \tag{3.17}$$

4. Contact detection between the fiber segments

Consider two non-adjacent (non-parallel, non-intersecting) fiber segments b_i and b_j with the nodes b_ic_{n-1}, b_ic_n on b_i and b_jc_{n-1},b_jc_n on b_j as shown in figure 3.4.

The contact forces between the fiber segments are calculated based on the distance between the segments b_i and b_j. The direction vector of the segment b_i is $\vec{p}_{b_i}$ and that of b_j is $\vec{p}_{b_j}$. The position vector of the node b_ic_n is denoted by $\vec{O}_{b_ic_n}$ and the position vector of node b_jc_n is denoted by $\vec{O}_{b_jc_n}$ and based on these position vectors the equation of a parametric line can be written as

$$\vec{\boldsymbol{A}}(\boldsymbol{s}) = \vec{O}_{b_ic_n} + s\vec{p}_{b_i} \tag{3.18}$$

$$\vec{\boldsymbol{B}}(\boldsymbol{t}) = \vec{O}_{b_jc_n} + t\vec{p}_{b_j} \tag{3.19}$$

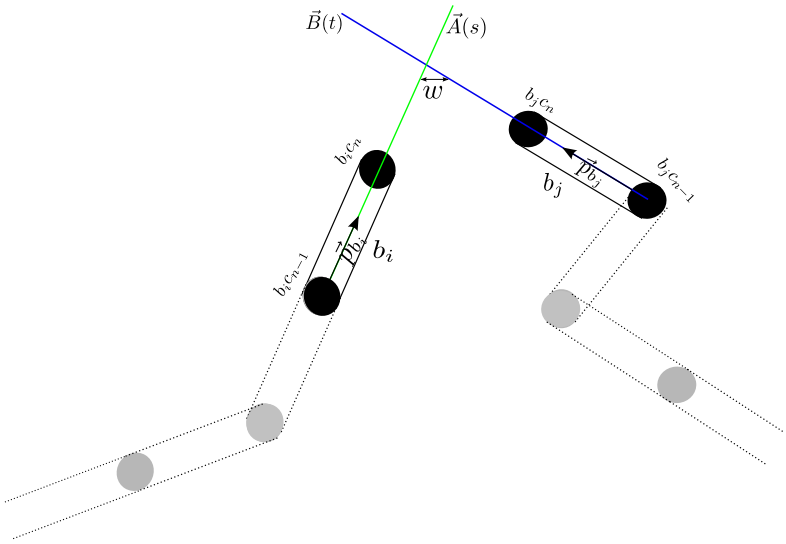

Figure 3.4: Interaction between non-parallel and non intersecting segments, adapted from [53]

where, $(s,t) \in [0,1] \times [0,1]$. The vector $\vec{w}$ is defined as

$$\vec{w}(s,t) = \boldsymbol{\vec{A}(s) - \vec{B}(t)} \tag{3.20}$$

The aim is to find $(s_c, t_c) \in [0,1] \times [0,1]$, such that

$$\boldsymbol{\vec{w}_c} = \vec{w}(s_c,t_c) = \vec{A}(s_c) - \vec{B}(t_c) = \min_{(s,t)\in[0,1]\times[0,1]} \vec{w}(s,t) \tag{3.21}$$

The vector $\boldsymbol{\vec{w}_c} = \vec{w}(s_c,t_c)$ is uniquely perpendicular to the segment direction vectors $\vec{p}_{b_i}$ and $\vec{p}_{b_j}$. Hence it satisfies : $\vec{p}_{b_i}.\boldsymbol{\vec{w}_c} = 0$ and $\vec{p}_{b_j}.\boldsymbol{\vec{w}_c} = 0$ and the following system of equations can be written :

$$\begin{cases} \boldsymbol{\vec{w}_c} = \vec{A}(s_c) - \vec{B}(t_c) \\ \vec{p}_{b_i} \cdot \boldsymbol{\vec{w}_c} = 0 \\ \vec{p}_{b_j} \cdot \boldsymbol{\vec{w}_c} = 0 \end{cases} \tag{3.22}$$

The solution of equation (3.22) is given by

$$\begin{cases} s_c &= \frac{(\vec{p}_{b_i}\cdot\vec{p}_{b_j})(\vec{p}_{b_j}\cdot\vec{w_0}) - ||\vec{p}_{b_j}||(\vec{p}_{b_i}\cdot\vec{w_0})}{||\vec{p}_{b_i}||||\vec{p}_{b_j}|| - (\vec{p}_{b_i}\cdot\vec{p}_{b_j})^2} \\ t_c &= \frac{||\vec{p}_{b_i}||(\vec{p}_{b_j}\cdot\vec{w_0}) - (\vec{p}_{b_i}\cdot\vec{p}_{b_j})(\vec{p}_{b_i}\cdot\vec{w_0})}{||\vec{p}_{b_i}||||\vec{p}_{b_j}|| - (\vec{p}_{b_i}\cdot\vec{p}_{b_j})^2} \end{cases} \tag{3.23}$$

where in equation (3.23), $\vec{w}_o = \vec{O}_{b_i c_{n-1}} - \vec{O}_{b_j c_{n-1}}$.

Once the values of s_c and t_c are obtained, the criterion for the contact is defined as:

$$||\vec{w}_c(s_c,t_c)|| \leq ||s_c - t_c|| \tag{3.24}$$

5. Contact force between two fiber segments

   The contact between two fiber segments b_i, b_j having radii r_{b_i}, r_{b_j} is shown in figure 3.5. Once a potential contact is found based on the criteria in equation (3.24), each segment in

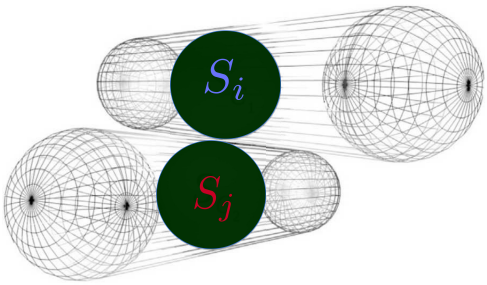

Figure 3.5: Interaction between two fiber-segments

the contact is associated with one virtual node at the contact points s_c and t_c. The virtual nodes S_i and S_j are positioned along the vectors connecting the nodes of beam segments b_i, b_j in contact as shown in figure 3.5. $||\vec{w}_c(s_c, t_c)|| = ||\vec{S}_i - \vec{S}_j||$ defines the shortest distance between the respective axes of the segments in contact. The translational $\dot{\vec{S}}_i$ and rotational velocities $\vec{S}_{\omega_i}$ of a virtual node S_i are calculated from its associated segment in the following way[53, 18]:

$$\dot{\vec{S}}_i = \lambda \dot{\vec{O}}_{c_{n-1}} + (1-\lambda)\dot{\vec{O}}_{c_n}. \tag{3.25}$$

$$\vec{S}_{\omega_i} = \lambda \vec{\omega}_{c_{n-1}} + (1-\lambda)\vec{\omega}_{c_n}. \tag{3.26}$$

$$\lambda = \frac{||\vec{O}_{c_{n-1}} - \vec{S}_i||}{||\vec{O}_{c_{n-1}} - \vec{O}_{c_n}||}. \tag{3.27}$$

The contact force $\vec{F}_{\text{con}}$ consists of a normal $\vec{F}_{\text{con},N}$ and shear component $\vec{F}_{\text{con},S}$, the expression for the normal force reads as

$$\vec{F}_{\text{con},N} = k_{n_{\text{con}}} u_{n,\text{con}} \cdot \vec{n}_{\text{con}} \tag{3.28}$$

where $u_{n,\text{con}}$ is the normal displacement (indentation depth) and $\vec{n}_{\text{con}}$ the contact normal between the virtual nodes, which are defined as

$$u_{n,\text{con}} = ||\vec{S}_i - \vec{S}_j|| - r_{S_i} - r_{S_j} \tag{3.29a}$$

$$\vec{n}_{\text{con}} = \frac{\vec{S}_i - \vec{S}_j}{||\vec{S}_i - \vec{S}_j||} \tag{3.29b}$$

where in equation (3.29a) r_{S_i} and r_{S_j} are the radii of the virtual nodes and $r_{S_i} = r_{b_i}$, $r_{S_j} = r_{b_j}$.

$k_{n_{\text{con}}}$ is the normal stiffness between the contact nodes

$$k_{n_{\text{con}}} = 2\hat{k}\frac{r_{S_i} r_{S_j}}{r_{S_i} + r_{S_j}} \tag{3.30a}$$

where in equation (3.30a), $\hat{k}$ is the normalized stiffness and $\hat{k}$ is assigned the value of E.

The shear stiffness $k_{s_{\text{con}}}$ is defined as

$$k_{s_{\text{con}}} = \alpha k_{n_{\text{con}}} \tag{3.30b}$$

where in equation (3.30b), α is a non dimensional parameter.

The contact shear force $\vec{F}_{\text{con},S}$ is as follows:

$$\vec{F}^{t+dt}_{\text{con},S} = \vec{F}^{t}_{\text{con},S} + k_{s_{\text{con}}} \vec{\dot{u}}_{s_{\text{con}}} dt \tag{3.31a}$$

$$||\vec{F}_{\text{con},S}|| \leq \mu_f ||\vec{F}_{\text{con},N}|| \tag{3.31b}$$

where in equation (3.31a), $\vec{\dot{u}}_{s_{con}}$ is the relative shear velocity defined as

$$\vec{\dot{u}}_{s_{con}} = (\mathbf{I} - \vec{n}_{\text{ncon}} \otimes \vec{n}_{\text{ncon}}) \cdot \left(\vec{\dot{S}}_i - \vec{\dot{S}}_j\right) + \left(\left(\vec{S}_{\omega_i} - \vec{S}_{\omega_j}\right) \times \frac{\vec{S}_i - \vec{S}_j}{2}\right) \tag{3.32}$$

and μ_f is the coefficient of friction. Equation (3.31) leads to an elastic-frictional condition between the fiber segments in contact.

Hence the expression for the contact force reads as

$$\vec{F}_{\text{con}} = \vec{F}_{\text{con},N} + \vec{F}_{\text{con},S} \tag{3.33}$$

The moment of this force about S_i is:

$$\vec{M}_{\text{con}} = \left(\vec{C} - \vec{S}_i\right) \times \vec{F}_{\text{con}} \tag{3.34}$$

considering the contact point located at $\vec{C} = (\vec{S}_i + \vec{S}_j)/2$

The contact force $\vec{F}_{\text{con}}$ and the corresponding moment $\vec{M}_{\text{con}}$ are then distributed to the nodes of the segment using λ as the interpolation weight. Further details are reported in the works of Bourrier *et al.* [18] and Effeindzourou *et al.* [53, 174]

6. Lubrication forces

The lubrication force between the fiber segments is based on the formulation of Frenkel and Acrivos [59], and it is composed of a normal component and a shear component.The normal component of the lubrication force is written as

$$\vec{F}^{L}_{n} = \frac{3}{2}\pi\mu\frac{r_f^2}{h}\vec{\dot{u}}_n. \tag{3.35}$$

The equation for the shear component is

$$\vec{F}^{L}_{s} = \frac{\pi\mu}{2}\Big[-2r_f + (2r_f + h) + \ln\frac{(2r_f + h)}{h}\Big]\vec{\dot{u}}_s, \tag{3.36}$$

where in equations (3.35) and (3.36), μ is the fluid viscosity, r_f is the radius of the fiber segment, h is the distance between 2 adjacent fibers (calculated based on equation (3.22)), $\vec{\dot{u}}_n$ and $\vec{\dot{u}}_s$ are the normal and shear velocity components of the fiber segment.

3.2.2 Numerical stability

The stability based on the stiffness of the fiber segments is derived as follows [69]. For a given node c_n that participates in N_i interactions, an equivalent translational stiffness $\mathbf{K}_{\text{tran}}$ and rotational stiffness $\mathbf{K}_{\text{rot}}$ matrices are written. This is based on the 'stifnesses' defined in equations (3.9) to (3.30a):

$$\mathbf{K}_{c_n}^{\text{tran}} = \sum_{j=1}^{N_i} (k_n - k_s)\,(\vec{p}_{b_i} \otimes \vec{p}_{b_i}) + k_s \mathbf{I} \tag{3.37}$$

$$\mathbf{K}_{c_n}^{\text{rot}} = \sum_{j=1}^{N_i} r_f^2 k_s\,(\mathbf{I} - \vec{p}_{b_i} \otimes \vec{p}_{b_i}) + k_t\,(\vec{p}_{b_i} \otimes \vec{p}_{b_i}) + k_b\,(\mathbf{I} - \vec{p}_{b_i} \otimes \vec{p}_{b_i}) \tag{3.38}$$

where in equations (3.37) and (3.38), k_n, k_s, k_t, k_b are the stiffnesses associated to the normal force, shear force, twisting moment and bending moment as described in the previous section. r_f is the fiber radius.
The maxima of the natural frequency $\omega_{\max}$ from the stiffness matrices are used to calculate the timestep:

$$\omega_{\max} = \max_{c_n} \left(\max\left(\omega_{c_n}^{\text{tran}}, \omega_{c_n}^{\text{rot}}\right)\right) \tag{3.39}$$

$$\Delta t_{sf} = \frac{2}{\sqrt{\omega_{max}}} \tag{3.40}$$

Since the computation of the stiffness matrices are quite involved, only the diagonal elements are calculated as these terms are dominant.

3.3 Finite volume solver

YALES2[117] is a massively parallel unstructured low Mach number solver primarily used for studying turbulent flows and combustion problems in complex geometries. Originally developed in CORIA lab, several research labs develop and maintain their own versions. YALES2 is written in object oriented Fortran and contains a suite of solvers and numerical methods to solve complex multiphysics problems. Within the context of this work, only the numerics of the incompressible solver are presented. The user defines a simulation by an input file (a bash script) with a .f90 'main' file for including user defined functions.
YALES2 follows a collocated cell-vertex based discretization, i.e.. the variables $\vec{U}, p, \text{grad}\,\vec{U}$ and scalars are stored in the nodes of the mesh and the control volumes are constructed around the nodes.

3.3.1 Finite Volume discretization

The 3D Incompressible Navier-Stokes equations (omitting the energy equation), consists of a momentum conservation equation and the mass conservation equation. The momentum conservation equation reads as

$$\underbrace{\frac{\partial \vec{U}}{\partial t}}_{\text{unsteady term}} + \underbrace{\vec{\nabla}\left(\vec{U} \otimes \vec{U}\right)}_{\text{convective term}} = \underbrace{\frac{-\vec{\nabla} \cdot p\mathbf{I}}{\rho}}_{\text{pressure grad.}} + \underbrace{\nu \vec{\nabla}^2 \vec{U}}_{\text{diffusion term}} + \underbrace{\frac{\vec{f}_b}{\rho}}_{\text{body forces}} \tag{3.41}$$

where in equation (3.41), ρ is the fluid density and ν the fluid kinematic viscosity. The continuity or the mass conservation equation reads as

$$\vec{\nabla} \cdot \vec{U} = 0 \tag{3.42}$$

Discretization of the Navier-Stokes equations begins with defining a polyhedral control volume Ω consisting of N_f faces

$$\frac{1}{V_p}\int_\Omega \frac{\partial \vec{U}}{\partial t} d\Omega + \frac{1}{V_p}\int_\Omega \vec{\nabla}.\left(\vec{U}\otimes\vec{U}\right) d\Omega = \frac{1}{V_p}\int_\Omega \frac{-\vec{\nabla}.p\mathbf{I}}{\rho} d\Omega + \frac{1}{V_p}\int_\Omega \nu\vec{\nabla}^2\vec{U} d\Omega + \frac{1}{V_p}\int_\Omega \frac{\vec{f_b}}{\rho} d\Omega \tag{3.43}$$

Rearranging and applying Gauss's theorem to equation (3.43) leads to

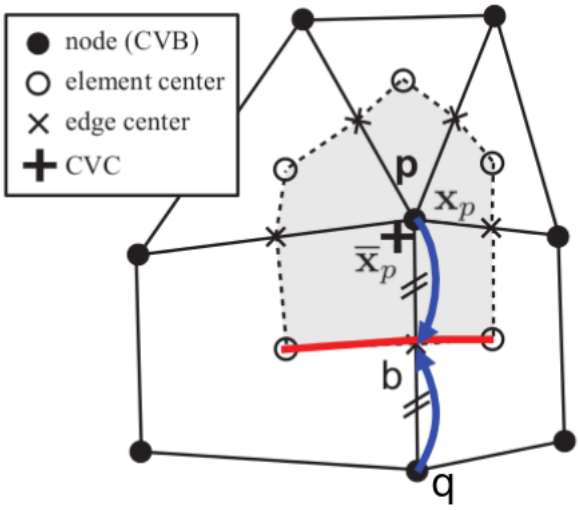

Figure 3.6: Control volume definition, from YALES2 training document.

$$\frac{1}{V_p}\int_\Omega \frac{\partial \vec{U}}{\partial t} d\Omega = \frac{1}{V_p}\int_{\partial\Omega}\left(-\left(\vec{U}\otimes\vec{U}\right) + \nu\vec{\nabla}\vec{U}\right)\vec{n}dA + \frac{1}{V_p}\int_\Omega \frac{-\vec{\nabla}p\mathbf{I}}{\rho} d\Omega + \frac{1}{V_p}\int_\Omega \frac{\vec{f_b}}{\rho} d\Omega \tag{3.44}$$

Representing the volume integral of $\vec{U}$ as

$$\vec{\bar{U}} = \frac{1}{V_p}\int_\Omega \vec{U} d\Omega \tag{3.45}$$

Rewriting (3.44) as

$$\frac{\vec{\bar{U}}(t+\Delta t) - \vec{\bar{U}}(t)}{\Delta t} = \frac{1}{V_p}\int_{\partial\Omega} \underbrace{\left(\left(-\vec{U}\otimes\vec{U}\right) + \nu\vec{\nabla}\vec{U} - \frac{p\mathbf{I}}{\rho}\right)}_{\text{surface forces}} \vec{n}dA + \frac{1}{V_p}\int_\Omega \underbrace{\frac{\vec{f_b}}{\rho}}_{\text{body forces}} d\Omega \tag{3.46}$$

The semi-discrete form of equation (3.46) is:

$$\frac{\vec{\bar{U}}(t+\Delta t) - \vec{\bar{U}}(t)}{\Delta t} = \frac{1}{V_p}\sum_{i=1}^{N_f}\int_{S_f} \underbrace{\left(\left(-\vec{U}\otimes\vec{U}\right) + \nu\vec{\nabla}\vec{U} - \frac{p\mathbf{I}}{\rho}\right)\vec{n}dA}_{\text{surface flux}\,\psi} + \frac{1}{\rho V_p}\vec{f}_b \tag{3.47}$$

From equation (3.47), ψ forms the surface flux across the cell face, the expression of a 2$^{\text{nd}}$ order accurate interpolation of this flux at the control volume boundary (CVB) b between p and q is (figure 3.6) :

$$\psi_b = \frac{\bar{\psi}(\Omega_p) + \bar{\psi}(\Omega_q)}{2} \tag{3.48}$$

Equation (3.48) is a nominally 2^{nd} order accurate, for irregular meshes consisting of tetrahedral and pyramid elements, the scheme is 1^{st} order accurate. In order to overcome the issue of accuracy, YALES2 includes a 4^{th} order accurate scheme. This spatial integration scheme was derived by a two step procedure. This scheme is derived using the following procedure:

- In the first step, the nodal values at p and q (figure 3.6) are calculated as volume averages at the barycenter of the control volume. Then a Taylor series expansion of the deconvolution of this function is then performed.
- the resulting expression of the nodal values are used to calculate the fluxes between the control volume boundary b.

Complete details of this procedure can be found in the study of Vantieghem [170] and Kraushaar [83].

3.3.2 Pressure correction

Since the flow is incompressible, it introduces an inherent decoupling between the pressure and velocity fields. In YALES2 the problem of decoupling is solved by using a modified version of the fractional step pressure projection method of Chorin [35]. The procedure involves decomposing the velocity field into two parts [87], a solenoidal part and an irrotational part (Hodge decomposition).

$$\vec{U} = \vec{U}_{\text{solenoidal}} + \vec{U}_{\text{irrotational}} \tag{3.49}$$

The irrotational vector field can be expressed as the gradient of scalar potential ϕ

$$\vec{U}_{\text{irrotational}} = \vec{\nabla}\phi \tag{3.50a}$$

The following vector identity holds

$$\vec{\nabla} \times \vec{U}_{\text{irrotational}} = \vec{\nabla} \times \left(\vec{\nabla}\phi\right) = 0 \tag{3.50b}$$

From equation (3.50b), $\vec{U}_{\text{solenoidal}}$ can be expressed as

$$\vec{U}_{\text{solenoidal}} = \vec{U} - \vec{\nabla}\phi \tag{3.50c}$$

$$\vec{\nabla}^2\phi = \vec{\nabla} \cdot \vec{U} \tag{3.50d}$$

The following procedure outlines the pressure-correction algorithm in YALES2

- The first step is to 'predict' a velocity field $\hat{\vec{U}}$ from semi-discrete form of equation (3.46),

$$\frac{\hat{\vec{U}} - \vec{U}^n}{\Delta t} = \psi_b - \frac{\vec{\nabla} P^{n-1/2}}{\rho} \tag{3.51}$$

  where in equation (3.51), the superscript n refers to the current time level.

- In the next step, an intermediate 'corrected velocity' $\vec{U}^*$ field is calculated from $\hat{\vec{U}}$ using the following expression

$$\frac{\vec{U}^* - \hat{\vec{U}}}{\Delta t} = -\frac{\vec{\nabla} P^{n-1/2}}{\rho} \tag{3.52}$$

- In the final step of the pressure correction, the velocity field is advanced to time level $n+1$ or at $(t+\Delta t)$ as

$$\frac{\vec{U}^{n+1}-\vec{U}^{*}}{\Delta t}=-\frac{\vec{\nabla}P^{n+1/2}}{\rho} \tag{3.53}$$

From equation (3.53), the pressure field at time level $n+1/2$ can be recovered by taking the divergence of equation (3.53) since the velocity field $\vec{U}^{n+1}$ is divergence free :

$$\vec{\nabla}^{2}P^{n+1/2}=\rho\frac{\vec{\nabla}\cdot\vec{U}^{*}}{\Delta t} \tag{3.54}$$

Equation (3.54), forms the pressure Poisson equation. In order to determine $P^{n+1/2}$ an algebraic linear equation system with dimensions equivalent to the number of nodes has to be solved. A brief description of the solution of the linear system is presented in section 3.3.4

3.3.3 Time advancement

A 4^{th}-order Runge Kutta like scheme is used for time integration in the fluid solver, with an implicit time-stepping scheme for the diffusive terms (see Kraushaar [83] for details). The stability is then controlled by the Courant-Friedrichs-Lewy (CFL) number, defined as,

$$\text{CFL}=|\vec{U}_f|\frac{\Delta t_f}{\Delta x}, \tag{3.55}$$

where $\vec{U}_f$ the fluid velocity, Δt_f the time step and Δx the mesh size. For each iteration, the time step is adapted to guarantee CFL < 1.

3.3.4 Linear solver

Equation (3.54) is the pressure-Poisson equation and for each node an algebraic expression is written. This results into a linear system of equations of the form

$$\mathbf{A}x=f \tag{3.56}$$

where in equation (3.56), $\mathbf{A}$ is a positive definite symmetric and sparse matrix with dimensions $n_c \times n_c$ with n_c being the number of nodes. Direct methods such as Gaussian elimination or LU factorization are expensive, therefore iterative algorithms are used. In the present study, all computations were performed using a variant of the Conjugate Gradient (CG) method known as the Deflated Preconditioned Conjugate Method (DPCG) method is used. Details on the method can be found in refs [173, 107].

3.4 FVM-DEM Coupling

One of the main objectives of the present work is to couple the DEM code YADE with the FVM code YALES2. The hydrodynamic force $\vec{F}_{\text{HYD}}$ and torques $\vec{T}_{\text{HYD}}$ are applied on the fiber segment and the feedback force from the fiber segment acts as a body force in the NS equations describing the fluid motion. In this section, the method of calculation of the hydrodynamic force and torque on the segment is presented, followed by a brief description of the technical implementation used in the present work. Finally the method of coupling the segment hydrodynamic force on the fluid cells is discussed.

3.4.1 Overview of the hydrodynamic force and torque on a fiber segment.

On a given fiber segment, the hydrodynamic forces and torques are calculated based on analytical expressions (see Chapter 4). The hydrodynamic force and torque on a fiber segment are functions of the relative velocity between fluid velocity and the orientation of the fiber segment.
Figure 3.7 shows a fiber segment b_i formed by the nodes c_n and c_{n-1} and the orientation of the segment is $\vec{p}_{b_i}$. For calculating the hydrodynamic force on the segment, the segment translational velocity is required. The segment velocity is calculated in the following way:

$$\vec{U}_{\text{seg}} = \frac{\vec{\dot{O}}_{c_{n-1}} + \vec{\dot{O}}_{c_n}}{2} \tag{3.57}$$

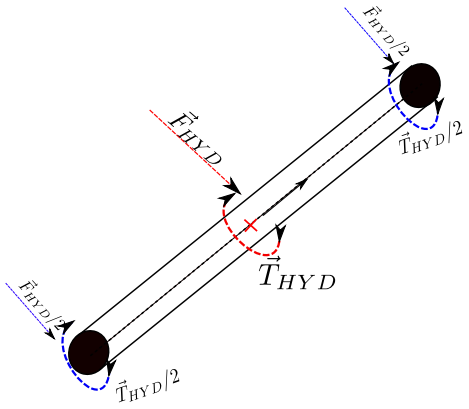

Figure 3.7: Application of hydrodynamic force and torque on a fiber segment.

The hydrodynamic force is then calculated using the following expression (for finite Reynolds numbers)

$$\vec{F}_{\text{HYD}} = \frac{1}{2}\rho C_D \left|\vec{U}_{\text{fluid}} - \vec{U}_{\text{seg}}\right| \left(\vec{U}_{\text{fluid}} - \vec{U}_{\text{seg}}\right) d_{\text{seg}} l_{\text{seg}} \tag{3.58}$$

where, l_{seg} and d_{seg} are the length and diameter of the fiber segment. The hydrodynamic torque on a fiber segment is calculated in the following manner:
The equation for the component of angular velocity of the fiber segment, parallel to the symmetric axis of the fiber segment reads as

$$\vec{\omega}_{\text{seg}_{\parallel}} = (\vec{\omega}_m . \vec{p_{b_i}}) . \vec{p_{b_i}} \tag{3.59}$$

where, $\vec{\omega}_m$ is given by $\vec{\omega}_m = 0.5(\vec{\omega}_{c_{n-1}} + \vec{\omega}_{c_n})$.
The equation for the component of angular velocity of the fiber segment, normal to the symmetric axis of the fiber segment reads as:

$$\vec{\omega}_{\text{seg}_{\perp}} = \left(\frac{\vec{\dot{O}}_{c_{n-1}} - \vec{\dot{O}}_{c_n}}{l_{\text{seg}}}\right) \times \vec{p_{b_i}} \tag{3.60}$$

Hence, the total angular velocity of the beam segment is

$$\vec{\omega}_{\text{seg}} = \vec{\omega}_{\text{seg}_{\perp}} + \vec{\omega}_{\text{seg}_{\parallel}} \tag{3.61}$$

The expression of the hydrodynamic torque on the fiber segment is

$$\vec{T}_{\text{HYD}} = \vec{T}_{\text{spin}} + \vec{T}_{\text{strain}} \tag{3.62}$$

where, $\vec{T}_{\text{spin}}$ is the component of the hydrodynamic torque due to the fluid vorticity and $\vec{T}_{\text{strain}}$ is the component of the hydrodynamic torque due to the straining motion of the fluid. Formulation of these torque components are expalined in Chapter 4.

3.4.2 Coupling Methodology

From equations (3.58) and (3.62), it is seen that the fluid velocity and the velocity gradient tensor of the fluid are required to compute the hydrodynamic force and torque on the fiber segment. In this section, discussion on the interpolation of these quantities from the fluid Eulerian grid to the Lagrangian fiber segments is done.

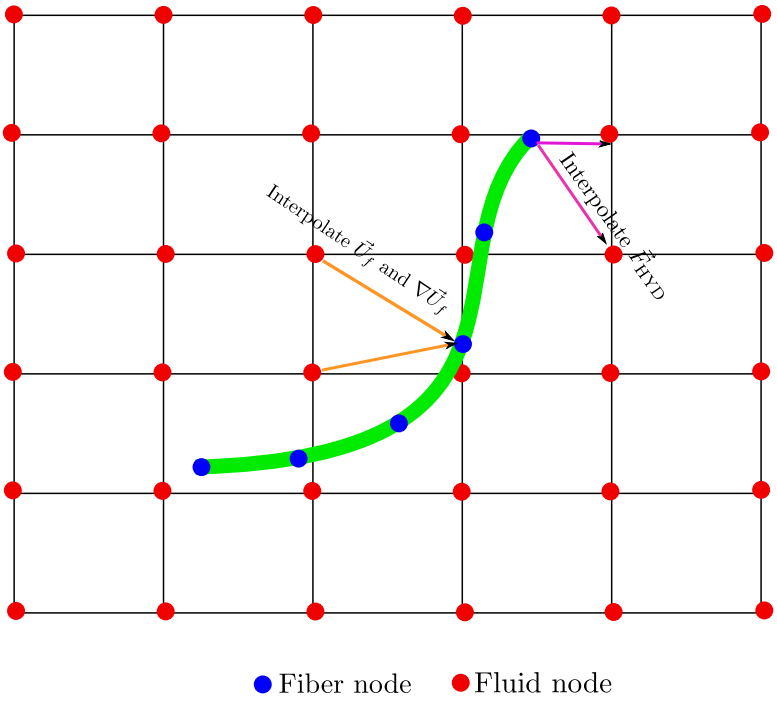

Figure 3.8: Graphical representation of the coupling. Fiber shown in green, fiber nodes shown in blue. Fluid grid in black lines and fluid nodes in red.

The coupling methodology involves managing the data exchange between the two solvers. YADE requires the velocity and velocity gradient tensor at a specific position in 3D space corresponding to the position of the fiber nodes and YALES2 requires the body force term from the fiber nodes. An overview of the coupling is shown is shown in figures 8.3 and 3.9.
YALES2 is a massively parallel code which is parallelized by the distributed memory paradigm of parallelization and uses Message Passing Interface (MPI) libraries. In this framework, each processor has its own memory space and the processor deals with the variables within this memory space. Variables between different processors are exchanged by sending and receiving messages using the MPI library. There are two types of communication, point-to-point communication which involves communication between two processors and collective communication in which variables are broadcast or gathered to one processor from several different processors.
Compared to standard single level domain decomposition, YALES2 follows a double domain decomposition. In this type of decomposition, at first the domain is split into several pieces based on optimal load balancing for each processor and the the overlap regions that participate in the inter-processor communication are marked. In the second level of the decomposition, within each processor the mesh is further divided into several 'cell groups' and each processor has an internal communicator as well as an external communicator. The internal communicator is responsible for maintaining the exchange and looping between these cell groups, whereas the external communicator collects the required data from the internal communicator and uses it for communication with the other processors. The METIS [76] library is used to generate the partitions based on an uni-directional graph data structure at both the levels.
The discrete element method is essentially an N-body simulation problem. For such problems,

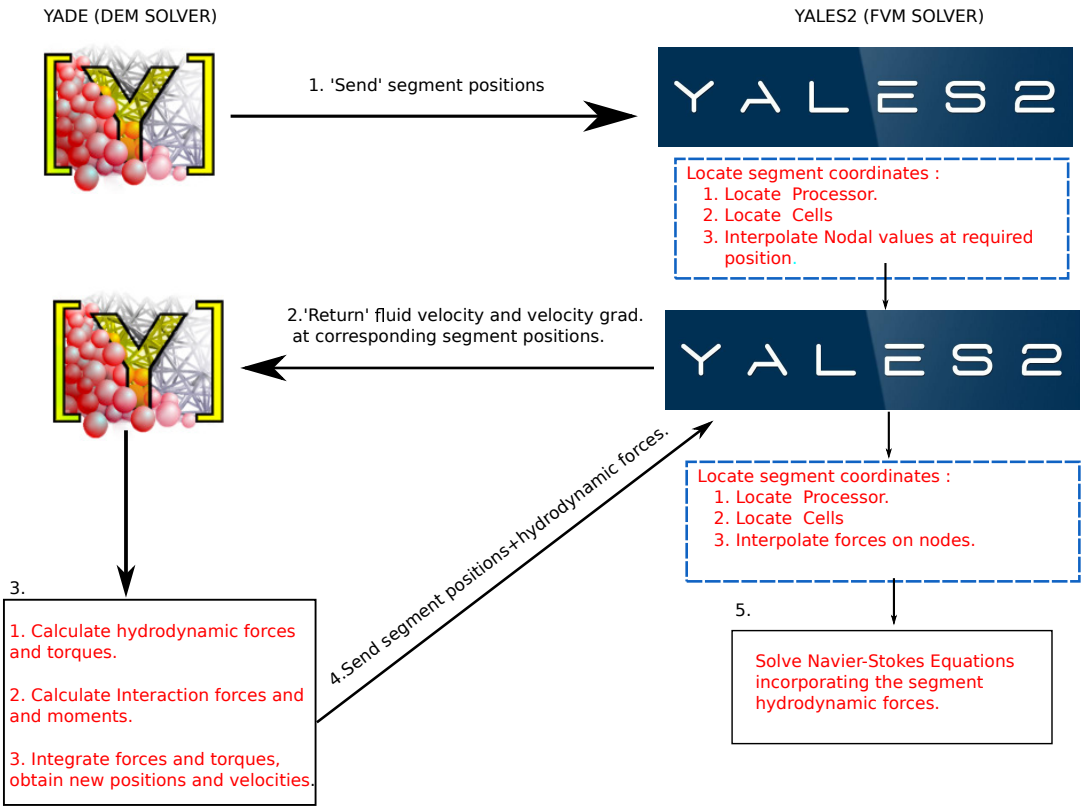

Figure 3.9: Simple schematic of the coupling between the codes YADE and YALES2.

distributed parallelization coupled with spatial domain decomposition is not well suited as there would be severe load imbalance between the processors. One could perform a domain decomposition for these problems by initially assigning the particles to the processors irrespective of the spatial location. This method looks quite attractive if there are long range interaction between the particles, however typical DEM problems involve short range interaction forces and for such problems this mode of decomposition would lead to large communication overheads between the processors. Parallelization in YADE is done based on the shared memory paradigm and the OpenMP library is used to achieve the parallelization. In this mode of parallelization, several cores have access to a single memory space. Building the lists of potential contacts and interaction forces based on this method is relatively efficient, since the looping through the particles can be split into several lightweight processes called threads and with the trend of increasing number of cores and larger RAM, this method of parallelization is quite attractive. However if one wishes to solve large scale problems involving millions of particles, MPI based domain decomposition parallelization would be efficient.

In the present coupling framework, a task-based parallelism approach is used. This is achieved by splitting the 'communicator' in the MPI framework. A collection of processors performing a single task forms a communicator and the default communicator is called `MPI_COMM_WORLD`. The default communicator is split into two, with one processor and communicator assigned to YADE and N_p processors assigned to YALES2 which forms the YALES2 communicator. YADE spawns OpenMP threads based on the number of available cores. One processor in the YALES2 communicator is called as the 'master' and manages the communication between the other processors in the YALES2 communicator. Furthermore YADE sends and receives data from the master processor of YALES2. Figure 3.10 shows an overview of the coupling scheme within one timestep.

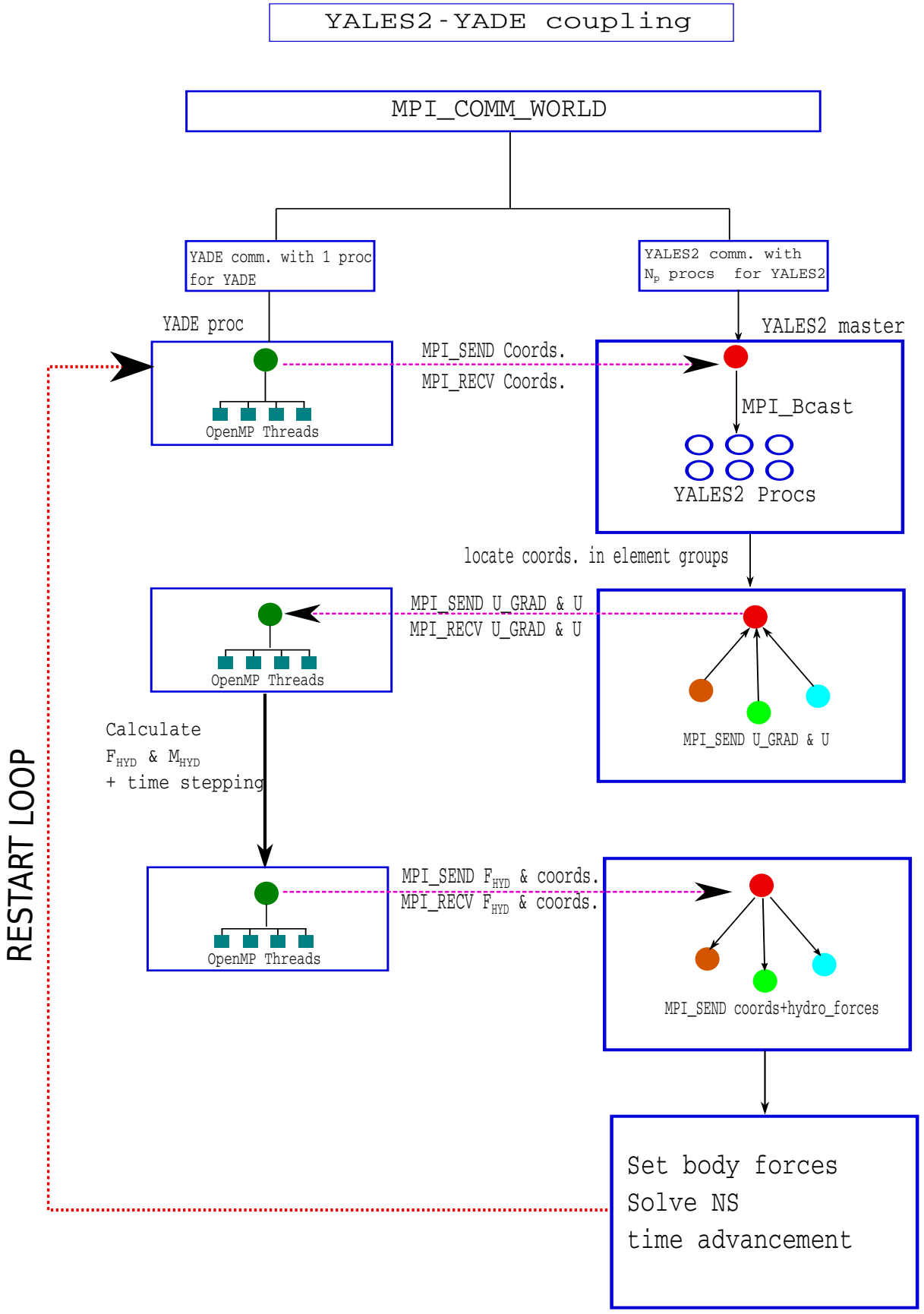

Figure 3.10: Flowchart of coupling between the codes YADE and YALES2.

3.4.3 Implementation

YADE runs under a Python environment and by default, majority of the C++ classes and variables are 'wrapped' at the lowest level i.e.. they behave as objects in a shared library which can be accessed and modified via a generic Python script. Since Python is used in the top level, Python can be used as a 'glue' to facilitate coupling between the two codes. YALES2 on the other hand uses Fortran 'main.f90' file which drives the simulation. A Fortran code can be called under Python environment by generating Python wrappers for the Fortran code. This is done by using the `f2py` module of the Numpy library in Python. Therefore one method of coupling is to write a piece of Fortran code that acts as an interface. The interface consists of the functions that provides the splitting of the `MPI` communicator, sending and receiving of data under the `MPI` environment (`MPI_SEND`,`MPI_RECV` `MPI_BROADCAST` etc.). This type of coupling is relatively simple to implement however it has some drawbacks. One of the main drawbacks is the dependency on the `f2py` and Numpy libraries as it is incapable of generating wrappers for modern object oriented Fortran codes utilizing derived data-types (similar to `struct` in C/C++)[2]. The other drawback of this method involves an internal conversion of datatypes i.e.. Fortran floats to Numpy floats and for large arrays it is inefficient. `f2py` is also notorious for memory-leaks during runtime, i.e.. earlier versions of `f2py` keeps a copy of the variable when it is passed between Fortran and Python, this leads to a growing memory consumption during runtime ultimately terminating the entire application.
Another approach for coupling the codes is based on mixed language programming. This involves in exposing Fortran functions in C++ or vice versa. This method is similar to the previous approach but instead of using Python to maintain the coupling/communication between the codes, a low level coupling is achieved by calling Fortran functions in C++ or vice versa. This leads to an efficient and fast data exchanges. However, careful implementation should be done in order to avoid unexpected 'segmentation faults'. The function prototype of the external Fortran functions are declared in the `.hpp` header file using the `extern` keyword and the associated datatype buffers (no support for `struct` datatypes). This mode of coupling is used throughout in this thesis.

The coupling algorithm is as follows (from figure 3.10):

- The communicator `MPI_COMM_WORLD` is split into two. YADE forms a communicator space with one processor and YALES2 forms a separate communicator with its group of processors.
- The fiber segment coordinates are collected in an array and sent to the YALES2 master processor using the `MPI_SEND` function. YALES2 master processor receives the segment coordinates (`MPI_RECV`).
- The YALES2 master processor performs a broadcast using the `MPI_BROADCAST` function, the other processors receive the segment coordinates.
  - Each processor loops through its element groups and performs a search for the coordinates based on a min-max method in a tree like data structure.
  - Once the element containing the segment is found, the values of the velocity vector and velocity gradient tensor is interpolated and sent to the master processor.
- YALES2 master sends the velocity vector and velocity gradient tensor corresponding to the segment position to YADE by a `MPI_SEND/RECV` function. YADE calculates the hydrodynamic forces and torque for each segment and calculates the new position of segments for a prescribed number of timesteps.

[2]There is a library called `f90wrap` which overcomes this limitation, during the development of the coupling `f90wrap` was in its nascent stage ca. early 2015

- YADE sends the new segment positions and corresponding hydrodynamic forces to YALES2 by the `MPI_SEND/RECV` function.
  - The velocity-source/body force term in the NS equations are initialized to zero. YALES2 master processor broadcasts the segment position and hydrodynamic forces.
  - A search in the element group of each processor is performed, once the segment position is located the hydrodynamic forces are interpolated to the nodes of the element containing the fiber segment.
- The NS equations are solved based on the algorithm presented in the previous section incorporating the velocity-source term and the loop continues until the desired number of timesteps or time is reached.

Compared to typical CFD-DEM coupling [179, 81], the present coupling numerical model differs in the scale of particle-grid resolution and particle volume fraction. In standard CFD-DEM methods, the particle concentration is higher than 10% and the effect of this volume concentration is incorporated in to the NS equations, whereas in the present study the fiber volume fraction at maximum is 5%. Furthermore the particles are several times smaller than the fluid element size. In the present work, the segment sizes and the fluid elements have comparable dimensions (usually the segment length is kept 1 to 2 times the fluid element edge length). This method is quite expensive, however it provides better resolution and for low Reynolds numbers the subgrid scales are resolved within the fiber segment length.
The hydrodynamic forces on the fluid element nodes are interpolated using a method similar to the work of Lindström and Uesaka [97]. Using this interpolation scheme, the force exerted by one fiber segment on one fluid cell is distributed over the fluid cell nodes in such a way that:

- The sum of the interpolated forces is equal to the force itself.
- At each cell node, the moment of the interpolated forces is equal to the force itself.

Consider a hexahedral element with nodes labeled as (i,j,k), $(i+1,j,k)\cdots$ and so on. $\vec{x}_p = (x_p, y_p, z_p)$ be the position vector of the fiber segment from the node (i,j,k). The weighting function for each node is as follows:

$$W_{i,j,k}(x_p,y_p,z_p) = \frac{x_{i+1}-x_p}{\Delta x}\cdot\frac{y_{i+1}-y_p}{\Delta y}\cdot\frac{z_{i+1}-z_p}{\Delta z} \tag{3.63a}$$

$$W_{i+1,j,k}(x_p,y_p,z_p) = \frac{x_p}{\Delta x}\cdot\frac{y_{i+1}-y_p}{\Delta y}\cdot\frac{z_{i+1}-z_p}{\Delta z} \tag{3.63b}$$

$$W_{i+1,j+1,k}(x_p,y_p,z_p) = \frac{x_p}{\Delta x}\cdot\frac{y_p}{\Delta y}\cdot\frac{z_{i+1}-z_p}{\Delta z} \tag{3.63c}$$

$$W_{i,j+1,k}(x_p,y_p,z_p) = \frac{x_{i+1}-x_p}{\Delta x}\cdot\frac{y_p}{\Delta y}\cdot\frac{z_{i+1}-z_p}{\Delta z} \tag{3.63d}$$

$$W_{i,j,k+1}(x_p,y_p,z_p) = \frac{x_{i+1}-x_p}{\Delta x}\cdot\frac{y_{i+1}-y_p}{\Delta y}\cdot\frac{z_p}{\Delta z} \tag{3.63e}$$

$$W_{i+1,j,k+1}(x_p,y_p,z_p) = \frac{x_p}{\Delta x}\cdot\frac{y_{i+1}-y_p}{\Delta y}\cdot\frac{z_p}{\Delta z} \tag{3.63f}$$

$$W_{i,j+1,k+1}(x_p,y_p,z_p) = \frac{x_{i+1}-x_p}{\Delta x}\cdot\frac{y_p}{\Delta y}\cdot\frac{z_p}{\Delta z} \tag{3.63g}$$

$$W_{i+1,j+1,k+1}(x_p,y_p,z_p) = \frac{x_p}{\Delta x}\cdot\frac{y_p}{\Delta y}\cdot\frac{z_p}{\Delta z} \tag{3.63h}$$

The hydrodynamic force $\vec{F}_{\text{hyd}}$ is distributed to the nodes based on the volumetric weighting function from equation (3.63). For example for node (i, j, k), the hydrodynamic force is

$$\widetilde{\vec{F}_{\text{hyd}_{i,j,k}}} = \frac{\vec{F}_{\text{hyd}} W_{i,j,k}(x_p, y_p, z_p)}{\rho_f \Delta V_f} \tag{3.64}$$

Figures 3.11 and 3.12 shows the geometric representation of the force distribution in 2 dimensions. In figure 3.11, the hydrodynamic force $\vec{F}_h$ from the fiber segment center P is to be distributed to the four nodes of the quadilateral fluid cell as

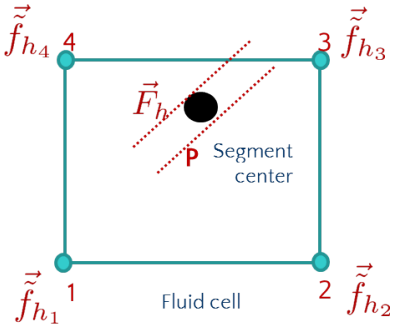

Figure 3.11: Schematic of the force interpolation in 2D.

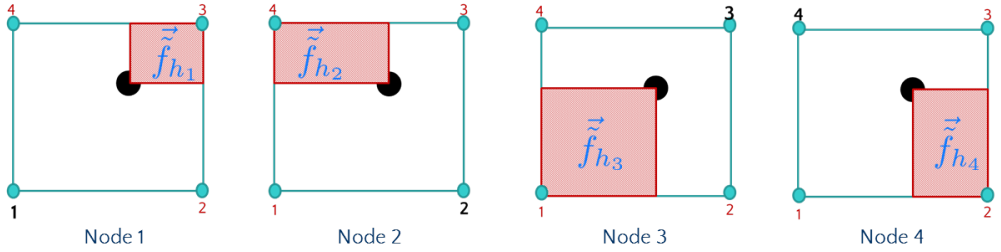

Figure 3.12: Geometric representation of the force interpolation by means of area weighted average in 2D.

In the case of tetrahedral elements, the same approach is used. Consider a tetrahedral element with the nodes $n_1 = (x_1, y_1, z_1)$, $n_2 = (x_2, y_2, z_2)$, $n_3 = (x_3, y_3, z_3)$ and $n_4 = (x_4, y_4, z_4)$. $p = (x_p, y_p, z_p)$ is the position of the segment and Ω_{1234} be the volume of the tetrahedral element. The weighting function for node n_1 is

$$W_{n_1}(p) = \frac{\Omega_{p234}}{\Omega_{1234}} \tag{3.65}$$

where in equation (3.65), Ω_{p234} is the volume of the tetrahedron formed by the segment center and the other nodes n_2, n_3 and n_4. For other nodes, the same expression applies. The hydrodynamic force on the node is calculated based on expression (3.64) :

$$\widetilde{\vec{F}_{\text{hyd}_{n,i}}} = \frac{\vec{F}_{\text{hyd}} W_{n,i}}{\rho_f \Delta V_f} \tag{3.66}$$

3.4.4 Coupled FVM-DEM numerical stability

The equations of motion presented for a given fiber segment node can be written as a spring-mass system. However, the presence of a fluid damps the motion of the fiber nodes [32], hence a spring-mass damper system equation for a given node c_n can be written as

$$m_{c_n}\{\ddot{\vec{O}}_{c_n}\} + [\mathbf{V}_{c_n}]\{\dot{\vec{O}}_{c_n}\} + [\mathbf{K}_{c_n}]\{\vec{O}_{c_n}\} = 0 \tag{3.67}$$

where in equation (3.67) m_{c_n} is the mass of the node, $\mathbf{V}_{c_n}$ is the viscosity matrix consisting of the hydrodynamic force coefficients and $\mathbf{K}_{c_n}$ the segment stiffness matrix. From equation (3.67) a critical timestep Δt_{df} can be derived for the viscosity dominated regime (negligible stiffness).

$$m_{c_n}\{\ddot{\vec{O}}_{c_n}\} + [\mathbf{V}_{c_n}]\{\dot{\vec{O}}_{c_n}\} = 0 \tag{3.68}$$

where $\mathbf{V}_{c_n}$ is a 3×3 diagonal matrix with the scalar hydrodynamic force coefficients $\zeta_{\parallel}$, $\zeta_{\perp}$ and $\zeta_{\perp}$ as the diagonal elements

$$\zeta_{\parallel} = \frac{1}{2}\rho_f C_l d_f l_{seg} \left|\vec{U}_f - \vec{U}_{seg}\right|, \tag{3.69a}$$

$$\zeta_{\perp} = \frac{1}{2}\rho_f C_n d_f l_{seg} \left|\vec{U}_f - \vec{U}_{seg}\right|. \tag{3.69b}$$

Writing equation (3.68) in the discrete form for one direction , one obtains:

$$\frac{\dot{\vec{O}}_{c_n}(t+\Delta t) - \dot{\vec{O}}_{c_n}(t)}{\Delta t} = -\frac{V_{c_{n_{i,j}}}(t)}{m_{c_n}}\dot{\vec{O}}_{c_n}(t) \tag{3.70a}$$

and

$$\dot{\vec{O}}_{c_n}(t+\Delta t) = \left(1 - \frac{V_{c_{n_{i,j}}}}{m_{c_n}}\Delta t\right)\dot{\vec{O}}_{c_n}(t) \tag{3.70b}$$

where equation (3.70) reflects the integration of equation (3.68) by the explicit time stepping algorithm in use.
The stability of an explicit integration scheme is ensured by imposing the condition [32]:

$$\left|1 - \frac{\max(\mathbf{V}_{c_n})}{m_{c_n}}\Delta t\right| \leq 1. \tag{3.71}$$

Hence from equation (3.71), the criterion for a stable timestep is deduced as:

$$\Delta t_{df} < 2 \cdot \min_{c_n}\left(\frac{m_{c_n}}{\max(\mathbf{V}_{c_n})}\right). \tag{3.72}$$

3.4.5 Coupling timescale

From the previous discussions, three critical timesteps pertaining to the DEM solver, FVM solver and the coupled scheme has been presented. In the present section, the 'coupling' time is presented. The timestep of the DEM solver depends on the particle size, stiffness (Young's modulus) and density of the material. The fibers in the present work are assumed to have diameters in the order of μm and the Young's modulus varies from few MPa to tens of GPa. This leads to extremely stiff systems rendering the typical timestep Δt_{sf} of the DEM solver in the order of $10^{-7}s$ to $10^{-9}s$. For the fluid solver, two timesteps are present: a timestep based on the advection of the flow and a timestep for the diffusive component. For turbulent and finite *flow Reynolds numbers*, the viscous/diffusive timesteps are in the order of $10^{-8}s$ to $10^{-4}s$ and the convective timesteps range from $10^{-5}s$ to $10^{-2}s$, (at CFL=1). As mentioned in section 3.3.3, the constraint of extremely small timesteps arising from the diffusion process is overcome by using implicit schemes and therefore a timescale for the fluid solver is fixed based on the convective timetstep Δt_f. In section 3.4.4, a timestep Δt_{df} for the coupling has beeen presented. This timestep can be considered in an intermediate region between the fluid and particle timescales,

i.e. the coupling timestep is higher than the standard DEM solver timestep but less than the fluid solver : $\Delta t_{sf} < \Delta t_{df} < \Delta t_{\text{fluid}}$. In the present work, the DEM solver is run until it approaches Δt_{df}, at this time the data exchange is done. In the fluid solver the CFL number is set to a value that correpsonds to Δt_{df}. For Stokesian force models such as the slender body theory and prolate-spheroid model (discussed in detail in Chapter 4), the fluid velocity at the current timestep is used. Owing to the non-linearity of the drag force in finite Reynolds numbers, the hydrodynamic force is calculated using the fluid velocity from the previous timestep.

3.5 Conclusion

The governing equations and the numerical methods of the fiber phase and the fluid phase have been discussed. YADE an open-source DEM solver is used for solving the equations of fiber motion and a high fidelity finite volume solver YALES2 is used for the numerical solution of the Navier-Stokes equations of the fluid phase. Interphase coupling is achieved by incorporating the fiber hydrodynamic force as a velocity-source term in the NS equations and the methodology of the communication between the solvers has been presented. Numerical stability of each numerical method is presented and finally the stability of the coupled FVM-DEM has also been presented.

CHAPTER 4

HYDRODYNAMIC FORCE AND TORQUE MODELS

Contents

4.1 Introduction

This chapter is primarily concerned with the various force formulations applicable for flexible fibers within a bead-rod framework. The chapter begins with implementations of some previous force models used. Their implication in using them in the present fiber discretization framework is examined. A hydrodynamic force model based on the 'force per unit length' on an infinite cylinder model for various Reynolds numbers is introduced and its applicability is discussed. The chapter closes with a formulation for the hydrodynamic torque in a 'per unit length' fashion. This hydrodynamic torque was developed from explicit CFD simulations of a high aspect ratio cylinder in a shear flow.

4.2 Preliminaries

In this section, we describe the definitions of the hydrodynamic force coefficients used in this chapter and throughout this work.
The total hydrodynamic force $\vec{F}_{\text{hyd}}$ acting on the surface of a particle is defined as:

$$\vec{F}_{\text{hyd}} = \int_{s_p} \boldsymbol{\sigma}.\vec{n}dS \tag{4.1}$$

where $\boldsymbol{\sigma}$ is the total hydrodynamic stress. This stress $\boldsymbol{\sigma}$ can be decomposed into:

$$\boldsymbol{\sigma} = -p\mathbf{I} + \boldsymbol{\tau}. \tag{4.2}$$

In equation (4.2) p is the absolute pressure, $\mathbf{I}$ is the unit tensor, and $\boldsymbol{\tau}$ is the viscous stress tensor. The viscous stress tensor $\boldsymbol{\tau}$ is defined as :

$$\boldsymbol{\tau} = 2\mu\mathbf{E}. \tag{4.3}$$

In equation (4.3), μ is the fluid dynamic viscosity. $\mathbf{E}$ is the strain rate tensor, which is defined as:

$$\mathbf{E} = \frac{1}{2}\left((\nabla\vec{U}_f) + (\nabla\vec{U}_f)^T\right) \tag{4.4}$$

where in equation (4.4), $\vec{U}_f$ is the fluid velocity.
The Reynolds number is defined as the ratio of inertial force to viscous force. In the present study the Reynolds number is based on the fibre diameter as follows:

$$Re_p = \frac{\rho_\mathrm{f}|\vec{U}_n|d_\mathrm{fib}}{\mu} \tag{4.5}$$

where ρ_f is the fluid density, and $\vec{U}_n$ is the component of the relative velocity normal to the symmetry axis of the fiber segment. For low Reynolds numbers ($Re_p < 0.01$), a Stokesian formulation of the force is used:

$$\vec{F}_\mathrm{hyd} = \mu_f\mathbf{A}\left(\vec{U}_f - \vec{U}_\mathrm{seg}\right) \tag{4.6}$$

where $\mathbf{A}$ is the hydrodynamic resistance tensor of the particle. For higher Reynolds numbers, the following non-linear formulation is used :

$$\vec{F}_n = \frac{1}{2}\rho_\mathrm{fl}C_n d_\mathrm{fib}l_\mathrm{seg}|\vec{U}_\mathrm{abs}|\left(\vec{U}_{f_\perp} - \vec{U}_{\mathrm{seg}_\perp}\right) \tag{4.7a}$$

$$\vec{F}_l = \frac{1}{2}\rho_\mathrm{fl}C_l d_\mathrm{fib}l_\mathrm{seg}|\vec{U}_\mathrm{abs}|\left(\vec{U}_{f_\parallel} - \vec{U}_{\mathrm{seg}_\parallel}\right) \tag{4.7b}$$

$$\vec{F}_\mathrm{hyd} = \vec{F}_n + \vec{F}_l \tag{4.7c}$$

In equation (4.7), $\vec{F}_l$ is the component of the hydrodynamic force parallel to the fiber segment symmetric axis (longitudinal component). $\vec{F}_n$ is the component normal to the symmetry axis. C_n and C_l are the hydrodynamic force coefficients for the normal and longitudinal directions (equations (4.7a) and (4.7b)). Details of the force coefficients are presented in the later sections. The total hydrodynamic torque at the hydrodynamic center of the particle is defined as

$$\vec{T}_O = \int_{s_p} \vec{r} \times \boldsymbol{\sigma}.\vec{n}dS \tag{4.8}$$

where $\vec{r}$ is the vector from the center of the particle to the particle surface. The torque due to the rotational velocities of fluid and the fiber (at the hydrodynamic center) is defined as :

$$\vec{T}_R = \mu C_R(\vec{\omega}_f - \vec{\omega}_p) \tag{4.9}$$

Torque due to the strain-rate tensor/deformation of the fluid (at the hydrodynamic center) is defined as :

$$\vec{T}_S = \mu C_S\left(\boldsymbol{\epsilon}\cdot(\vec{p}\otimes\vec{p})\right) : \mathbf{E} \tag{4.10}$$

where in equation (4.9) C_R is a resistance tensor depending upon the particle shape and orientation and in (4.10), and C_S is resistance scalar based on the particle shape and $\boldsymbol{\epsilon}$ is the Levi-Civita symbol.

4.3 The prolate spheroid model

The prolate-spheroid model was used in the studies of Schmid *et al.* [144], Lindström and Uesaka [97] and Skjetene *et al.* [154]. In their studies, a fiber was modeled as a chain of cylinders with hemispherical end caps. The hydrodynamic force on these segments are approximated by 'equivalent' prolate spheroid. The hydrodynamic force formulation on these spheroids is based on Jeffery's results [70] and has been presented in the work of Kim and Karilla [80].
The hydrodynamic force and torque on a prolate-spheroid [80] is written as follows :

$$\vec{F}_{\text{hyd}} = 6\pi\mu a \left[X^A\,(\vec{p}\otimes\vec{p}) + Y^A(\boldsymbol{\delta} - (\vec{p}\otimes\vec{p}))\right].\left(\vec{U}_f - \vec{U}_{\text{seg}}\right) \tag{4.11}$$

$$\vec{T}_{\text{hyd}} = 8\pi\mu a^3 \left[X^C\,(\vec{p}\otimes\vec{p}) + Y^C(\boldsymbol{\delta} - (\vec{p}\otimes\vec{p}))\right].(\vec{\omega}_f - \vec{\omega}_{\text{seg}}) - 8\pi\mu a^3 Y^H\,(\boldsymbol{\epsilon}.(\vec{p}\otimes\vec{p})) : \mathbf{E} \tag{4.12}$$

where in equations (4.11) and (4.12), $a = l_{\text{seg}}/2$ is half the segment length, μ is the dynamic viscosity of the fluid. X^A,Y^A,X^C,Y^C,Y^H are the hydrodynamic scalar resistance functions which are based on the geometry of the spheroid.

$$X^A = \frac{8}{3}e^3\left[-2e + (1+e^2)L\right]^{-1} \tag{4.13a}$$

$$Y^A = \frac{16}{3}e^3\left[2e + (3e^2-1)L\right]^{-1} \tag{4.13b}$$

$$X^C = \frac{4}{3}e^3(1-e^2)\left[2e - (1-e^2)L\right]^{-1} \tag{4.13c}$$

$$Y^C = \frac{4}{3}e^2(2-e^2)\left[-2e + (1+e^2)L\right]^{-1} \tag{4.13d}$$

$$Y^H = \frac{4}{3}e^5\left[-2e + (1+e^2)L\right]^{-1} \tag{4.13e}$$

$$L(e) = \ln\left(\frac{1+e}{1-e}\right) \tag{4.13f}$$

where e is the eccentricity of the spheroid. When using such a model for fibers with cylindrical shapes, a question of defining the value of e arises. Schmid *et al.* [144] defined an effective aspect ratio r_e of the spheroid relating the segments aspect ratio r_p based on Bretherton's results [24] $r_e = 0.7r_p$. The eccentricity was then defined as:

$$e = \sqrt{1 - \frac{1}{r_e^2}} \tag{4.13g}$$

It should be noted that the eccentricity in all these studies (Schmid *et al.* [144] and Lindström and Uesaka [97]) was defined for the fiber segment and not for the entire fiber.
In the work of Lindström and Uesaka [97], the diameter of the equivalent spheroid d_{spheroid} was calculated from the semi-empirical expression derived by Cox [41],

$$d_{\text{spheroid}} = \frac{1}{1.24}d_f\left(\ln\frac{l_{\text{seg}}}{d_f}\right)^{1/2} \tag{4.14}$$

Equation (4.14) is valid for slender bodies with high aspect ratio ($r_p > 10$) and is not accurate when the aspect ratio of the segment is short. As a first case study, the prolate spheroid hydrodynamic force model was implemented and tested. A rigid fiber is placed under a shear flow

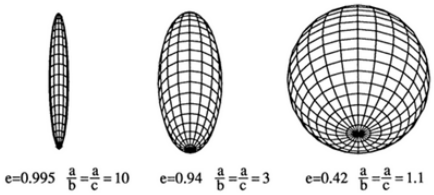

Figure 4.1: Spheroid shape based on e, from ref [80]

and the motion of the fiber is compared with Jeffery's theory. Fibers with different aspect ratios ranging from 25 to 200 are tested with two-way coupling. The effective aspect ratio of the fiber segments were calculated using equation (4.14) and the eccentricity from (4.13g). For rigid fibers the Young's modulus was varied from 8 to 20 GPa (higher Young's modulus for higher r_p). Table 4.1 shows the details of the fiber discretization for different r_p .

r_p	N_{seg}
12	6
25	12
32	15
50	20
80	30
100	50
200	60

Table 4.1: Fiber discretization.

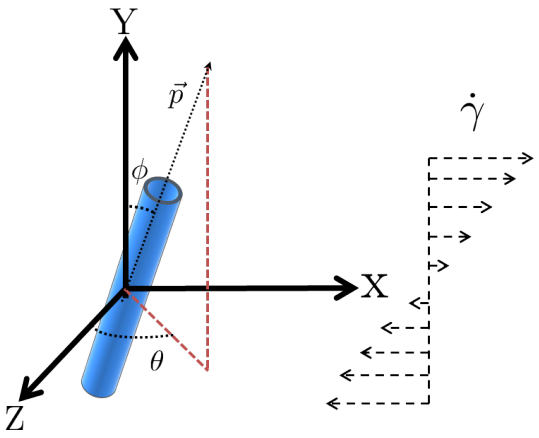

Figure 4.2: Rigid fiber in a shear flow (shear in XY plane).

Figure 4.2 shows the schematic of the numerical simulation. ϕ is the angle between the symmetric axis of the fiber and the velocity gradient direction. θ is the angle between the vorticity axis and the projection of the fiber symmetric axis on the vorticity plane. For a fiber depicted in figure 4.2, Jeffery [70] derived the time period of the rotation of an ellipsoid:

$$T_p = \frac{2\pi\dot{\gamma}}{r_e + \frac{1}{r_e}} \tag{4.15}$$

where $\dot{\gamma}$, is the shear rate and r_e is the the aspect ratio of the ellipsoid. In the present study, r_e is the effective aspect ratio. For a finite cylinder with aspect ratio r_p, r_e was calculated using

the equation derived by Cox [41]:

$$r_e = 1.24 r_p \frac{1}{\sqrt{\ln r_p}} \tag{4.16}$$

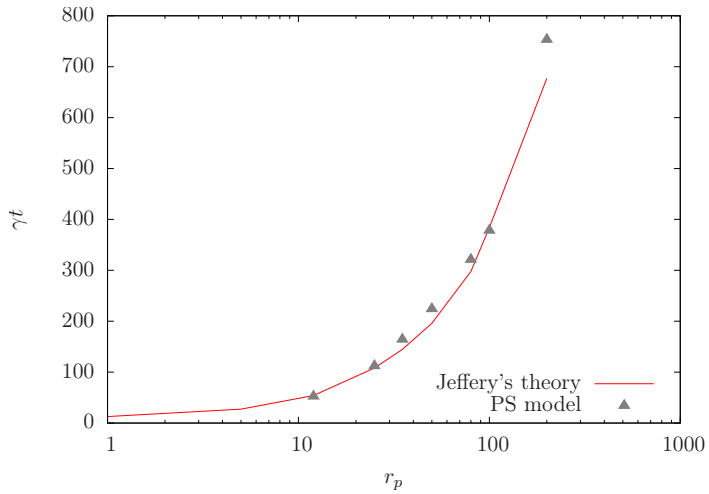

Figure 4.3: Comparison of angular displacement with Jeffery's theory for rigid fibers with different aspect ratios.

Figure 4.3 shows the comparison of the non-dimensional orbit period $\dot{\gamma}T$ with respect to the aspect ratio r_p. The eccentricity of the segments were fine-tuned in this case. The effect of varying the number of segments is shown in figure 4.4.
Figure 4.4 shows the comparison of angular displacement ϕ with respect to time obtained from the prolate spheroid (PS) model and the analytical solution of Jeffery (eq. (4.15)). From the figure it is observed that the numerical solutions are dependent on the number of segments. This is the major inconsistency of the PS model.

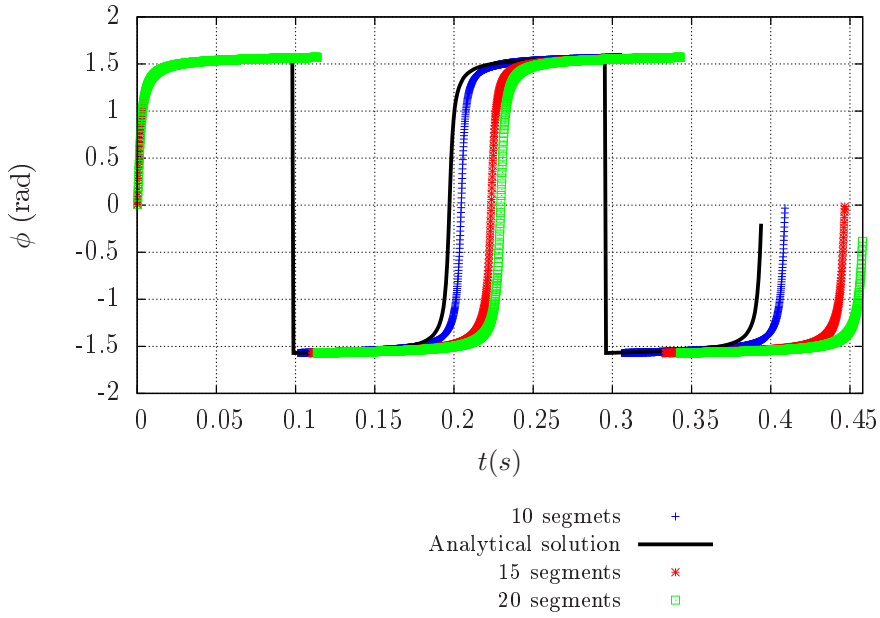

Figure 4.4: Comparison of angular displacement with Jeffery's theory. Fiber $r_p = 50$, $\dot{\gamma} = 500$

The Bending number (BR) is a non-dimensional number that characterizes the flexibility of a

fiber in shear flow [63, 58]. The expression of BR is

$$\mathrm{BR} = \frac{E\left(\ln(2r_p) - 1.50\right)}{2\mu\dot{\gamma}r_p^4} \tag{4.17}$$

In equation (4.17), E is the fiber Young's modulus. For $BR > 10$ the fibers are considered as rigid, and as the BR decreases, the fibers are seen as flexible.

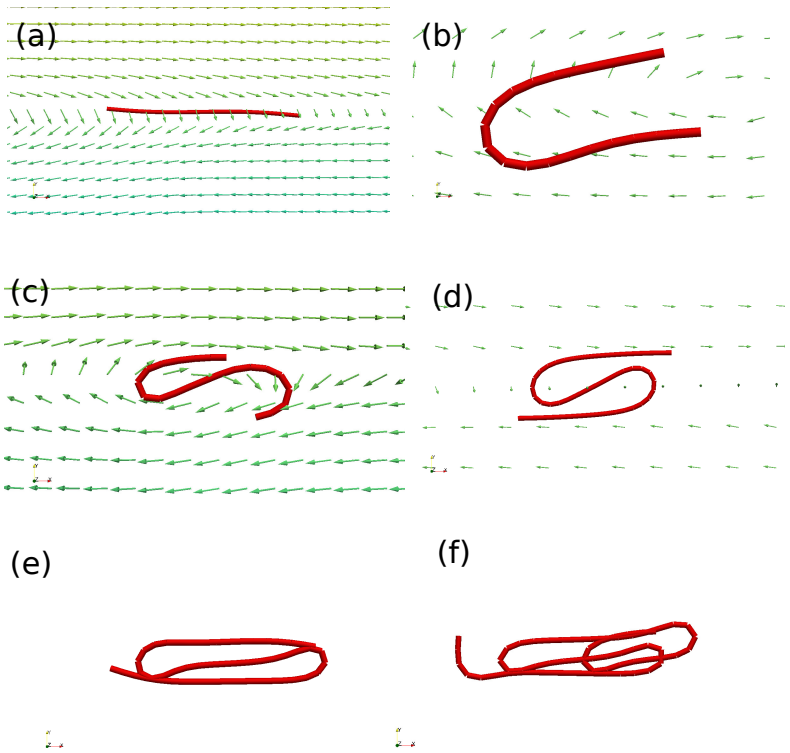

Figure 4.5: Deformation of flexible fibers in a shear flow, shear in XY plane. *(a)* $BR = 0.80$. *(b)* $BR = 0.04$. *(c)* $BR = 0.0075$. *(d)* $BR = 8.5 \times 10^{-4}$. *(e)* $BR = 5.1 \times 10^{-4}$. *(f)* $BR = 1.1 \times 10^{-4}$. Vectors in green show the disturbance produced by the fiber.

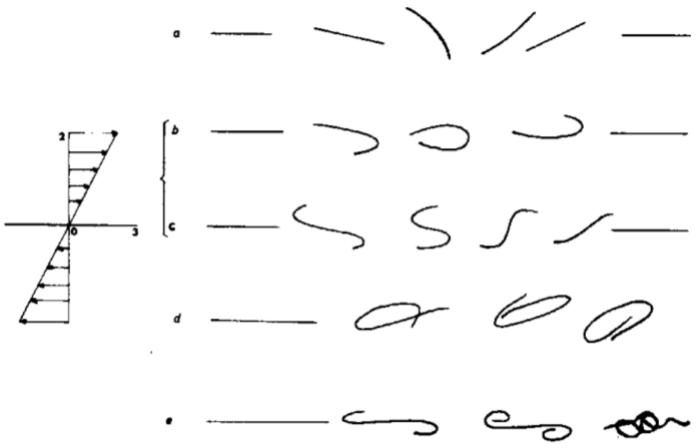

Figure 4.6: Deformation of fibers observed in the experiments of Salinas and Pitman [142]

The deformation of a flexible fiber in a shear flow for varying bending numbers was studied. The results of the fiber deformation is shown in figure 4.5. Figure 4.6 shows the experimental

observations obtained by Salinas and Pitman [142]. From the figures it is observed that the results obtained by the PS hydrodynamic model is in reasonable agreement with the experimental observations.

4.4 Slender body theory

The slender body theory was derived by Batchelor [12] and Cox [41]. Keller and Rubinow [77] introduced the non-local slender body theory. The slender body theory derives asymptotic solutions for particles having large aspect ratios ($r_p > 10$). Since the slender body theory is derived based on the Stokes equations in which the inertial terms of the NS equations are neglected, it does not aim to solve the Stokes paradox. The slender body theory assumes a distribution of point forces and torques on axisymmetric particles called as 'stokeslets' and 'rotlets'. Let b be the semi-length of the particle, a be the width/radius particle, slender body theory aims to derive the pointforce distribution for an axisymmetric body with $a/b \to 0$. An asymptotic expansion of the Stokes equation based on $k = a/b$ is employed at the vicinity of the particle to satisfy the no-slip boundary condition known as the 'inner expansion'. The 'outer expansion', is based on the parameter k and aims to satisfy the free stream velocity boundary condition based on the Stokes equation but in the absence of the slender body. (see Cox [41] page 797)
The force per unit length/force distribution on an axisymmetric particle derived from the slender body theory is :

$$\vec{f} = 4\pi k\mu \left(\boldsymbol{\delta} - \frac{1}{2} \left(\vec{p} \otimes \vec{p} \right) \right) \vec{V} \tag{4.18}$$

from equation (4.18), the force per unit length parallel to symmetric axis of the particle is :

$$f^{\parallel} = \frac{4\pi\mu}{ln(2r_p) + 0.5} V_{\parallel} \tag{4.19}$$

and the force per unit length normal to the symmetric axis :

$$f^{\perp} = \frac{8\pi\mu}{ln(2r_p) + 0.5} V_{\perp} \tag{4.20}$$

The slender body theory in the form of equations (4.19) and (4.20) is not directly applicable in the present numerical methods, as there remains questions on the definition of the aspect ratio r_p for flexible fibers.

4.5 Force per unit length on an Infinite Cylinder

Stokes Paradox: Based on the Stokes equations, it is impossible to derive the force per unit length on an infinite cylinder, i.e. there exists no 2D creeping flow past a circular cylinder which satisfies both the no-slip boundary condition on the surface of the cylinder, and the free-stream velocity boundary condition in an unbounded domain because the effect of the cylinder on the fluid exists at very large distances from the cylinder boundary and Re tends to be $O(1)$. Hence the inertial terms are not negligible. Oseen [121] linearized the inertial terms of the NS equations and formed the Oseen-Stokes equations and solved the flow past a sphere for higher Re, Lamb [88] explains that the linearization of Oseen[121] is not true and re-formulated the Oseen-Stokes equation and derived the force per unit length on an infinite cylinder. Tomotika *et al.* [164] derived the force per unit length for oblique infinite cylinders by expanding the Oseen-Stokes equations in terms of Bessel functions for $Re < 4$. Proudmann and Pearson [133] and Kaplun [75] derived the force per unit length by the rigourous mathematical method of Matched Asymptotic Expansions and showed that the expression derived by Lamb [88], Tomotika [164] is true, however the framework of derivation used by Lamb and Tomotika was not entirely correct.

Tomotika *et al.* [164] derived the following model for the normal and longitudinal component of the hydrodynamic force with respect to the symmetry axis of an oblique infinite cylinder. This model is valid for $Re < 4$:

$$C_n = \frac{8\pi}{s}\left(1 - \frac{s^2 - s/2 + 5/16}{32s}\right)Re^2, \tag{4.21a}$$

$$C_l = \frac{8\pi}{2s-1}\left(1 - \frac{2s^2 - 2s + 1}{16(2s-1)}\right)Re^2, \tag{4.21b}$$

where $s = 2.002 - \ln(Re)$.
Through DNS simulations of flow past infinite oblique cylinders, Marhienke and Wegner [109] derived the following models for the force coefficients C_n and C_l which is valid in the range $1 < Re < 20$

$$C_n = 2\exp\left(\sum_{j=0}^{3} p_{n,j}(\ln Re)^j\right) \tag{4.22a}$$

$$C_l = 2\exp\left(\sum_{j=0}^{3} p_{\tau,j}(\ln Re)^j\right) \tag{4.22b}$$

where in equations (4.22a) and (4.22b), $p_{n,j}$ and $p_{\tau,j}$ are four constants shown in tables 4.2 and 4.3.

$p_{n,0}$	1.6911
$p_{n,1}$	-6.722×10^{-1}
$p_{n,2}$	3.3287×10^{-2}
$p_{n,3}$	3.5015×10^{-3}

Table 4.2: Constants used in equation (4.22a)

$p_{\tau,0}$	1.1552
$p_{\tau,1}$	-6.8479×10^{-1}
$p_{\tau,2}$	1.4884×10^{-2}
$p_{\tau,3}$	7.4966×10^{-3}

Table 4.3: Constants used in equation (4.22b)

The model derived by Taylor [163] valid for $Re > 20$ reads as:

$$C_n = \frac{4}{\sqrt{Re}} + 1 \tag{4.23a}$$

$$C_l = \frac{5.4}{\sqrt{Re}} \tag{4.23b}$$

In order to assess the validity and accuracy of these models, numerical simulations of flow past an infinite cylinder at various incidence angles were performed. The numerically obtained C_n and C_l at different Re were compared to the various models described in equations (4.21), (4.22) and (4.23).
Mesh details : The mesh consisted of $\sim 650,000$ tetrahedral elements. The length of the domain downstream from the cylinder was $140d$, where d is the diameter of the cylinder. Periodic boundary conditions were imposed at the top, bottom and lateral sides of the domain. At

the inlet, a velocity boundary condition was specified and at the convective outflow boundary condition was imposed in the outflow side. A portion of the mesh and streamlines of the flow past an oblique cylinder is shown in image 4.7(a). In figure 4.7(b), the streamlines are attached to the surface of the cylinder and there was almost no flow separation at the trailing edge. On increasing the Reynolds number $Re = 60$, the flow detaches at the trailing edge due to the effect of the adverse pressure gradient and this leads to a formation of horseshoe vortex as shown in figure 4.7(c). The Reynolds numbers considered here are in the laminar regime as $Re < 3000$ and one can observe the non linear behavior of the flow at these laminar Reynolds numbers.
Figures 8.4(a) and 8.4(b) show the range of the discussed force models with respect to the Reynolds number.
From figures 8.4(a) and 8.4(b), it is observed that the force models described in this section are in reasonable agreement with the numerical simulations and to the experimental observations [143].

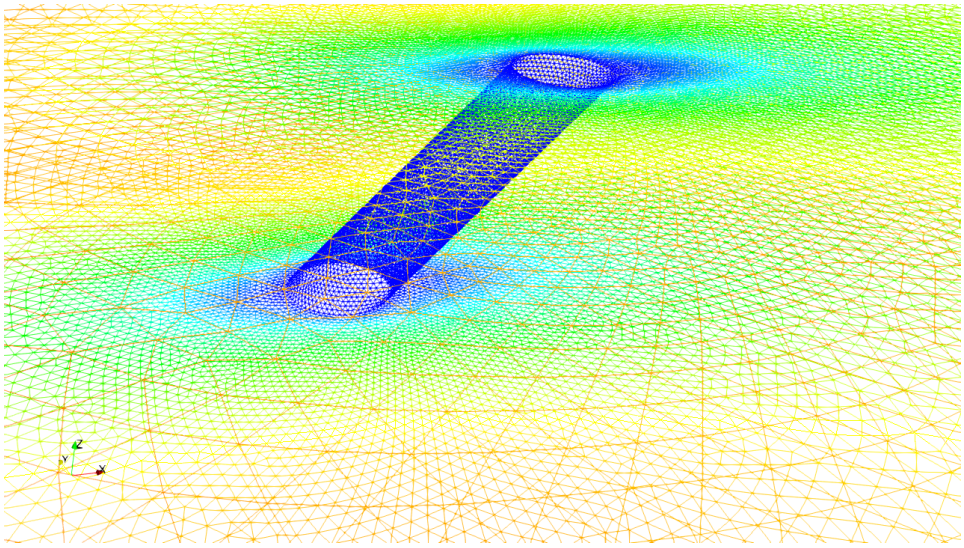

(a) Portion of the mesh for an obliquie infinite cylinder.

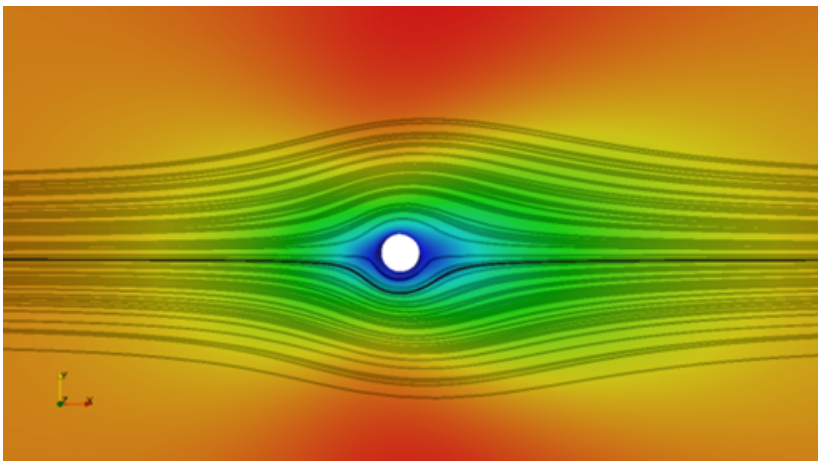

(b) Streamlines at $Re = 0.50$

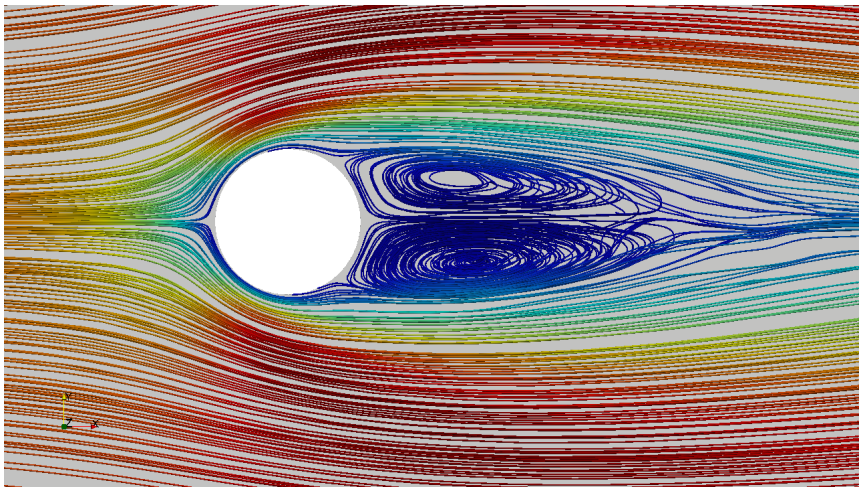

(c) Horseshoe vortex at $Re = 60$

Figure 4.7: Numerical simulations of flow past an oblique infinite cylinder.

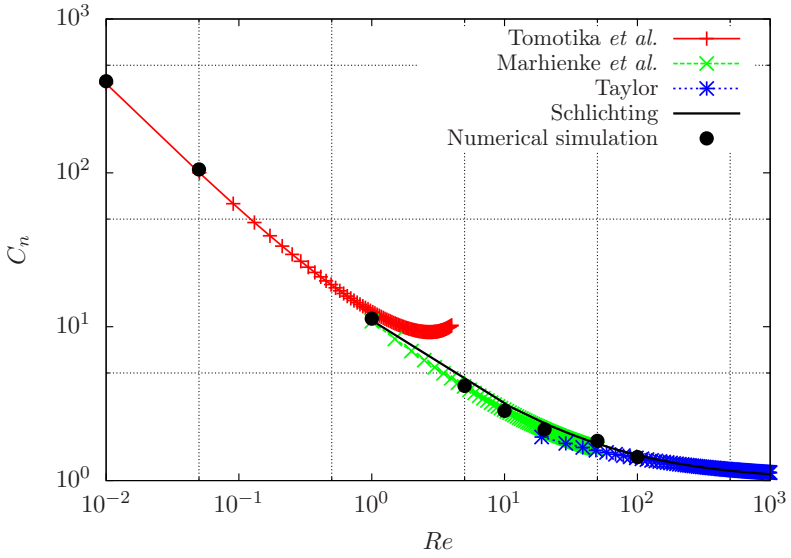

(a) C_n vs. Re

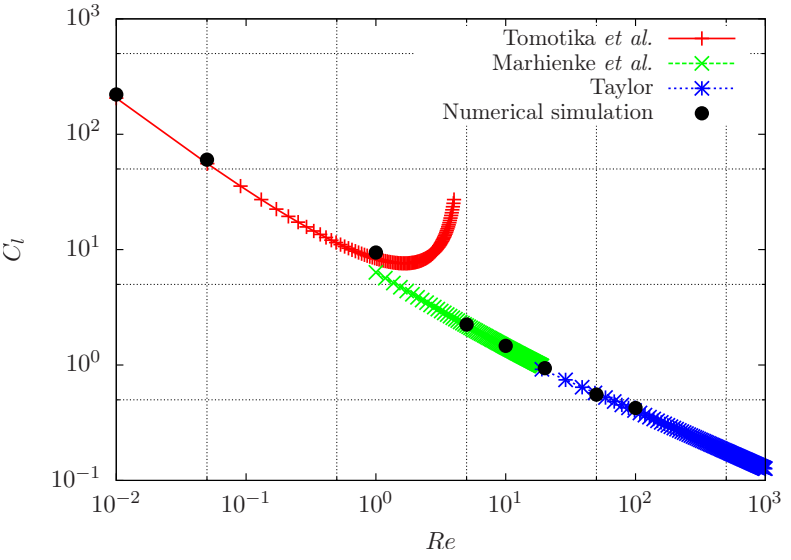

(b) C_l vs. Re

Figure 4.8: Hydrodynamic force coefficients vs. Reynolds Number. In figure 8.4(a), Schlichting refers to the data in ref [143]. Numerical simulations refer to the present study.

4.6 Comparison of different force models.

This section deals with the comparison of the previously discussed hydrodynamic force models (the PS model, slender body theory and infinite cylinder model). These comparisons are done for a situation in which fiber was placed in a uniform flow field. The force per unit length based on each model was calculated.
As defined earlier :

$$C_n = \frac{F_n}{\frac{1}{2}\rho V^2 d_{\text{fib}} l_{\text{fib}}} \tag{4.24}$$

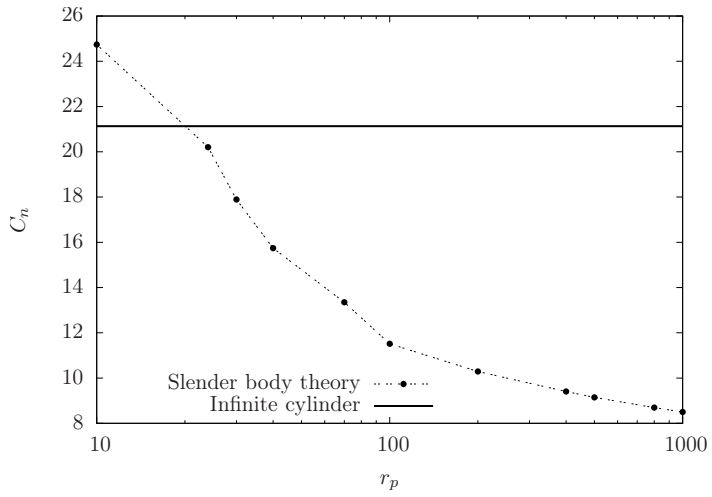

Figure 4.9: Comparison of C_n between the slender body theory and the infinite cylinder

Figure 4.9 shows the dependence of C_n with respect to the aspect ratio r_p of the slender body model. The Reynolds number Re based on the fiber diameter was 0.37. The analytical value of C_n at $Re = 0.37$ was 21.24 (calculated from equations (4.21a) and numerical results obtained from explicit numerical simulations of flow past an infinite cylinder), and the experimental value of C_n at this Reynolds number was found to be 19.6 [168].

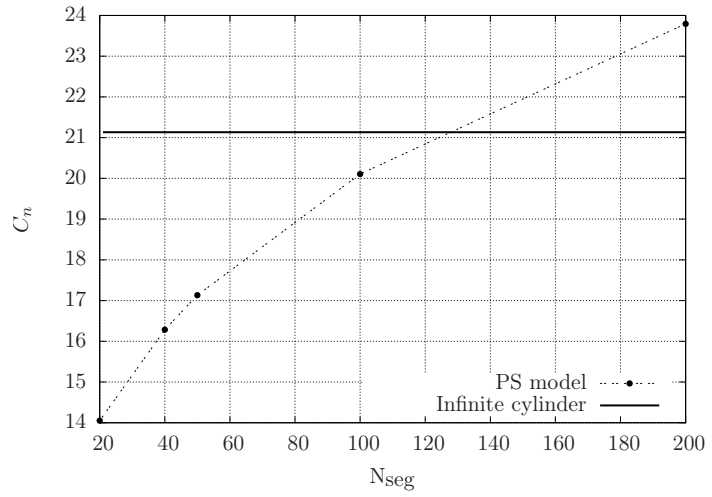

Figure 4.10: Comparison of normal force coefficient C_n between PS model and the infinite cylinder model. $Re = 0.37$, $r_p = 300$

Using the PS model leads to discrepancy in the hydrodynamic force with respect to the number

of fiber segments for a given aspect ratio as shown in figure 4.10. In this simulation, a high aspect ratio fiber $r_p = 300$ was kept fixed, placed in a uniform flow and the Reynolds number based on the fiber diameter was $Re = 0.37$. The normal drag coefficient is then calculated for each configuration with varying number of segments. Figure 4.10 clearly shows the inconsistency of the PS model.
The model derived by Tomotika *et al.* [164] (equation (4.21)) includes a dependency on the Reynolds number and its validity in the creeping flow regime is questionable. The validity of this model at low Reynolds number ($Re < \mathbf{O}(10^{-3})$) was tested by calculating the hydrodynamic torque at the center of the fiber which is placed in a shear flow. The results are compared with solutions of Jeffery [70], slender body theory and explicit numerical simulations. The aspect ratio of the cylinder/fiber in the study was set to $r_p = 128$ and the shear rate was set to $\dot{\gamma} = 0.004$. The flow is in x direction, velocity gradient in y direction and vorticity in z direction as shown in figure 4.2. The hydrodynamic torque at the center ($\vec{T}_o$) of the cylinder using the models (slender body theory and infinite cylinder) are calculated using equation (4.25).

$$\vec{T}_o = \int_{l_f} \vec{O}_c \times \vec{f}_{\text{hyd}} dl \tag{4.25}$$

where $\vec{O}_c$ is the center of the fiber, $\vec{f}_{\text{hyd}}$ the hydrodynamic drag force per unit length. The details of the explicit numerical simulations are presented in section 4.7. Figure 4.11 shows the comparison of the torque between the hydrodynamic force models, Jeffery's theory and numerical simulations. It is observed that the infinite cylinder model of Tomotika *et al.* [164] underestimates the net hydrodynamic torque.

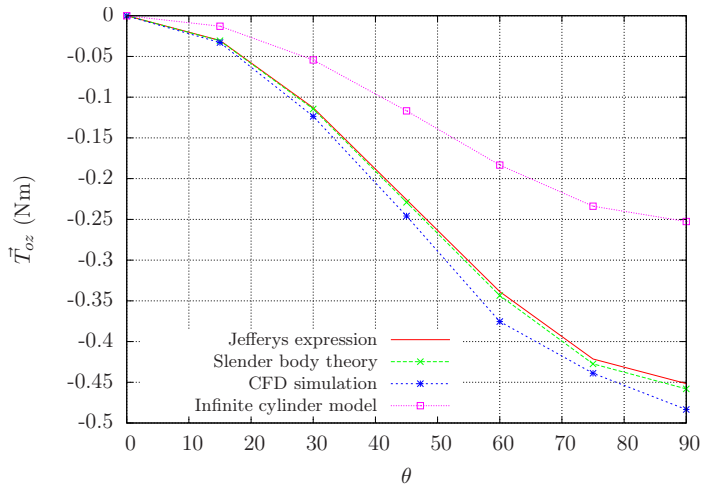

Figure 4.11: $\vec{T}_{oz}$ comparison (Jeffery, slender-body theory, infinite cylinder, $\dot{\gamma} = 0.004$)

A comparison of the local hydrodynamic drag force per unit length on the cylinder/fiber was made. In this comparison, the fiber/cylinder is kept fixed in a shear flow and the symmetric axis is perpendicular to flow direction. We define a Reynolds number Re_{tip}, based on the local velocity $\vec{U}_{x,\text{tip}}$ at the tip of the fibre,

$$Re_{\text{tip}} = \frac{\rho_{\text{fl}} |\vec{U}_{x,\text{tip}}| d_{\text{fib}}}{\mu} \tag{4.26}$$

In the explicit numerical simulations, the mesh of the cylinder was decomposed into several 'ring elements' (see figure 4.13(b)) and the drag force per unit length (f_n) normal to the symmetry axis was calculated on these ring elements. Two Reynolds numbers, $Re_{\text{tip}} = 0.002$ and $Re_{\text{tip}} = 0.02$ were considered. The validity of the slender body theory and infinite cylinder model in terms of

Reynolds numbers is known. Comparing the hydrodynamic force per unit length predicted by these models with numerical simulations give an insight about the validity of these force models in terms of Reynolds numbers.
Figures 4.12(a) and 4.12(b) show the variation of the hydrodynamic force per unit length between the models and the numerical simulations. The aspect ratio r_p in this analysis was set to 128. From figure 4.12, it is seen that the infinite cylinder model of Tomotika *et al.* [164] (equation

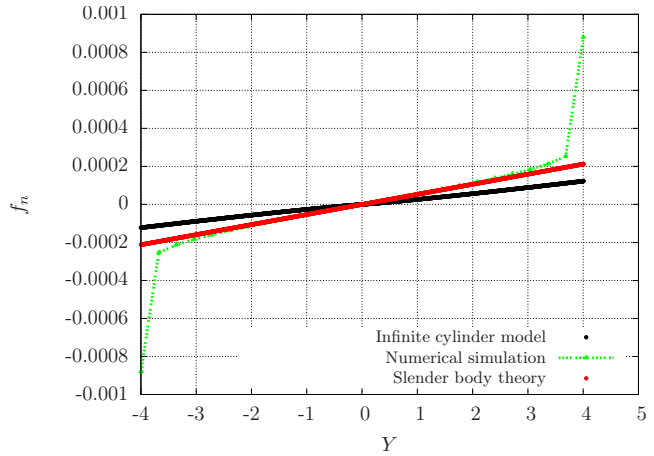

(a) Force per unit length of the cylinder comparison, $Re_{\text{tip}} = 0.002$, $\dot{\gamma} = 0.004\text{s}^{-1}$

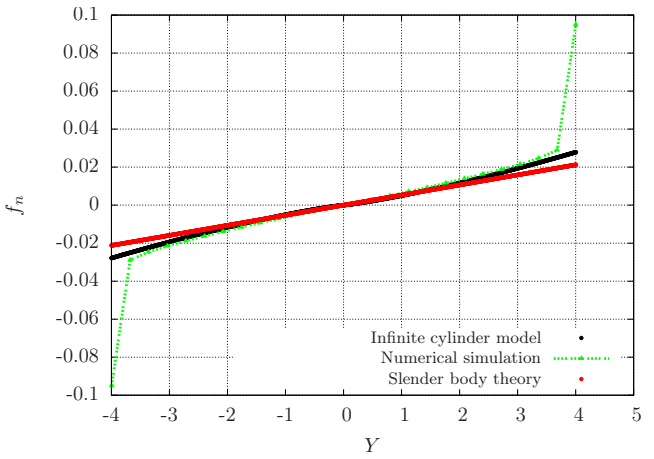

(b) Force per unit length comparison, $Re_{\text{tip}} = 0.02$, $\dot{\gamma} = 0.04\text{s}^{-1}$

Figure 4.12: Comparison of force per unit length for a cylinder in shear flow.

(4.21a)) under predicts the drag force at low Re_{tip} whereas the slender body theory agrees well with the results of the numerical simulations (excluding the tip effects). When the Re_{tip} was increased to 0.02, the drag force per unit length of the infinite cylinder model (equation (4.21a)) showed better agreement with the numerical simulation compared to the slender body theory.
In order to further understand this behavior, explicit 2D numerical simulations for a flow past a circle at various Reynolds numbers (Re based on the diameter) were performed. The C_n values obtained from the numerical simulations and the infinite cylinder model were compared and are shown in table 4.4. It is observed that the infinite cylinder model (4.21a) is not valid for Reynolds numbers less than 10^{-2}.

Re	C_n (model) [164]	C_n (2D simulations)
0.001	2820.2	6210.1
0.0025	1257.6	2384.8
0.005	688.5	1185.2
0.01	380	391.4
0.05	100.6	111.2
0.1	58.6	62.1
0.2	34.2	35.6
0.4	21.7	20.8
0.6	16.25	16.7
0.8	13.2	13.5
1.0	12.2	12.4

Table 4.4: Re vs C_n. The infinite model used here is from Tomotika *et al.* [164], equation (4.21a)

4.7 Hydrodynamic torque model

In the previous section, the hydrodynamic force distribution on the fiber is represented as a line force,when the symmetric axis of the fiber/fiber segment is parallel to the fluid velocity vector, the moment of this hydrodynamic drag force becomes zero as depicted in figure 4.14.
Hence in-order to account for the thickness of the fiber, a hydrodynamic torque model per unit length has been derived in the present study. The present model accounts for the fluid spin and the fluid strain similar to Jeffery's [70] analytical expression. The expression for the torque due to the spin reads as

$$\vec{T_r} = \mu d_f^2 l_{seg} \left(C_{r_\parallel} \vec{p} \otimes \vec{p} + C_{r_\perp} (\mathbf{I} - \vec{p} \otimes \vec{p}) \right) \cdot (\vec{\omega}_f - \vec{\omega}_{seg}) \tag{4.27}$$

where $\vec{\omega}_{seg}$ refers to the angular velocity of the fiber segment and $\vec{\omega}_f$ is the fluid spin ($\vec{\omega}_f = 0.5 \nabla \times \vec{U}_f$). The coefficients $C_{r_\parallel}$ and $C_{r_\perp}$ are hydrodynamic torque resistance that are parallel and normal to the fiber-segment symmetry axis respectively (see figure 4.15)
The expression for the torque due to fluid strain reads as

$$\vec{T_s} = C_s \mu d_f^2 l_{seg} (\boldsymbol{\epsilon} \cdot \vec{p} \otimes \vec{p}) : \mathbf{E} \tag{4.28}$$

where $\mathbf{E}$ is the fluid strain rate tensor, $\boldsymbol{\epsilon}$ is the Levi-Civita symbol. Figure 4.16 depicts the streamlines for a rigid fiber in a straining motion. The values of $C_{r_\perp}$ and C_s were calculated from explicit CFD calculations of a high aspect ratio (r_p) fiber, $r_p = 128$ in a shear flow as shown in figure 4.13(a). A hybrid mesh approach was used as shown in figure 4.13(c), The surface mesh of the fiber is composed of quadrilateral elements (see figure 4.13(b)), and the volume mesh is composed of tetrahedral elements. The size of the fluid domain was set to 8 times the fiber length and the mesh consisted of 1.3×10^6 elements. For deriving the resistance $C_{r_\parallel}$, the domain shown in figure 4.13(d) was used. In this configuration, the cylinder is placed in a rotating wall with periodicity in the axial direction and the hydrodynamic torque at the ring elements are computed.
Figure 4.17 shows the comparison of the net torque $\vec{T}_{oz}$ calculated at the hydrodynamic center of the fiber with the torque predicted by Jeffery's[70] theory for various incidence angles under a shear flow.
The net torque $\vec{T}_{oz}$ at the center of the fiber was calculated using the expression :

$$\vec{T}_{oz} = \int_{S_f} \vec{x}_o \times (\boldsymbol{\sigma}.\vec{n}) ds, \tag{4.29}$$

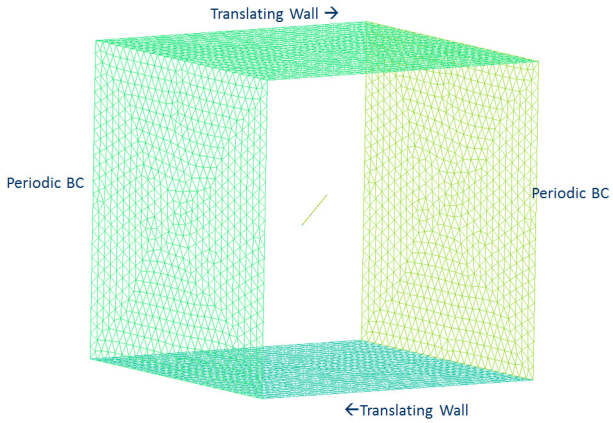

(a) Domain configuration

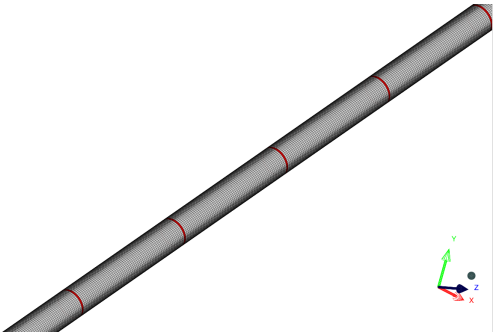

(b) Ring elements (shown in red) over the quad surface mesh

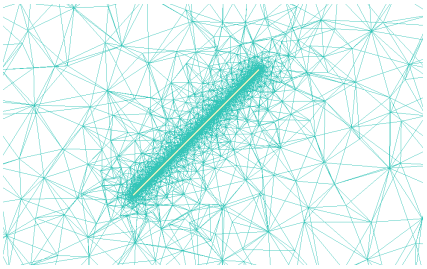

(c) Cut plane view of mesh used for extracting $C_{r_\perp}$

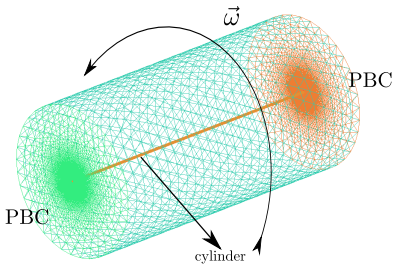

(d) Domain configuration used for extracting $C_{r_\parallel}$

Figure 4.13: Domain and Mesh used for the simulations.

where in equation (4.29), $\vec{T}_{oz}$ is the torque at hydrodynamic center of the fiber, $\vec{x}_o$ refers to the vector from the hydrodynamic center to the surface mesh points on the fiber and $\boldsymbol{\sigma}$ the hydrodynamic stress on the corresponding mesh points.
In order to obtain a "torque per unit length", the torque was calculated on individual 'ring elements' on the surface of the cylinder as shown in figure 4.13(b). The torque on these elements is calculated by the following expression[64]

$$\vec{T}_c = \int_{S_p} \vec{x}_c \times \left(\boldsymbol{\sigma}.\vec{n} - \frac{\vec{F}_{\text{hyd}}}{S_p} \right) ds, \tag{4.30}$$

where in equation (4.30) $\vec{T}_c$ is the torque at the center of the ring element, S_p is the surface area,

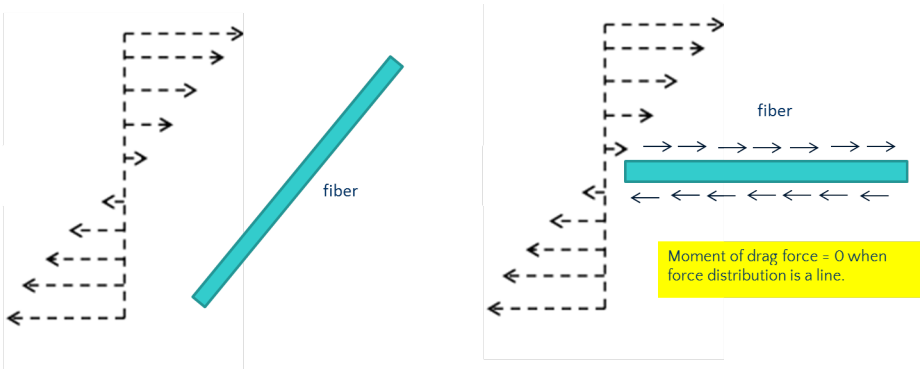

Figure 4.14: Schematic of fiber in shear flow when the symmetry axis is parallel to the fluid velocity. The moment due to the drag force is 0 when the hydrodynamic force distribution is considered as a line.

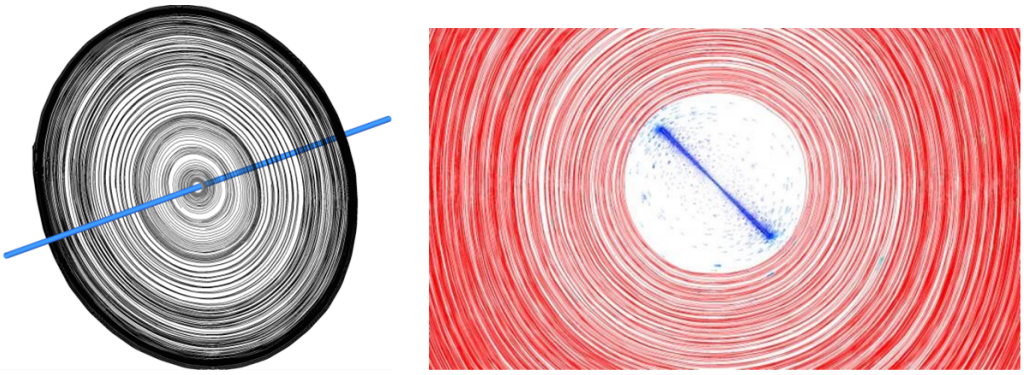

(a) flow stream lines past a rigid fiber/-cylinder with the symmetry axis parallel to fluid vorticity $C_{r_{\parallel}}$

(b) flow stream lines past a rigid fiber/cylinder with the symmetry axis normal to fluid vorticity $C_{r_{\perp}}$

Figure 4.15: Streamlines of flow a rigid fiber in a rotational flow field.

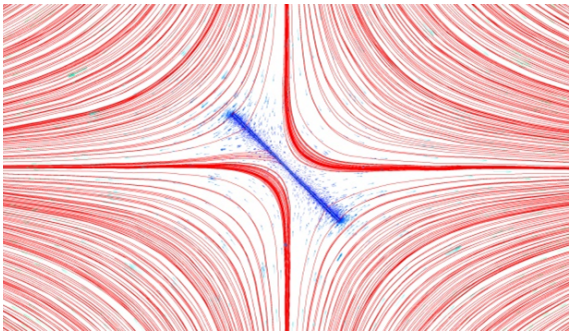

Figure 4.16: Schematic of fiber in straining flow (C_s)

$\boldsymbol{\sigma}$ the hydrodynamic stress, $\vec{F}_{\text{hyd}}$the hydrodynamic force on the ring element and $\vec{x}_c$ is the vector from the center of the ring element to the nodes of the mesh within that particular ring element. Equation (4.30) defines the component of the torque which results only from the shear forces at the fluid/solid interface, removing the torque component resulting from the heterogeneity of the pressure field [64]. This latter component is naturally taken into account in the present model as the moment of the drag force. Figure 4.18 shows the variation of the hydrodynamic torque normalized by the shear rate $\dot{\gamma}$ along the fiber length, calculated at the ring elements by using equation (4.30) for fiber aspect ratio $r_p = 100$ and $r_p = 200$. It was observed that the torque

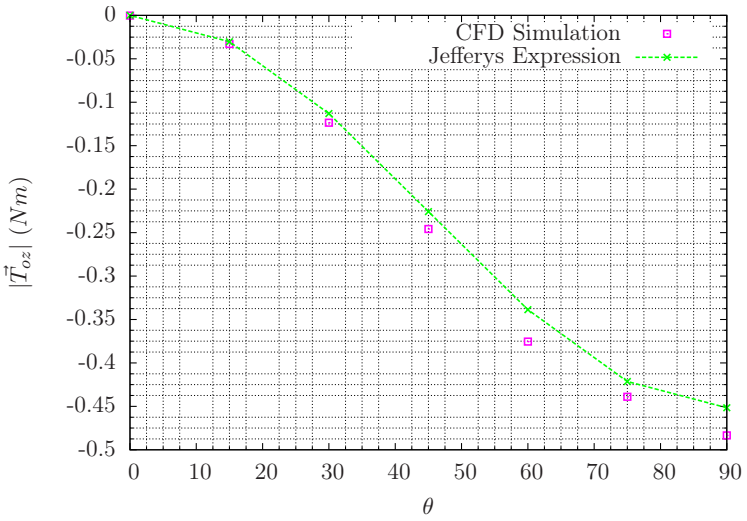

Figure 4.17: Torque comparison with Jeffery's [70] expression, θ is the angle between the fiber axis and flow direction. Equation (4.29) was used to calculate $\vec{T}_{oz}$.

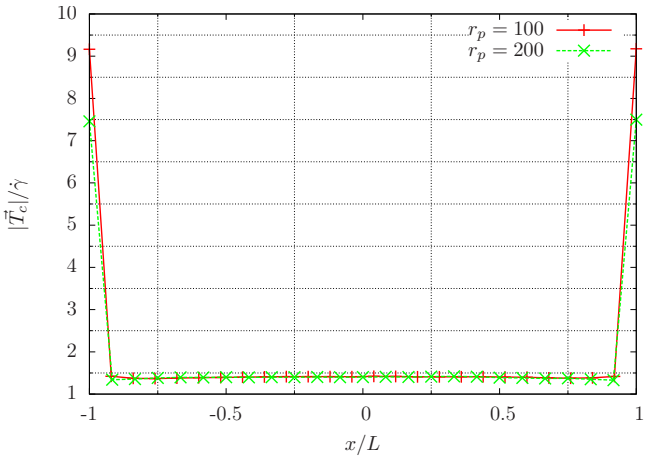

Figure 4.18: Variation of the hydrodynamic torque (normalized by the shear-rate $\dot{\gamma}$) on the ring elements along the length of the cylinder for aspect ratios r_p 100 and 200.

was independent of the aspect ratio on all the ring elements, except at the tips of the fiber. Figure 4.19 shows the obtained values of C_r and C_s for different orientations of the cylinder in a shear flow. Based on these results, the values of $C_{r_\parallel}$,$C_{r_\perp}$ and C_s were set to 3.10, 0.35 and 3.07 respectively. An analytical expression for the component $\vec{T}_{r_\parallel}$ per unit length has been derived in refs [89, 130] their expression reads as

$$\vec{T}_{r_\parallel} = \pi d^2 \mu \vec{\omega}_f \cdot dl \tag{4.31}$$

Comparing the coefficient in (4.31), the numerically obtained value of $C_{r_\parallel}$ is in good agreement. The developed torque model is based on the creeping flow formulation (Jeffery's equations [70]). The use of such a torque model is justified due to the following reasons:

- The hydrodynamic force should explicitly lead to the hydrodynamic torque (difference in forces along the fiber segments should generate a torque).
- The rotational Reynolds number (equation (4.32)) is proportional to the square of the fiber

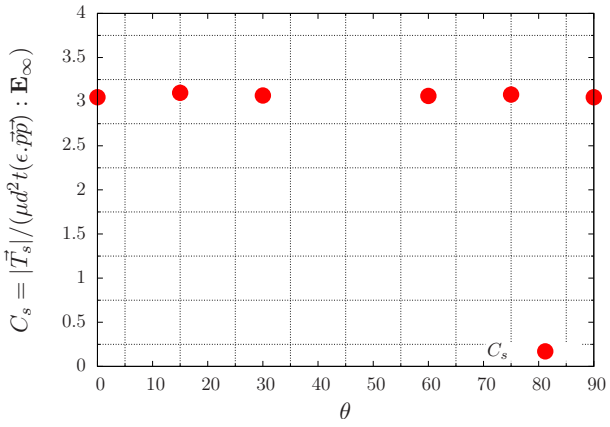

(a) C_s

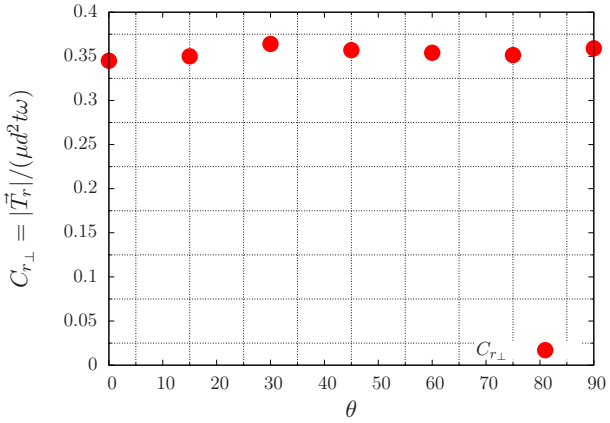

(b) $C_{r_\perp}$

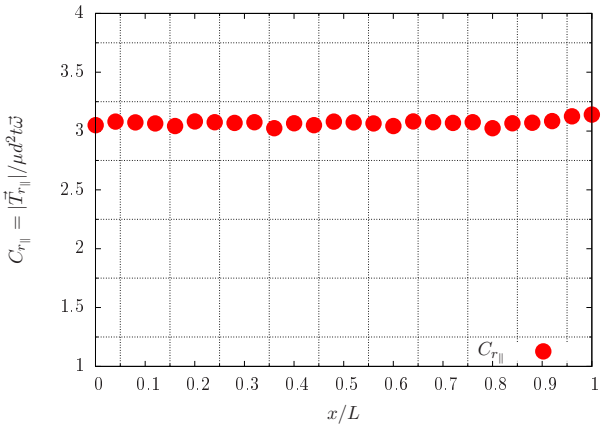

(c) $C_{r_\parallel}$

Figure 4.19: C_s and C_r for different angles θ between the fiber axis and flow direction. At $\theta = 45^o$ the fiber axis is parallel to the principal axis of the strain rate tensor, hence the torque $\vec{T}_s$ due to the fluid strain is 0.

diameter and for small diameters ($\approx 10^{-6}\mu$m), a Stokesian model would suffice.

$$Re_{\text{rot}} = \frac{|\vec{\omega}|_{\text{rel}}\, d_{\text{fib}}^2}{\nu} \tag{4.32}$$

4.8 Conclusion

An examination of various hydrodynamic force and torque models have been presented. The prolate spheroid model used in previous studies has been implemented and tested and the results were in good agreement with Jeffery's theory. In addition in the case of flexible fibers, the deformed shapes were compared with experimental results. However, the prolate spheroid model shows a strong dependency on the fiber discretization and this model is not valid for small finite Reynolds numbers. The slender body theory is valid for very low Reynolds numbers $Re < 10^{-2}$ but at higher Reynolds number the slender body theory under predicts the drag force. Furthermore, the drag force predicted by the slender body theory is dependent on the aspect ratio of the fiber and as the aspect ratio is increased, the drag force tends to 0 which is a major shortcoming. The infinite cylinder model of Tomotika *et al.* was found to be valid for $Re > 10^{-2}$ and for lower Reynolds numbers, this model under predicts the drag force. A model which describes the hydrodynamic torque 'per unit length' was developed from explicit simulations of a high aspect ratio fiber in a shear flow.
In the following chapters several examples of the simulation results using the infinite cylinder model and the developed hydrodynamic torque model are presented. The hydrodynamic force formulation of the slender body theory is used for high aspect ratio rigid fibers in creeping flow for $Re < 10^{-2}$ and the infinite cylinder model is used for all types of fibers at finite Reynolds numbers.

CHAPTER 5

VALIDATION TEST CASES

Contents

5.1 Introduction

The present chapter deals with some validation test cases for the coupled numerical model. Three test cases are considered in the present work. In the first test case, the deflection of the free end of a fiber placed in an uniform flow is considered for several Reynolds numbers. These results are compared with the experimental results of Tritton [168] and an analytical solution for the deflection. In the second test case, the deformation of flexible fibers under a homogeneous isotropic turbulent flow field is studied. The probability density function of the end-to-end vector is obtained numerically and the results are compared with the experimental results of Brouzet *et al.* [28]. Under the same framework, the correlation of the tangent vector along the length of the fiber for different fiber lengths is studied and these results are compared with the experimental study of Verhille and Bartoli [172]. In the last test case, the flow of a fiber suspension in a channel is considered. Two Reynolds numbers viz. $Re = 2000$ and $Re = 6000$ are studied and the effect of the fibers on the mean flow field are studied. The fiber concentration in this study is fixed at 1% concentration by volume and the results of this last study are compared with the experimental results of Xu and Aidun [182].

5.2 Deflection of a free end fiber in a uniform flow

5.2.1 Experiment

Tritton [168] performed experiments to study the drag of cylinders in low Reynolds number flow ($Re = \rho U d_f/\mu$ varying from $0.387 - 100$). In the experiments, a high aspect ratio (r_p varying from 500 to 876) quartz fiber cemented on one end was placed in an uniform flow and the deflection of the free end was measured using a traveling microscope. As a first validation case, the experiments of Tritton were numerically performed for various Reynolds numbers as shown in Table 5.1.
An analytical expression for the deflection h of the fiber based on the simple bending moment theory, was derived as [168] :

$$h = \frac{8Fl_f^4}{\pi E d_f^4} \tag{5.1}$$

where in equation (5.1), F is the force per unit length, E the fiber Young's modulus. In the present study, comparisons between the experimental, analytical and the simulations were made. The expression of hydrodynamic force per unit length on an infinite cylinder derived by Tomotika *et al.* [164] was used for the analytical solution (equation (5.1)).

5.2.2 Numerical study

Figure 5.1 shows the schematics of the numerical simulations, it consisted of a fiber fixed on one end, i.e. the translational and rotational degrees of freedom of the node attached to the wall was blocked. In order to obtain uniform velocity profile and since the dimensions of the wind-tunnel were unknown, periodic boundary conditions were applied at the top and bottom surfaces. The domain was discretized into $64 \times 64 \times 2$ cells, properties of the fluid correspond to air $\rho_f = 1.205$ kg/m^3 and $\mu = 1.81 \times 10^{-5}$ Pa s. The fiber properties are given in Table 5.1.

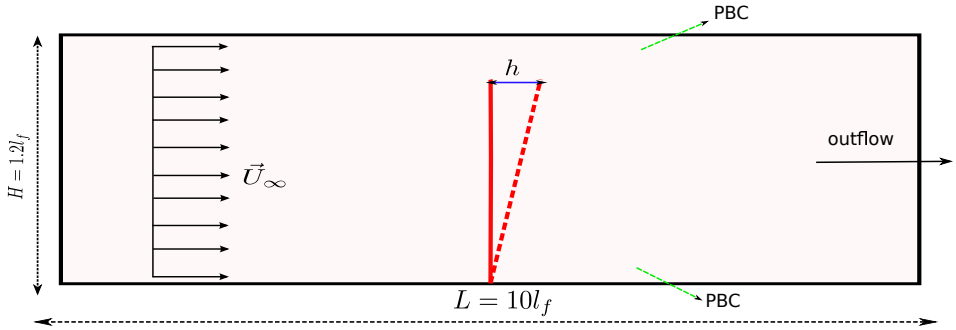

Figure 5.1: Schematics of the numerical setup, $\vec{U}_\infty$ is the fluid velocity, l_f is the fiber length, PBC refers to Periodic Boundary conditions for the fluid domain, the bottom node of the fiber is fixed, h is the deflection.

Fiber Type	E (GPa)	d_f (cm)	l_f (cm)	Reynolds numbers
Fiber-1	79.4	0.00194	1.70	$0.387 - 0.845$
Fiber-2	79.0	0.00197	1.27	1.16
Fiber-7	59.5	0.00745	1.12	49
Fiber-8	59.5	0.01125	2.11	105

Table 5.1: Fiber properties and Reynolds numbers used in the validation study.

The prolate-spheroid model (PS) and the infinite cylinder model (current model) were used in the numerical study and the deflections obtained from these models were compared. In the case of PS model, the diameter of the equivalent spheroid was determined based on the semi-empirical expression derived by Cox [41]. This expression was previously used by Lindström and Uesaka [97]. The expression for the equivalent diameter of the spheroid reads as

$$d_{\text{spheroid}} = \frac{1}{1.24} d_f \left(\ln \frac{l_{\text{seg}}}{d_f} \right)^{1/2} \tag{5.2}$$

The expressions of the hydrodynamic force on a prolate-spheroid presented by Kim and Karrila [80] were used. The simulations were run until a steady state convergence of the deflection was obtained. Figure 5.2(a) shows the time convergence of the infinite cylinder model (current model) with respect to the fluid grid. One can observe that deflections of the fiber converge for different fluid discretizations.

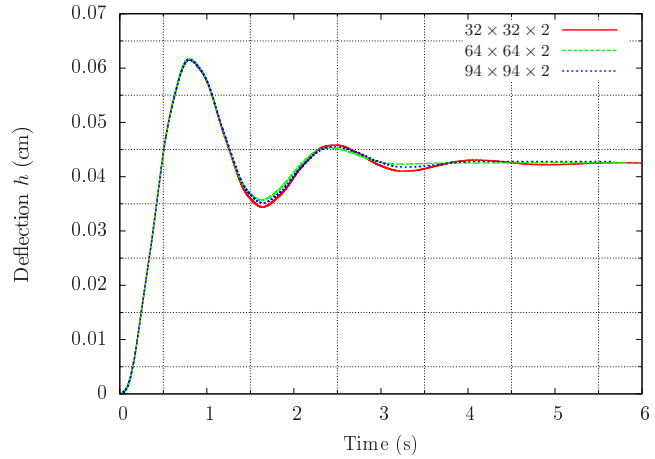

(a) Grid convergence study for the infinite cylinder model.

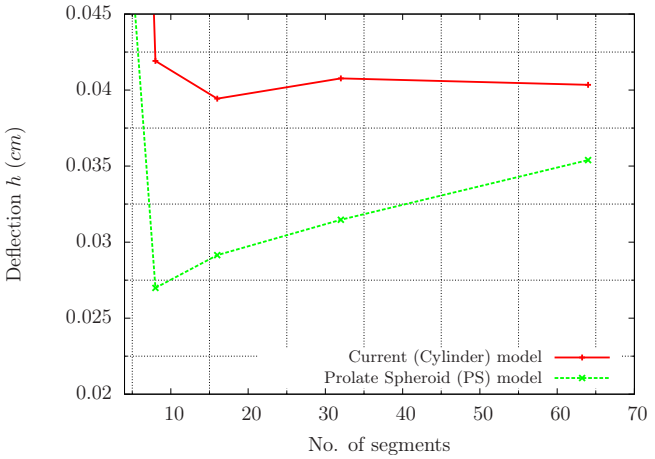

(b) Comparison of model sensitivity with respect to the number of segments used for the fiber discretization.

Figure 5.2: Grid and segment convergence studies for the deflection h of fiber placed in a uniform flow at $Re = 0.387$.

Figure 5.2(b) shows the convergence of deflection for the two force models with respect to number of segments for Fiber-1. It is observed that using the PS model leads to a dependence on the segment discretization. This error/difference is due the geometric parameter called eccentricity (based on the segment aspect ratio) which varies with the number of segments resulting in a different net drag force as discussed in Chapter 4. Figure 8.6 shows the comparison of the

obtained deflection with respect to the experimental values for different Reynolds numbers. The maximum error in the case of current force model was found to be approximately 7%, whereas for the PS model, the error was approximately 43% with 55 segments as shown in figure 8.6. Figures 5.4(a) and 5.4(b) shows the convergence of deflection of Fiber-1 and Fiber-8 at $Re = 1$

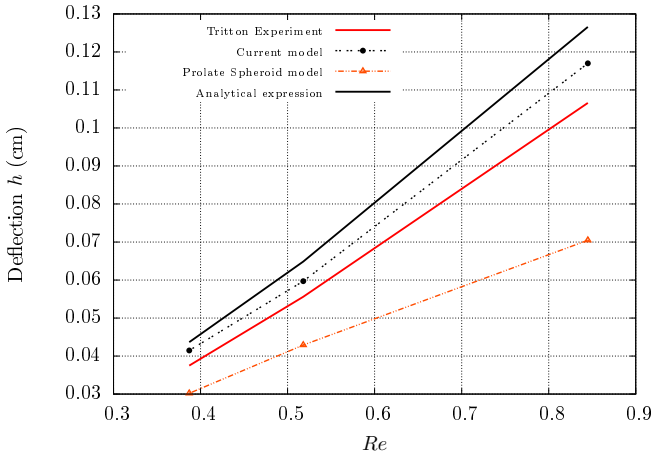

Figure 5.3: Comparison of deflection h with experimental and numerical results (PS and current model) and the analytical expression.

and $Re = 105$ respectively. The mesh in these computations consisted of $64 \times 64 \times 2$ and the fibers were discretized into 64 segments. Table 5.2 shows the comparison of the deflection h between experiments h_{exp}, simulations h_{sim} and the analytical expression (equation (5.1)) $h_{\text{analytical}}$.

Type	Reynolds number	h_{sim}(cm)	h_{exp} (cm)	$h_{\text{analytical}}$ (cm)
Fiber-1	0.387	0.0426	0.0413	0.0436
Fiber-1	0.518	0.0605	0.0556	0.0640
Fiber-1	0.845	0.1180	0.1063	0.126
Fiber-2	1.16	0.0471	0.0460	0.0508
Fiber-7	49.0	0.0142	0.0138	0.0154
Fiber-8	105	0.0904	0.0878	0.0980

Table 5.2: Comparison of deflection h between experiments, simulations and analytical expression (5.1) for all fiber types. h_{sim} is obtained using the infinite cylinder model discussed in chapter 4.

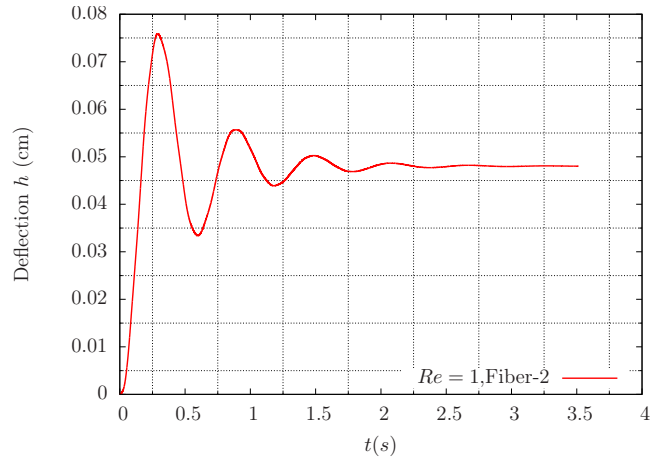

(a) Deflection convergence at $Re = 1.16$

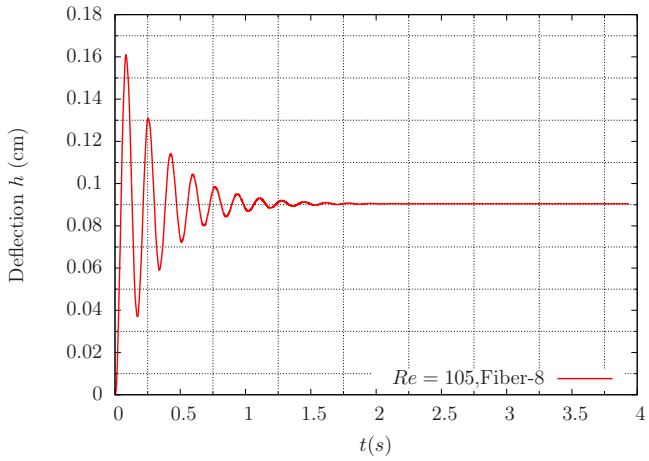

(b) Deflection convergence at $Re = 105$

Figure 5.4: Deflection convergence

5.3 Flexible fiber in turbulent flow

5.3.1 Experiment

The dynamics of flexible fibers in isotropic turbulent flow was studied experimentally by Brouzet *et al.* [28] and Verhille and Bartoli [172]. In both studies, an isotropic Von Kármán flow was generated in a cylindrical tank by counter rotating disks. The Reynolds number was calculated based on the rotational frequency and the disk radius, i.e $Re = 2\pi R^2 f/\nu$, where f is the disk rotation frequency, R the disk radius and ν the kinematic viscosity of the fluid. The disks were placed 17.6 cm apart in a cylindrical container, with each disk having a diameter of 17.2 cm [28, 172]. A schematic diagram of the experimental setup is shown in figure 5.5

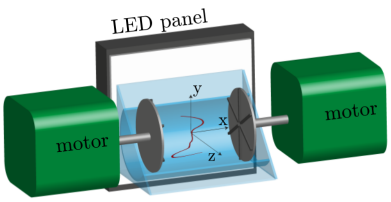

Figure 5.5: Schematics of the experimental setup used in experiments [28, 172]

In the study of Brouzet *et al.* [28], the working fluid used was a mixture of water and ucon oil with a dynamic viscosity of $\mu \sim 100 \times 10^{-3}$ Pa s, whereas in the experimental study of Verhille and Bartoli [172], the working fluid was water. Brouzet *et al.* [28] studied the conformation and distortion of fibers in an isotropic turbulent flow field. The integral scale Reynolds number was varied by changing the rotational frequency f of the disk (f varies from 2Hz to 30Hz, $Re_L \approx 1000$ to 10^4) and the authors obtained the Probability Density Function (PDF) of the end-to-end vector $\vec{Z}_e$ for different fiber lengths. From the experimental study, it was observed that the behavior of a flexible fiber under a turbulent flow field is "analogous to a polymer in a good solvent" [28], i,e. a fiber behaves as a macroscopic polymer [28]. The deformation of the fiber was dependent on the turbulent dissipation rate ϵ and the length of the fiber l_f. However, for high aspect ratio fibers or for a certain length greater than the "persistence length" l_p, the fibers were always flexible. Verhille and Bartoli [172] obtained the correlation of the tangent vector along the length of the fiber for l_f ranging from $l_f = 1$ cm to $l_f = 5$ cm. In their study the Reynolds number Re_L and turbulent dissipation rate ϵ were 6.8×10^5 and 6 m^2/s^3, respectively, and the fiber's Young's modulus was $\sim$ 400 kPa. The expression for the elastic length l_e (the term "elastic length" was used instead of persistence length by Verhille and Bartoli [172]) defined by Verhille and Bartoli [172] reads as

$$l_e = \frac{(EI)^{1/4}}{(\rho\mu\epsilon)^{1/8}}, \tag{5.3}$$

where E is the Young's modulus of the fiber, I the moment of inertia of the fiber cross section ($I = \pi d_f^4/64$), ϵ the turbulence dissipation rate, ρ and μ the density and viscosity of the fluid respectively.

5.3.2 Numerical study

In In the present work, numerical simulations of flexible fibers in homogeneous isotropic turbulent (HIT) flows were performed. The correlation of the unit tangent vector along the fiber length $\langle \vec{p}(s)\vec{p}(s+l)\rangle$ and PDF of the fiber end to end vector $\vec{Z}_e$ were compared. DNS simulations of HIT flow field in physical space at $Re_{\lambda_m} \approx 50 - 90$, based on the Taylor micro-scale λ_m were performed. This range of Re_{λ_m} leads to integral scale Reynolds numbers Re_L comparable to the experiments of Brouzet *et al.* [28] In order to sustain the turbulence at the prescribed Reynolds number (Re_{λ_m}), the linear forcing scheme for physical space proposed by Rosales and Meneveau [137] was used.
The initial conditions of the flow field (single phase fluid) corresponding to $Re_{\lambda_m} = 78.6$ are shown in table 5.3

Re_{λ_m}	Reynolds number based on Taylor micro scale	78.6
N^3	Number of grid points	256^3
ν	Kinematic viscosity	1.1×10^{-4} m^2/s
K	Kinetic energy	2.24 m^2/s^2
ϵ	Dissipation rate	48.4 m^2/s^3
λ_m	Taylor micro scale	7×10^{-3}m
η_k	Kolmogorov length scale	4×10^{-4}m
l_t	Length scale of largest eddy	0.036m
τ_ϵ	Eddy turnover time	4.519×10^{-2} s
$\Delta x/\eta_k$	Grid resolution	2.23
L_D	Domain length	0.23 m

Table 5.3: Initial conditions for the present HIT simulations at $Re_{\lambda_m} = 78$. For other values of Re_{λ_m}, the turbulent kinetic energy K was changed.

In Table 5.3, ϵ is the average dissipation rate per unit mass and η_k the Kolmogorov scale, the length scale of the smallest eddies at which the fluid viscosity dominates and the turbulent kinetic energy K is dissipated into heat. For homogeneous isotropic turbulence η_k and ϵ are related as

$$\eta_k = \left(\frac{\nu^3}{\epsilon}\right)^{\frac{1}{4}}. \tag{5.4}$$

the turbulent kinetic energy K is defined based on the root mean square of velocity fluctuations u'

$$K = \frac{3}{2}u'^2. \tag{5.5}$$

The Taylor micro-scale λ_m is an intermediate length scale used to characterize turbulence, is defined as

$$\lambda_m = \sqrt{10}\eta_k^{2/3} l_t^{1/3}. \tag{5.6}$$

The Reynolds number Re_{λ_m} based on λ_m, is defined as

$$Re_{\lambda_m} = \frac{u'\lambda_m}{\nu}. \tag{5.7}$$

The length scale of the largest eddies or the integral length scale l_t, is defined as

$$l_t = \frac{u'^3}{\epsilon}. \tag{5.8}$$

The eddy turnover time τ_ϵ is defined as

$$\tau_\epsilon = \frac{K}{\epsilon}. \tag{5.9}$$

Simulation of the fibers in HIT flow field were performed once a statistical stationary state of

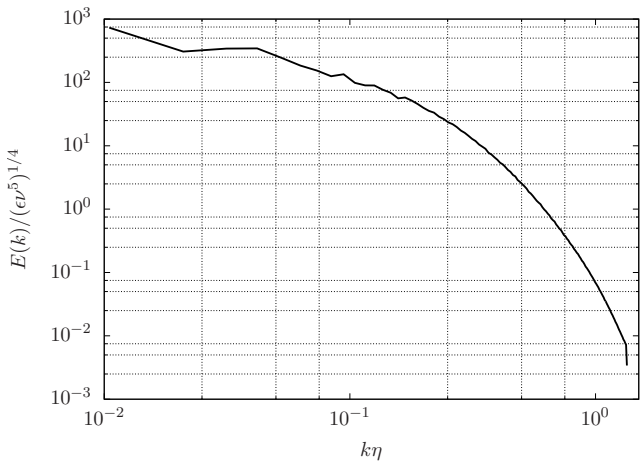

Figure 5.6: Normalized kinetic energy spectrum at the statistically stationary state corresponding to $Re_{\lambda_m} = 78.6$. The wave numbers k was normalized using the Kolmogorov scale length η_k.

the flow field was obtained. Figure 5.6 shows the obtained energy spectrum at this state. The number of fibers in the simulation was 50 and the number of segments used in the simulation for different fiber lengths is given in Table 5.4. The diameter of the fibers were set to the value in the experimental studies [28, 172], $d_f = 620\,\mu$m. Comparing to the experiments of Brouzet *et al.* [28], the fiber and the fluid properties were the same, however the Reynolds number based

Fiber length l_f (cm)	Number of segments n_{seg}
1	8
2	24
3	36
5	44
16	80

Table 5.4: Fiber discretization for different fiber lengths

on the Taylor micro-scale is comparatively lower in the simulations ($Re_{\lambda_m} \approx 80$ to 3000 in the experiments). Comparing the numerical setup with the experiments of Verhille and Bartoli [172], the fluid properties and fiber properties were different but the elastic length l_e was kept similar by changing the Young's modulus. The contact interaction between the fiber segments were not considered in the present simulations as the experiments correspond to dilute concentration.

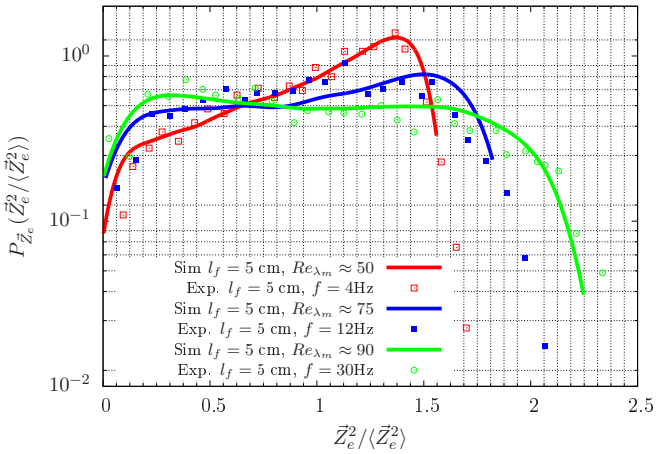

(a) PDF of $\vec{Z}_e^2$ for $l_f = 5$ cm

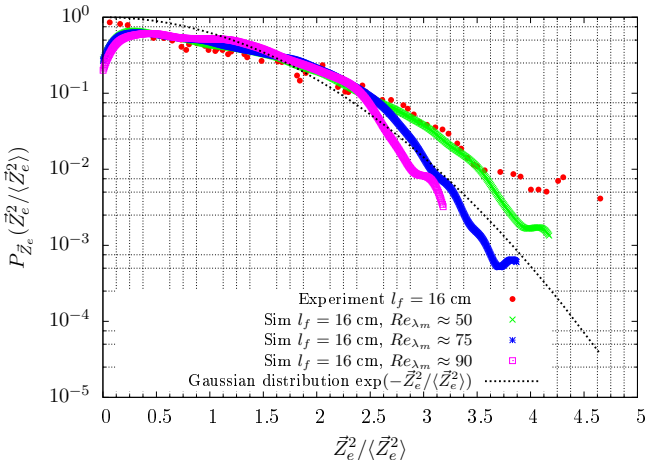

(b) PDF of $\vec{Z}_e^2$ for $l_f = 16$ cm, the rotational frequency in the experiment is unavailable.

Figure 5.7: PDF comparison for different fiber lengths between present simulations and experiments of Brouzet *et al.* [28]

Figures 5.7(a) and 5.7(b) show the PDF comparison of the end to end vector $\vec{Z}_e$ with the experimental results of Brouzet *et al.* [28]. Figure 5.8 shows the deformation of flexible fibers in a turbulent flow. In the case of $l_f = 5$ cm, the shape of the PDF changed indicating a transition from a rigid fiber towards a flexible fiber as a function of the input turbulent kinetic

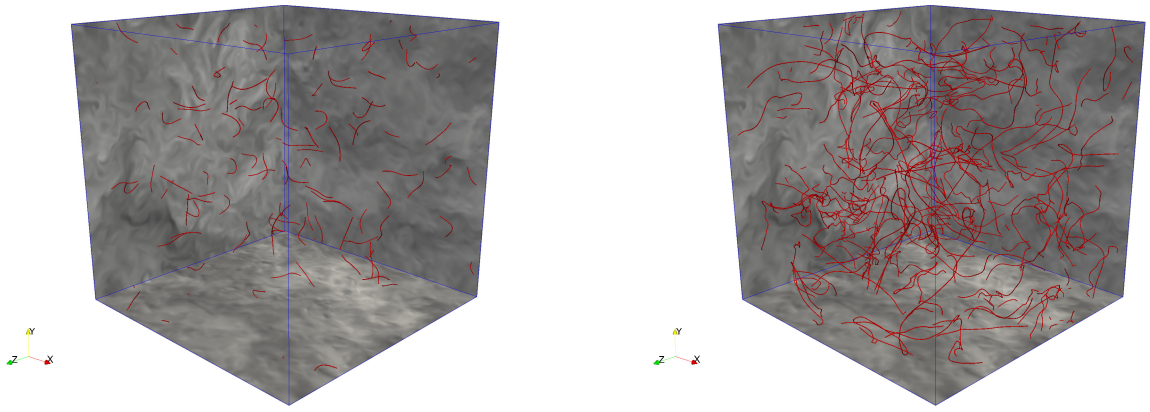

(a) $l_f = 5\,\text{cm}$ (b) $l_f = 16\,\text{cm}$

Figure 5.8: Instantaneous deformation of fibers in HIT flow field at $Re_{\lambda_m} = 78$. (fibers colored in red and fluid velocity contours in grayscale.)

energy, indicating that the numerical results are consistent with the experimental observations. While in the case of the longer fiber $l_f = 16\,\text{cm}$, the fibers remained flexible for all Re_{λ_m}, which was characterized by a behavior similar to the Gaussian distribution of $\vec{Z}_e^2/\langle\vec{Z}_e^2\rangle$, ($G(\vec{Z}_e^2) \sim \exp(-\vec{Z}_e^2/\langle\vec{Z}_e^2\rangle)$) consistent with the experimental observation and the fiber flexibility increases with increasing Re_{λ_m}. Figure 5.9 shows the particle Reynolds number based on the slip velocity between the fiber segments and fluid velocity. From the figure it is inferred that the segment Reynolds numbers are mostly in the inertial regime.

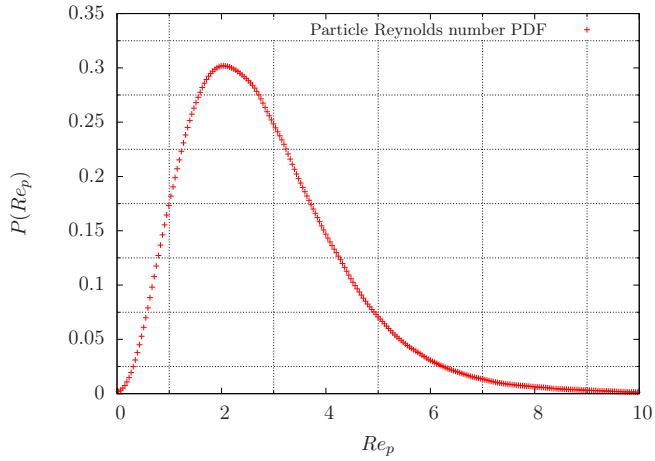

Figure 5.9: PDF of segment Reynolds number based on slip velocity in HIT flow field at $Re_{\lambda_m} = 52.4$.

Finally, the experimental results of the correlation function of the tangent vector [172] $\vec{p}(s)$ were compared with the results of the simulations. Since the working fluid in the experiments and the numerical simulation are different and in order to maintain the same elastic length l_e, and owing to higher dissipation rate in the simulations, the Young's modulus of the fibers in the simulations were set to $E = 1.5\,\text{GPa}$. Figure 5.10 shows the comparison of the correlation functions of the tangent vector along the fiber length. For low ratios of l/l_e the numerically obtained correlation function agrees well with the experimental ones. However, for higher l/l_e ratios,there is a consistent deviation between the numerically obtained correlation function and experimental ones, this might be due to the difference in the properties of fiber and fluid between

the experiments and the simulations. Moreover, the quantity elastic length l_e may not be a universal parameter to compare with, as the bending of fibers are greatly influenced by the length scale of the interacting eddies.

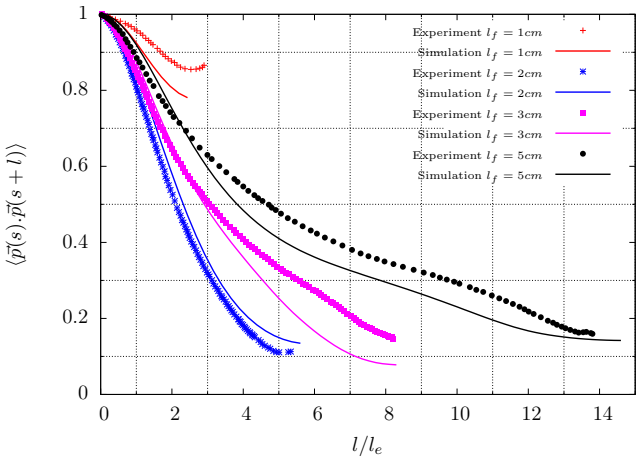

Figure 5.10: Correlation of the tangent vector along the fiber length comparison between the present study and experiments of Verhille and Bartoli [172]. Here l is the distance from one end of the fiber and l_e is the elastic length calculated by equation (5.3).

5.4 Concentrated fiber suspension in channel flow

5.4.1 Experiment

Xu and Aidun [182] performed an experimental study of wood fiber suspensions in a channel flow for varying concentrations and Reynolds number (Re varying from 2000 to 92000, based on the bulk fluid velocity and half the channel height). Their experiment consisted of a rectangular plexiglass channel with the dimensions of 150 cm in length, 5.08 cm in width and 1.65 cm in height. The velocity profiles for suspensions with concentrations varying from 0.0% to 1.0% were measured by the technique of Pulsed Ultrasonic Doppler Velocimetry (PUDV). In addition to the measurement of velocity profiles, the fluctuations in the velocity fields were also measured.

5.4.2 Numerical study

In the present study, we performed DNS simulations of 1% concentration fiber suspension for Reynolds numbers of 2000 and 6000 (Re based on the bulk fluid velocity and half the channel height). The dimensions of the channel used were 6.5δ in the stream-wise direction x, 2δ in the wall normal direction y and and 2.2δ in the lateral direction z, where $\delta = 0.0024$ m.

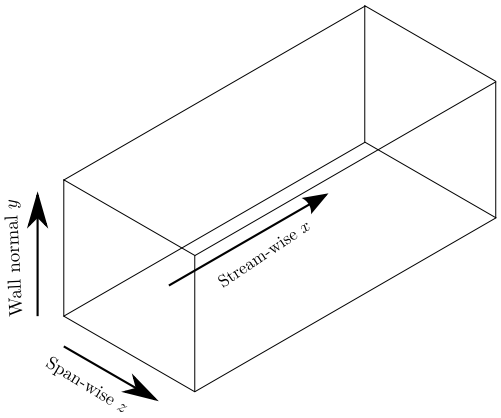

Figure 5.11: Schematics of the channel flow simulation.

The Reynolds number is defined based on the fluid bulk velocity and half the channel height:

$$Re_{\text{flow}} = \frac{\rho_{\text{fl}} U_{\text{b}} \delta}{\mu}, \tag{5.10}$$

where U_{b} is the fluid bulk velocity. The turbulent Reynolds number Re_τ is based on the friction velocity u_τ. The friction velocity is defined as

$$u_\tau = \sqrt{\frac{\tau_w}{\rho_{\text{fl}}}}. \tag{5.11}$$

For setting up the initial conditions and mesh spacing, the wall shear stress τ_w was calculated using the skin friction factor based on the Reynolds number Re calculated using the following expression [143]:

$$C_f = \frac{0.026}{Re^{1/7}}, \tag{5.12a}$$

and the wall shear stress:

$$\tau_w = \frac{C_f \rho_{\text{fl}} U_{\text{b}}^2}{2}. \tag{5.12b}$$

y^+ is defined as the non-dimensional distance from the wall. It is calculated using the following expression:

$$y_i^+ = \frac{\rho_{\text{fl}} u_\tau y_i}{\mu}. \tag{5.12c}$$

In equation (5.12c), y_i is the distance in the wall-normal direction. u_τ was initially calculated using equations (5.12b) and (5.11)
The channel domain was discretized into $128 \times 164 \times 128$ mesh points in the x, y and z respectively, with the first grid point placed at the viscous sublayer in 0.05 wall units ($y^+ = 0.05$). Periodic boundary conditions were employed in the x and z directions and no slip wall boundary condition in the y direction. Figure 5.11 shows the schematic of the numerical setup. DNS simulations similar to those of Morinishi *et al.* [115] were performed. The corresponding Reynolds number based on the friction velocity u_τ was $Re_\tau = 360$.

Figure 5.12 shows the comparison between the DNS results of the present study and the previous study of Moser *et al.* [116]. [3]
In figure 5.12(a), u^+ is the nondimensional velocity, obtained by normalizing the fluid velocity with u_τ. The turbulence statistics were obtained by performing temporal and spatial average over vertical planes for each y^+ and this procedure was done for 8 flow through times after the

[3] The RMS components of velocity was not available in the DNS database, http://turbulence.ices.utexas.edu/data/MKM/chan395/

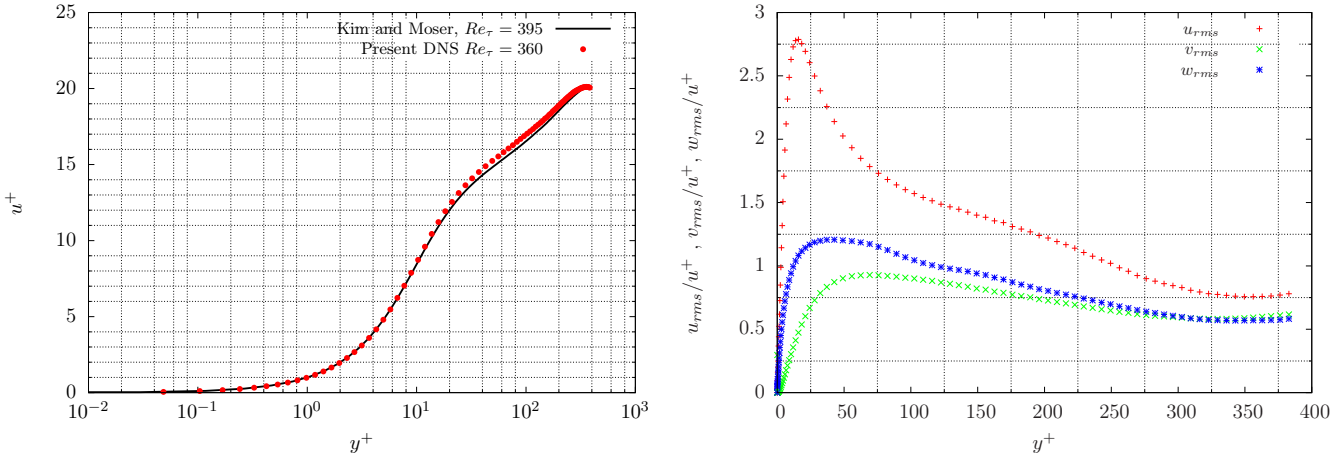

(a) Comparison of velocity profile in wall units between present study and ref [116] at $Re = 6000$.

(b) Root mean square components at $Re = 6000$, single phase flow.

Figure 5.12: Comparison of single phase flow DNS results.

flow was established. The friction velocity u_τ was calculated based on the numerically obtained wall shear stress τ_w. Figure 5.12(b) shows the root mean square(RMS)/fluctuating components of the fluid. The RMS components were obtained by subtracting the mean flow velocity from the instantaneous velocity field. The RMS components give an indication of the turbulence intensity and from the figure, it is observed that the turbulence production occurs near the wall in the viscous sublayer at $y^+ < 5$. Similar profiles are obtained in other DNS studies [115, 116].
Numerical simulations were performed with the fiber suspension at 1% concentration. The Young's modulus of the fiber corresponds to pulp fiber properties with $E = 21mmGPa$. The geometrical properties (aspect ratio $r_p = 60$ ($d_f = 38\mu$m, $l_f = 2.3mm$) similar to the experiments were used. Each fiber was discretized into 30 segments and a total of 1280 fibers (corresponding to 1% concentration) were initialized with random orientations and positions. The fluid properties are that of water (similar to the experiments), $\rho = 1000\,\mathrm{kg/m^3}$, $\mu = 0.001\,\mathrm{Pa\,s}$. The velocity field obtained from the DNS of single phase was flow used as the initial condition.
Figure 5.13 shows the comparison of the velocity profile for $Re = 2000$ with the experimental results [182]. Compared to the laminar flow velocity profile, the velocity profile of the fiber suspension resembles more of a turbulent flow rather than a laminar flow, as shown in figure 5.14(a). In fact there was a transition from the laminar flow to turbulent flow. Such a transitional effect was characterized in the DNS study of spherical particles (5% concentration by volume) in a channel flow by Loisel *et al.* [101] who reported similar effects in the production of near wall turbulent intensity as shown in figure 5.14(b).

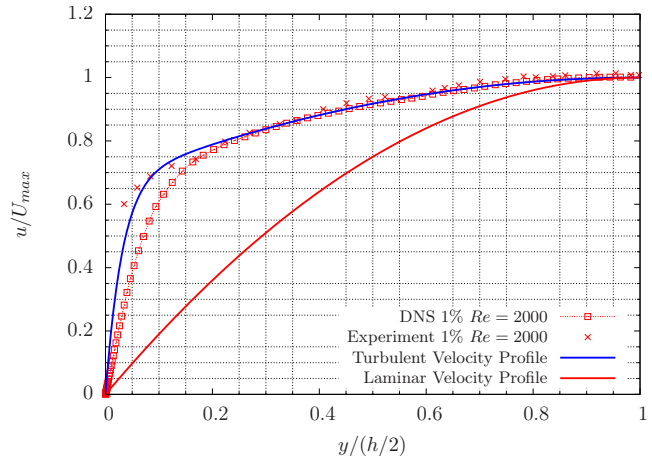

Figure 5.13: Comparison of velocity profiles between single phase fluid and 1% fiber suspension at $Re = 2000$.

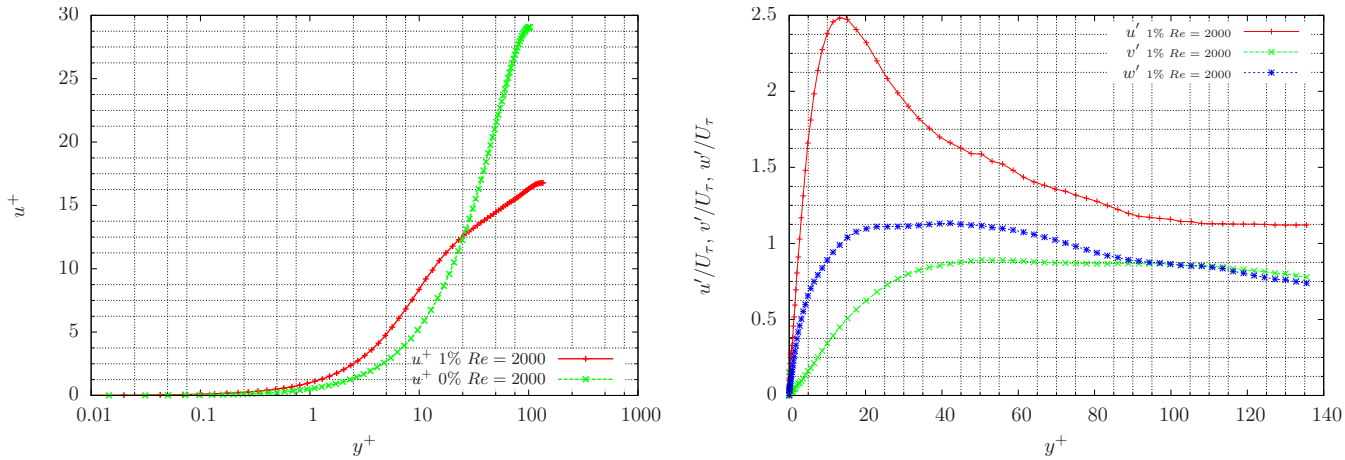

(a) Comparison of velocity profile in wall units between single phase fluid and fiber suspension at $Re = 2000$.

(b) Comparison of root mean square components at $Re = 2000$.

Figure 5.14: Non dimensional velocity profiles, $Re = 2000$.

Figure 8.8 shows the comparison of the velocity profile for $Re = 6000$ with the experimental results of Xu and Aidun [182]. The fiber suspension flow was characterized by a blunt velocity profile similar to a plug flow behavior. This effect is seen clearly in figure 5.16(a) where a reduction in velocity is observed in the region $y^+ > 100$. Such a reduction in the velocity, indicates that a significant portion of the mean turbulent kinetic energy is being transferred between the phases and further studies are required to understand and quantify this phenomenon. A reduction in the turbulence intensity in the stream wise direction, similar to the experimental results [182] and numerical results of Do-Quang [47] *et al.* is observed. The presence of fibers tends to dampen the turbulence. However, figure 5.16(b) shows that the fluctuating components (RMS) of wall-normal v' and spanwise w' directions were slightly higher ($\sim 2-3\%$) than the RMS components of the single phase turbulent flows in the regions of $y^+ > 175$ as the fibers tend to introduce certain instabilities in the log layer and outer layer of the flow. Figure 5.17 shows the PDF of the fiber segments Reynolds number based on the slip velocity, one can observe that the average segment Reynolds number were in the magnitude of 10.

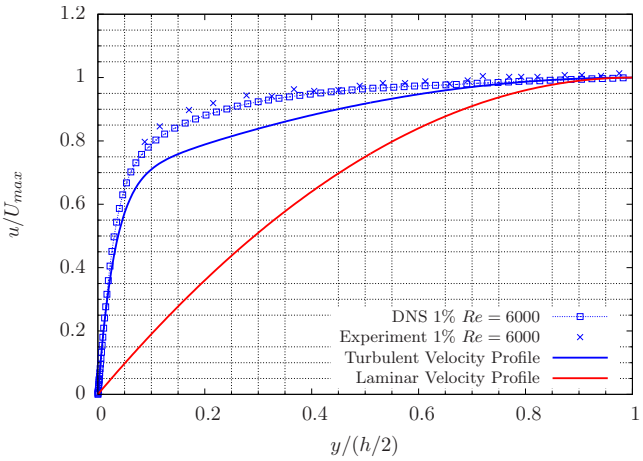

Figure 5.15: Comparison of velocity profiles between single phase fluid and 1% fiber suspension at $Re = 6000$.

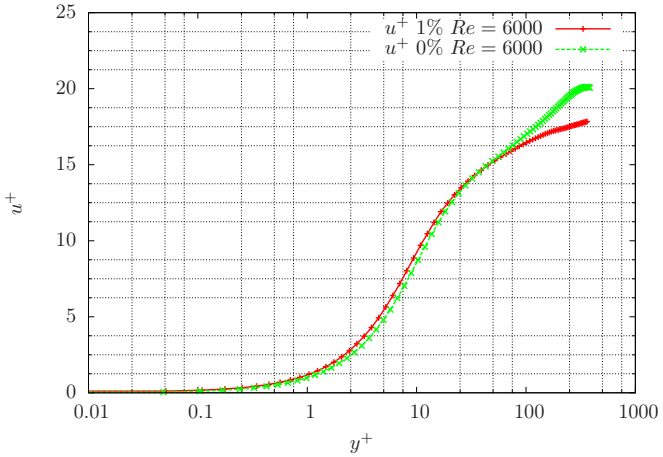

(a) Comparison of velocity profile in wall units between single phase fluid and fiber suspension at $Re = 6000$.

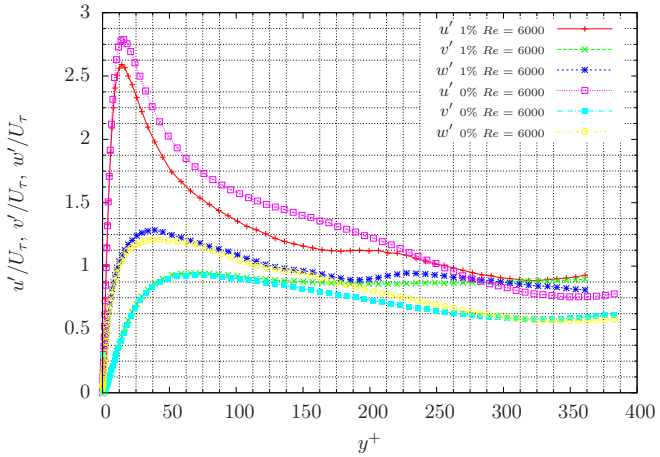

(b) Comparison of RMS components.

Figure 5.16: Non dimensional velocity profiles at $Re = 6000$.

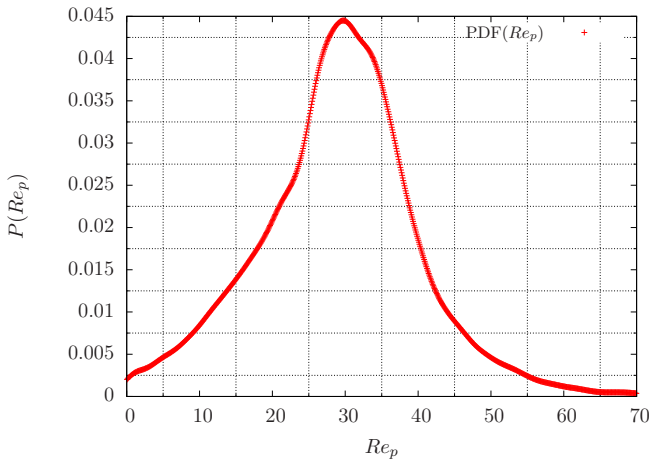

Figure 5.17: PDF of segment Reynolds number based on the slip velocity in turbulent channel flow. The Re based on half the channel height, $Re = 6000$

Figure 5.18 shows the evolution of the fiber structure in the turbulent channel flow case for different flow through times. As the steady state was approached, a plug-like flow structure was observed with several fibers accumulating at the wall and a core with flocs in the center of the channel.

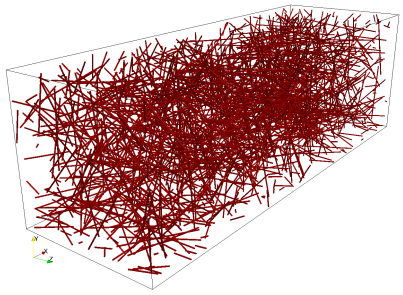

(a) $t/T = 0$

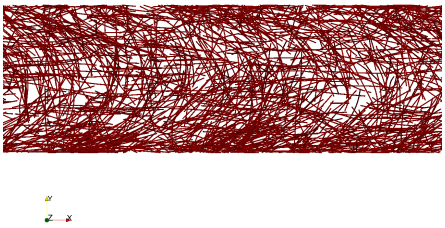

(b) $t/T = 1$

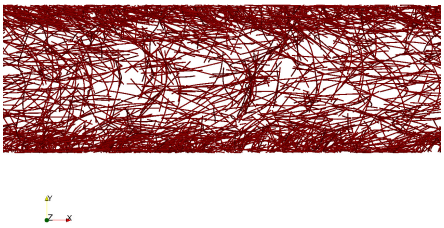

(c) $t/T = 2$

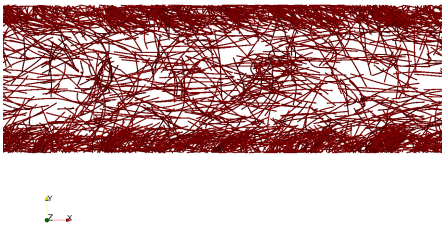

(d) $t/T = 3$

Figure 5.18: Evolution of floc formation for various flow through times, figures 5.18(b) to 5.18(d) sliced $X - Y$ plane.

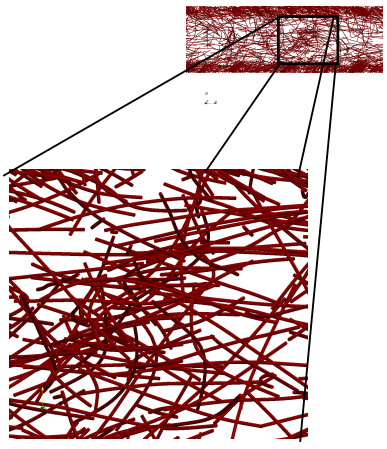

Figure 5.19: Magnified view of floc.

5.5 Conclusion

The developed numerical model was used to describe the deformation of flexible fibers under various flow conditions for low and high Reynolds numbers with reasonable agreement to the experiments. Furthermore, the present model was able to characterize some important flow physics of fiber suspensions such as the damping of turbulence and formation of fiber flocs under a channel flow.

CHAPTER 6

SEMI DILUTE RIGID FIBER SUSPENSIONS IN SHEAR

Contents

6.1 Introduction

Based on the concentration of the suspended fibers in the suspension, three distinct regimes i.e. : dilute, semi-dilute and concentrated regimes can be identified. In this chapter monodisperse fiber suspensions with the fibers having length l_f, diameter d_f and aspect ratio r_p are considered. The orientation vector of a fiber is represented by $\vec{p}$ and the number density (number of fibers per unit volume) of the fiber suspension is denoted by n.
In dilute suspensions, both the hydrodynamic and contact interactions between the fibers are minimal. The motion of the fibers in such a suspension under a low Reynolds number simple shear flow, follow Jeffery's prediction, that is they would rotate about their center of mass following the Jeffery orbits [70]. In such suspensions, the fibers tend to align or spend most of the time (depending on the fiber aspect ratio r_p and the shear rate $\dot{\gamma}$ the time spent would be in the order of $r_p/\dot{\gamma}$) in the $x-z$ plane (figure 2.1) and they quickly rotate (in the order of inverse of the shear rate $\dot{\gamma}$). For such suspensions, Batchelor [13] derived the following expression for the stress of the suspension:

$$\boldsymbol{\sigma_f} = \mu_{\text{fiber}} \left(\langle \vec{p} \otimes \vec{p} \otimes \vec{p} \otimes \vec{p} \rangle - \frac{1}{3} \boldsymbol{\delta} \langle \vec{p} \otimes \vec{p} \rangle \right) : \boldsymbol{E} + 2\mu \boldsymbol{E}, \tag{6.1}$$

where, μ_{fiber} is a constant depending on the concentration and aspect ratio of the fibers. The angled brackets denote the ensemble average over the orientation distribution of the fibers, $\boldsymbol{E}$ is the fluid strain rate tensor and μ the fluid dynamic viscosity. For dilute suspensions, the expression for μ_{fiber} reads as [13]

$$\mu_{\text{fiber}} = \frac{\pi n l_f^3 \mu}{6 \ln (2 r_p)} f(\epsilon), \tag{6.2a}$$

where $\epsilon = (\ln(2r_p))^{-1}$, and $f(\epsilon)$ is defined as

$$f(\epsilon) = \frac{1 + 0.64\epsilon}{1 - 1.5\epsilon} + 1.659\epsilon^2. \tag{6.2b}$$

On increasing the concentration (semi-dilute and concentrated regime) of the fibers, the evolution of the microstructure cannot be predicted using Jeffery's theory. In such suspensions, inter fiber interactions tend to dominate the evolution of the microstructure. These fiber-fiber interactions are in the form of contact forces, short range hydrodynamic forces (lubrication effects) and long range hydrodynamic interactions (effect of the disturbance in fluid velocity field). In the semi-dilute regime, Shaqfeh and Fredrickson [146] showed that the dilute theory of Batchelor [13] was found to be applicable using the following correction to μ_{fiber}:

$$\mu_{\text{fiber}} = \frac{\pi n l_f^3 \mu}{3\left(\ln(1/c) + \ln(\ln(1/c)) + A\right)}, \tag{6.3}$$

where, c is the volume fraction of fibers, A is a constant depending on the fiber orientation. The parameter $A = -0.66$ for a suspension with random fiber orientation [160] and $A = 0.16$ when all the fibers are aligned in the same direction.
Based on the microstructure of the fiber suspension and equation (6.1) the following rheological properties for dilute and semi-dilute suspensions can be obtained, written as follows:

The relative viscosity μ_{rel} of the fiber suspension was derived as

$$\mu_{\text{rel}} = 1 + \frac{\mu_{\text{fiber}}}{\mu}\langle p_x^2 p_y^2 \rangle. \tag{6.4a}$$

The first normal stress difference N_1 is

$$N_1 = \sigma_{xx} - \sigma_{yy} = \mu_{\text{fiber}}\dot{\gamma}\left(\langle p_x^3 p_z\rangle - \langle p_x p_y^3\rangle\right), \tag{6.4b}$$

and the second normal stress difference N_2 is

$$N_2 = \sigma_{yy} - \sigma_{zz} = \mu_{\text{fiber}}\dot{\gamma}\left(\langle p_x^3 p_z\rangle - \langle p_x p_y p_z^2\rangle\right). \tag{6.4c}$$

Various experimental studies have dealt with the rheological behavior of rigid fiber suspensions. Bibbo [16, 15] studied the rheological behavior of non-colloidal rigid fiber suspensions using a parallel-plate rheometry device. The effect of fiber concentration on the apparent viscosity was studied for dilute and semi-dilute regimes. The results were compared to Batchelor's theory [13] and good agreement was seen in the dilute regime. The presence of other fibers in the near vicinity do not allow the individual fibers to follow the Jeffery's orbits. In this regime, the fiber-fiber interactions tend to dictate the microstructure and rheological properties of the suspension. Stover *et al.* [160] experimentally studied the microstructural behavior of semi-dilute rigid fiber suspensions. Their experiment was based on optical methods. It allowed for the direct observation of tracer fibers in a couette rheometry device. The statistics of the orientation of the fibers were obtained from the images of the microstructure. Analysis of the data was performed in order to characterize the orbit distribution of the fibers. Using the orientation distribution and Batchelor's theory [13] (equations (6.1) to (6.4c)) the rheological properties of the fiber suspension was deduced. The measured orbit constants agreed well with the experimental results of Anczurowski, *et al.* [4] for the dilute regime. The rheological properties of the suspension compared reasonably well to the experimental results of Bibbo [15] and to the theory proposed by Shaqfeh and Fredrickson [146] (equations (6.18) to (6.4c)). The hydrodynamic interactions between fibers in the semi-dilute regime play a major role in the steady state orientation of the suspension. Within this context, Rahnama *et al.* [134] derived the steady state fiber orientation using the framework of perturbation analysis along with the theory of Leal and Hinch [91] for weak rotary brownian motion. The results of the orbit distribution, fiber orientation distribution

compared reasonably with the experimental results of Stover *et al.* for the semi dilute regime. However the steady state fiber orientation distribution did not agree well with the experimental results of Anczurowski *et al.* [3] for semi-dilute suspensions. Rahnama *et al.* argued that the fiber orientation distribution observed by Anczurowski *et al.* were not entirely due to inter-fiber hydrodynamic interactions but could also be due to thermal convection in the fluid. The rheological properties of high aspect ratio rigid fibers in the semi-dilute and semi-concnetrated regime in a parallel plate rheometry device was measured by Petrich *et al.* [129]. In the experimental study, the height of the parallel plate geometry was 3 times the fiber length and the effective viscosity of the suspension and the difference between the first and second normal stress differences were measured. The experimental study of Petrich was mainly confined to high aspect ratio fiber suspension ($r_p = 52$, $r_p = 72$) in the semi-dilute regime and the semi-concentrated regime. The experimental results were in reasonable agreement with theory of Shaqfeh and Fredrickson for $r_p = 52$ in the semi dilute regime.

Several particle-based numerical approaches have been used to study the rheological behavior of dilute and semi-dilute fiber suspensions. Based on a modified method of Stokesian Dynamics for ellipsoids and spheroids, Claeys and Brady [37, 38] studied the microstructural and rheological behavior of semi dilute rigid fiber suspensions, the hydrodynamic interactions between the fibers were resolved based on the multipole expansion arising from the formulation of SD. Lindström and Uesaka [99, 100] performed two way coupled simulations of semi dilute suspensions and their results were in good agreement with previous experimental studies. However as shown previously in Chapter 4, their simulations are highly sensitive to the number of segments as the hydrodynamic force description is based on approximating the fiber segment as a prolate spheroid. Salahuddin *et al.* [141] used the LBM-EBF model used to study the rotational diffusivity of semi dilute fiber suspensions in shear. The numerically obtained rotational diffusion were compared with the theoretical results of Koch's diffusion model [82] and to the experimental results of Stover *et al.* [160]. Sundararajakumar and Koch [161] developed a numerical method to study suspensions involving mechanical contacts between the fibers. The method did not include fiber-fiber hydrodynamic interactions (both lubrication and long range effects) and could not accurately describe the behavior of semi-dilute suspensions.

Recently Snook *et al.* [156] studied the normal stress differences in concentrated non-Brownian rigid fiber suspensions. The effect of confinement on the normal stress differences were aslo studied numerically in ref. [157]. In the work of Snook *et al.* [156], the normal stress differences were obtained both numerically and experimentally and it was observed that for short aspect ratio fibers ($10 < r_p < 20$), the sign of the second normal stress difference was negative was approximately half the value of first normal stress difference. In the experimental works of Bounoua *et al.* [17], similar phenomena was observed qualitatively and the effect of confinment was studied. In their study it was found that increasing the confinement led to an increased second normal stress difference (with a negative sign). A review on the rheology of fiber suspensions have been presented recently by Butler and Snook [31].

In this chapter numerical studies on semi dilute suspensions of rigid non-Brownian fibers in shear are presented. The rheological properties of the fiber suspensions were obtained via direct calculations and comparisons with previous theoretical and experimental studies are presented. Semi-dilute suspensions of fibers with aspect rations viz. $r_p = 18$, 32 and 52 were performed for concentrations varying from $c_v = 0.0075$ to 0.035 (maximum $nl_f^3 = 52$). The methodology in this study is similar to the previous chapter but owing to extremely low Reynolds numbers at the fiber scale, the slender body theory of Batchelor [12] is used to describe the hydrodynamic force on the fiber segments. The purpose of this chapter is to serve as a validation of the developed model at low Reynolds numbers and to demonstrate its ability to predict the rheological behavior of fiber suspensions in which the rheological and microstructure behavior is dominated by the long range short range fiber-fiber hydrodynamic interactions. The numerically obtained results are compared with the various experimental results and to the the semi dilute theory derived by

Batchelor [13] and Shaqfeh and Fredrickson [146].

6.2 Numerical Setup

6.2.1 Hydrodynamic force model

The hydrodynamic force model in this study is based on the slender body theory (presented in Chapter 4). As presented in Chapter 4, the solutions of the flow past an infinite cylinder in low Reynolds number flows underpredict the hydrodynamic force. However for long and finite axisymmetric bodies, the slender body theory accurately describes the hydrodynamic force. This hydrodynamic force is derived in 'per unit length' fashion and is logarithmically dependent on the aspect ratio r_p of the particle. For a cylinder with aspect ratio $r_p > 10$, the following equations describe the hydrodynamic force:

$$\vec{f}_{\parallel} = \frac{2\pi\mu}{\ln(2r_p) + C_0}\left(\vec{U}_{f_{\parallel}} - \vec{U}_{\text{seg}_{\parallel}}\right), \tag{6.5a}$$

$$\vec{f}_{\perp} = \frac{4\pi\mu}{\ln(2r_p) + C_0}\left(\vec{U}_{f_{\perp}} - \vec{U}_{\text{seg}_{\perp}}\right), \tag{6.5b}$$

where in equations (6.5a) and (6.5b), r_p is the fiber aspect ratio, $\vec{f}_{\parallel}$ is the component of hydrodynamic force parallel to the symmetry axis of the fiber segment, and $\vec{f}_{\perp}$ is the component of the hydrodynamic force normal to the symmetry axis. In addition C_0 is a constant defined as : $C_0 = \ln(2.0) - 1.5$ [23].

6.2.2 Simulation setup

The setup of the numerical simulation consists of fibers suspended in a Couette flow. Periodic boundary conditions are applied in the X and Z directions and translating wall boundary conditions are applied in the Y directions as shown in figure 6.1(a). The edge length of the fluid elements in the domain was equal to the length of a fiber segment, as such a discretization would allow to capture fluid disturbances and its effect on the other fiber segments to be captured. The initial microstructure is composed of fibers having random orientations and positions (figure 6.1(b)). The critical Young's modulus at which a fiber would undergo deformation in a shear flow is [58]

$$E_{\text{crit}} = \frac{2\mu\dot{\gamma}r_p^4}{\ln(2r_p) - 1.75}. \tag{6.6}$$

where in equation (6.6), $\dot{\gamma}$ is the shear rate. Therefore in the present study, the Young's modulus of the fibers were set to 10 times of E_{crit}. Table 6.1 gives the parameters of the present numerical study. The parameter r_p is the fiber aspect ratio, l_f the length, d_f the diameter and E_y is the Young modulus of the fiber. N_f is the number of fibers present in each concentration and n_{seg} is the number of the segments by which the fibers are discretized. c_v is the volume fraction of the fibers. nl_f^3 and $nl_f^2 d_f$ are the fiber concentration based on the number density $n = N_f/V$ with V the fluid volume. $\dot{\gamma}$ is the prescribed shear rate.

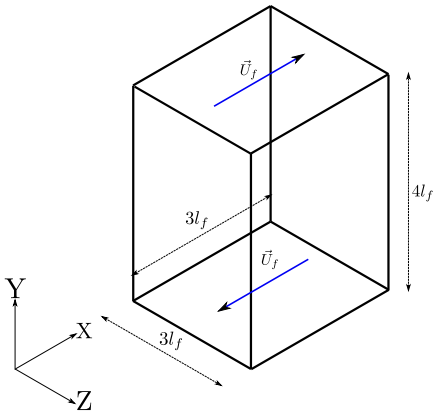

(a) Schematic of flow domain.

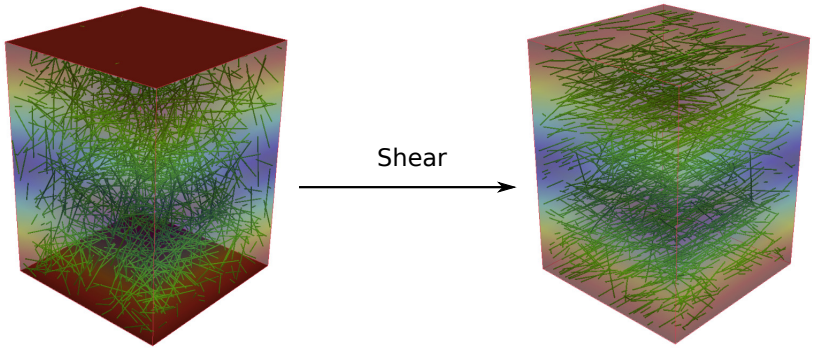

(b) Rigid fiber suspension with $r_p = 52$ at $c_v = 0.0075$.

Figure 6.1: Simulation setup. In fig. 6.1(b), the fluid velocity contours are shown in rainbow and the fibers in green.

r_p	l_f (mm)	d_f (μm)	E_y(GPa)	N_f	n_{seg}	nl_f^3	$nl_f^2 d$	c_v	$\dot{\gamma}(\text{s}^{-1})$	$N_x \times N_y \times N_z$
18	2.16	120	2.67	112	6	3.09	0.18	0.0075	300	$18 \times 24 \times 18$
				224		6.18	0.34	0.015		
				520		14.43	0.80	0.035		
32	3.84		20.37	352	10	9.77	0.30	0.0075	300	$30 \times 40 \times 30$
				704		19.55	0.61	0.015		
				1640		45.63	1.40	0.035		
52	6.24		39.4	930	15	25.80	0.49	0.0075	100	$45 \times 60 \times 45$
				1860		51.64	1.00	0.015		

Table 6.1: Fiber parameters used in the study. $N_x \times N_y \times N_z$ are the number of nodes by which the fluid domain is discretized in the X, Y and Z directions. The fluid viscosity was set to 13 Pa s.

6.3 Results and discussion

In this section the results of the two-way coupled numerical simulations of semi dilute rigid fiber suspensions are presented. First comparisons of the microstructure descriptors based on the fiber orientation are shown. Second, the stress states of the studied semi-dilute fiber suspensions are presented.

6.3.1 Suspension microstructure

Figure 6.2 depicts a single fiber in a shear flow (shear in XY planr). The angle $\phi \in [0, 2\pi)$ is the angle between the unit vector $\vec{p}$ parallel to the symmetric axis of the fiber and the velocity gradient direction. $\theta \in [0, \pi)$ is the angle between the unit vector $\vec{p}$ and the vorticity direction Z.

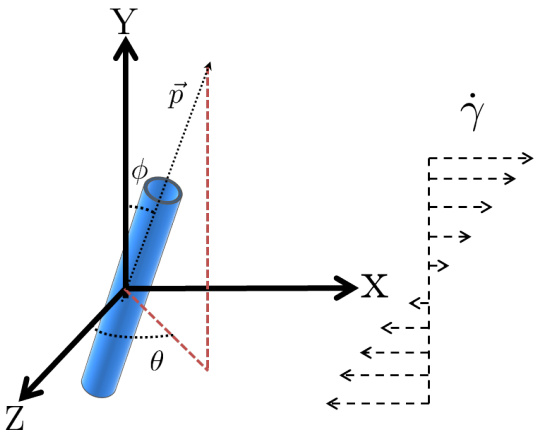

Figure 6.2: Rigid fiber in a shear flow, shear in XY plane. $\vec{p}$ is the unit vector parallel to the symmetric axis of the fiber. p_x and p_y are the projections of $\vec{p}$ in the flow direction **X** and gradient direction **Y**)respectively.

Jeffery [70] analytically showed that an ellipsoid immersed in an ubounded shear flow would rotate in 'orbits' about the vorticity axis. These orbits are characterized by the orientations ϕ and θ. For an ellipsoid with aspect ratio r_{el} immersed in a flow with shear rate $\dot{\gamma}$, the time period of the rotation (τ) of the ellipsoid is :

$$\tau = \frac{2\pi\dot{\gamma}}{r_{\text{el}} + \frac{1}{r_{\text{el}}}}. \tag{6.7}$$

Bretherton [24] showed that equation (6.7) is valid for rigid cylinders provided that the aspect ratio of the cylinder is replaced with an effective aspect ratio r_e. In the present study, the effective aspect ratio r_e is calculated based on the expression derived by Cox [41]:

$$r_e = 1.24 r_p \frac{1}{\sqrt{\ln r_p}} \tag{6.8}$$

Mason and Manley [112], based on Jeffery's theoretical work [70] derived the following expression for the probability distribution function $p(\phi)$ of fiber orientation angle ϕ:

$$p(\phi) = \frac{r_e}{2\pi\left(r_e^2 \cos^2\phi + \sin^2\phi\right)}. \tag{6.9}$$

Figure 6.3 shows the PDF of ϕ obtained for $r_p = 32$, in the semi dilute regime ($nl_f^3 = 45.6$) in comparison with Jeffery's equation. From the figure it is seen that the distribution is slightly asymmetric indicating the presence of fiber-fiber interactions, similar distribution was obtained in the experimental study of Stover *et al.* [160].

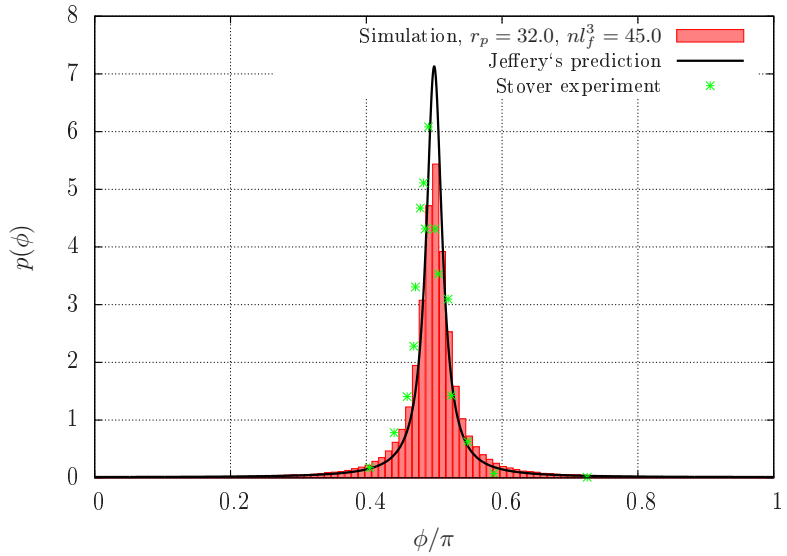

Figure 6.3: PDF comparison of numerically obtained ϕ with Jeffery's prediction (6.9) and Stover's experimental results [160] for $r_p = 32$, $nl^3 = 45.63$.

In creeping flow and for isolated non-Brownian fibers, the motion of the fibers can be characterized by an orbit constant C. The orbit constant is defined as the elliptical path traced out by the unit vector $\vec{p}$. $C = 0$ corresponds to perfect alignment in the XZ plane (vorticity axis) and $C = \infty$ corresponds to rotations in the XY plane (shear plane). The orbit constant C is defined as

$$C = \frac{1}{r_e} \tan\theta \sqrt{r_e \cos^2\phi + \sin^2\phi}. \tag{6.10}$$

Following the studies reported in refs. [160, 98, 141], the alternative orbit constant $C_b = (C/1 + C)$ was used in the present study so that C_b ranges between 0 and 1.
Figure 6.4 shows the comparison of the probability distribution function $p(C_b)$ with respect to the experimental results of Stover *et al.*[160]. The PDF shown in figure 6.4 was obtained over several time periods of rotation. From figure it is observed that the C_b distribution is nearly isotropic and is different from the distribution of dilute suspensions [4], in which lower orbit constants are preferred.
Within the semi dilute regime concentration ($1 < nl_f^3 < r_p$), the C_b distribution is qualitatively similar as shown in figure 6.5. However it is observed that the peak of the PDF shifts towards lower orbit constants. The obtained values of $< C_b >$ are compared with the experimental values as shown in table 6.2.

r_p	$\langle C_b \rangle$ present study	$\langle C_b \rangle$ Stover [160]	$\langle C_b \rangle$ Petrich [129]
18	0.459	0.450	–
32	0.413	0.408	–
52	0.378	–	0.365

Table 6.2: Comparison of $\langle C_b \rangle$ with experimental studies.

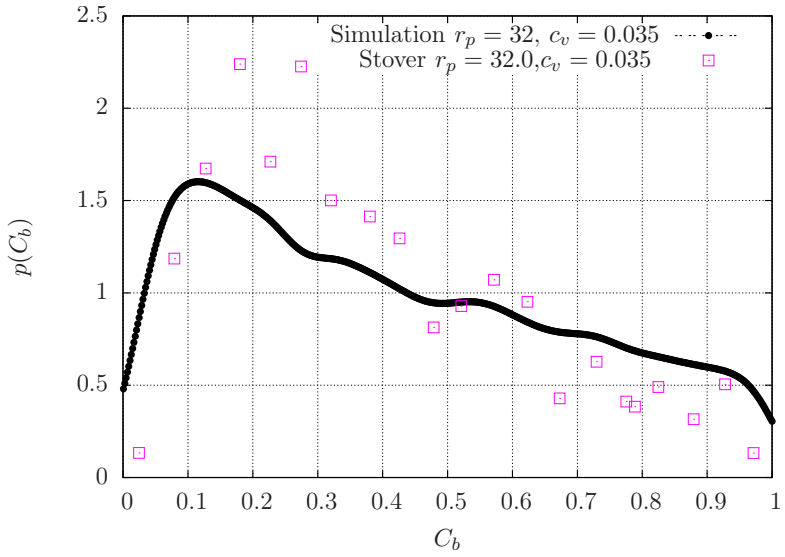

Figure 6.4: PDF of orbit constant C_b for $r_p = 32$ and $c_v = 0.035$. For other concentrations, the shape of the PDF was found to be similar (fig. 6.5).

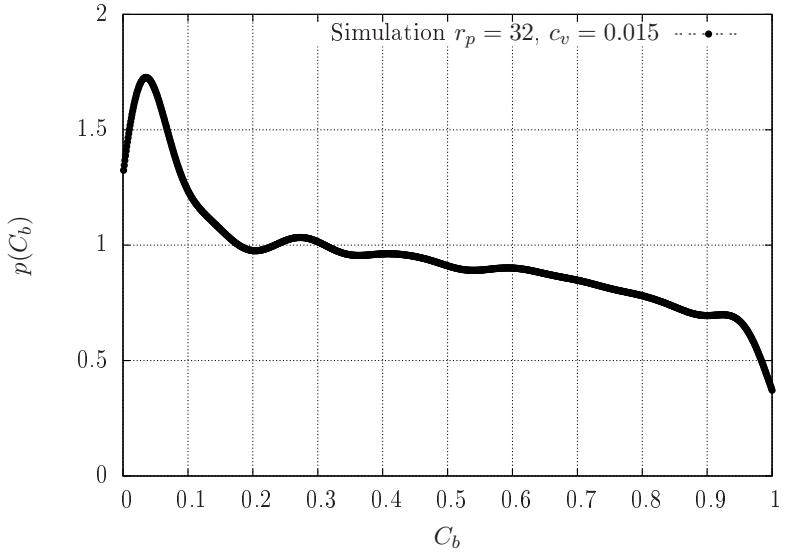

Figure 6.5: PDF of orbit constant C_b for $r_p = 32$ and $c_v = 0.015$.

In the theories predicting the relative viscosity (equations (6.16)) of fiber suspensions in shear, μ_{rel} depends on the quantity $\langle p_x^2 p_y^2 \rangle$ (p_x, p_y and p_z are the components of the unit vector $\vec{p}$). For suspensions in the semi-dilute regime, Stover [160], and Petrich [129] observed that $\langle p_x^2 p_y^2 \rangle$ was independent of the fiber volume fraction c_v. Figures 6.6(a) and 6.6(b) show the convergence of the numerically obtained values for $\langle p_x^2 p_y^2 \rangle$.
Figure 6.7 shows the comparison of $\langle p_x^2 p_y^2 \rangle$ for different fiber aspect ratios and concentrations with the experimental results of Petrich *et al.* and Stover *et al.* [129, 160]

Koch [82] derived a correlation for the structure/orientation moment $\langle p_x^2 p_y^2 \rangle$ of fiber suspensions based on the theoretical studies of Rahnama *et al.* [134] and the experimental studies of Stover *et al.* [160]. The following correlation was derived for shear flow:

$$\langle p_x^2 p_y^2 \rangle \approx \frac{0.371}{r_p}. \tag{6.11}$$

Table 6.3 shows rather good agreement between the numerically obtained $\langle p_x^2 p_y^2 \rangle$ with the

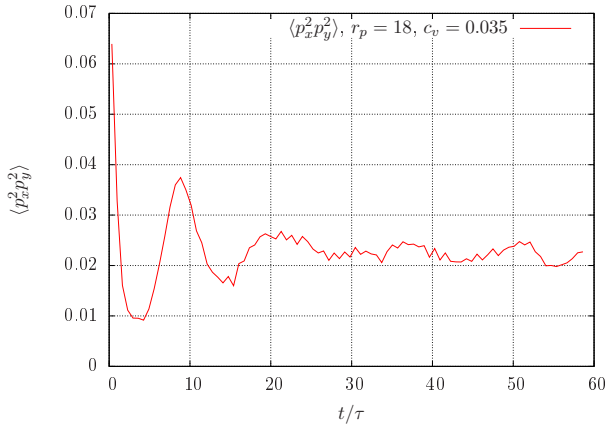

(a) $r_p = 18$, $c_v = 0.035$

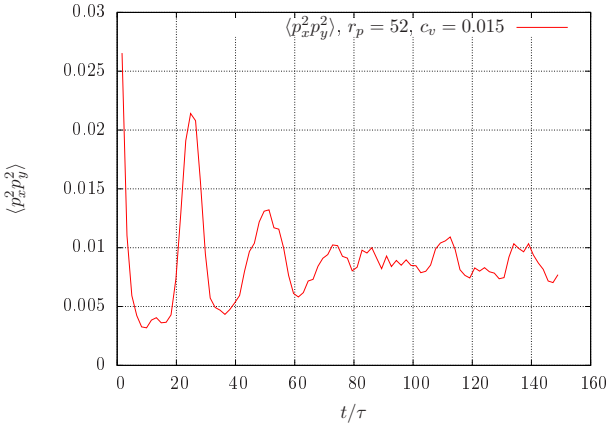

(b) $r_p = 52$, $c_v = 0.015$

Figure 6.6: Convergence of $\langle p_x^2 p_y^2 \rangle$ as a function of normalized time t/τ with τ the time period of Jeffery's orbit.

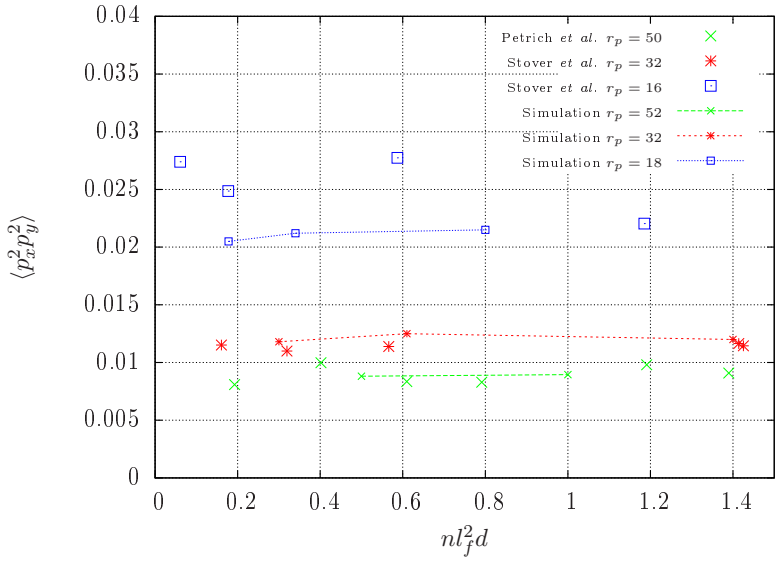

Figure 6.7: Comparison of $\langle p_x^2 p_y^2 \rangle$ with the results of experimental studies [160, 129]

correlation (6.11).

r_p	nl_f^2d	Simulations $\langle p_x^2 p_y^2 \rangle$	Correlation $\frac{0.371}{r_p}$
18	0.178	0.0205	0.0206
18	0.34	0.0212	
18	0.80	0.0215	
32	0.30	0.0118	0.0115
32	0.61	0.0125	
32	1.40	0.0120	
52	0.49	0.00881	0.00713
52	0.99	0.00895	

Table 6.3: Comparison of $\langle p_x^2 p_y^2 \rangle$ against Koch's correlation [82]

6.3.2 Suspension rheology

In this section the rheological properties obtained from the numerical simulations are compared with the predictions of Shaqfeh and Fredrickson [146] for semi-dilute suspensions ()equations (6.16) to (6.18)) and various experimental results [129, 16, 160].

The total stress tensor of the fiber suspension is defined as:

$$\boldsymbol{\Sigma}_{\text{susp}} = \underbrace{2\mu \boldsymbol{E} - p\boldsymbol{I}}_{\sigma_{\text{fluid}}} + \boldsymbol{\sigma}_{\text{fiber}}. \tag{6.12}$$

For shear flow, the first and second normal stress differences N_1 and N_2 are defined as

$$N_1 = \Sigma_{11} - \Sigma_{22}, \tag{6.13a}$$

$$N_2 = \Sigma_{22} - \Sigma_{33}. \tag{6.13b}$$

The relative viscosity μ_{rel} of the suspension is defined as follows:

$$\mu_{rel} = \frac{\Sigma_{12}}{2\mu E_{12}}. \tag{6.14}$$

In equations (6.13a), (6.13b) and (6.14), Σ_{ij} correspond to the components of the suspension stress tensor $\boldsymbol{\Sigma}_{\text{susp}}$. In the present study, the stress of the suspension was calculated via Direct Numerical Simulations. The following volume averaged expression was used to calculate the stress tensor of the fiber suspension

$$\boldsymbol{\Sigma}_{\text{susp}} = \left[\left(\int_V \boldsymbol{\sigma}_{\text{fluid}} dV \right) + \underbrace{\left(\sum_{i=1}^{N_{\text{fiber}}} \sum_{j=1}^{N_{\text{seg}}} \left(\vec{F}_{\text{int}i,j} \otimes \vec{p}_{i,j} dl \right) \right)}_{\text{Fiber contribution to stress}=\sigma_{\text{fiber}}} \right] \frac{1}{V}, \tag{6.15}$$

where in equation (6.15), $\boldsymbol{\sigma}_{\text{fluid}}$ is the volume averaged fluid stress tensor, $\vec{F}_{\text{int}}$ is the interaction force on a given fiber segment.

In addition to the direct calculation of the stress by expression (6.15), the normal stress differences and the effective viscosity of the suspension for dilute and semi-dilute rigid fiber suspensions can be calculated from the orientation of the fiber [13, 146] as it has been previously mentioned in the introduction of this chapter. The first and normal stress differences (N_1 and N_2, '*' refers to the theoretical expression) reads as:

$$N_1^* = \mu_{\text{fiber}} \dot{\gamma} \left(\langle p_x^3 p_z \rangle - \langle p_z p_y^3 \rangle \right), \tag{6.16a}$$

$$N_2^* = \mu_{\text{fiber}} \dot{\gamma} \left(\langle p_x^3 p_z \rangle - \langle p_x p_y p_z^2 \rangle \right). \tag{6.16b}$$

The expression for the relative viscosity of the suspension reads:

$$\mu^*_{\text{rel}} = 1 + \frac{\mu_{\text{fiber}}}{\mu}\langle p_1^2 p_2^2 \rangle. \tag{6.16c}$$

In equation (6.16), μ_{fiber} depends on the fiber concentration. For dilute suspensions, the expression of μ_{fiber} was derived by Batchelor [13]:

$$\mu_{\text{fiber}} = \frac{\pi n l_f^3 \mu}{6 \ln(2r_p)} f(\epsilon), \tag{6.17a}$$

where $\epsilon = (\ln(2r_p))^{-1}$, and $f(\epsilon)$ is defined as

$$f(\epsilon) = \frac{1 + 0.64\epsilon}{1 - 1.5\epsilon} + 1.659\epsilon^2. \tag{6.17b}$$

In the semi dilute regime, Shaqfeh and Fredrickson [146] proposed the following expression:

$$\mu_{\text{fiber}} = \frac{\pi n l_f^3 \mu}{3\left(\ln(1/c_v) + \ln(\ln(1/c_v)) + A\right)}. \tag{6.18}$$

In the present study, the stress of the fiber suspension is calculated directly using equation (6.15) and the results of this calculation is compared with the theory of Shaqfeh and Fredrickson [146] using the instantaneous fiber microstructure. In the present study, $A = 0.16$ was chosen.

	l_f (mm)	d_f (μm)	r_p	$\dot{\gamma}$ (s^{-1})	μ (Pa s)
Bibbo [16]	2.0	120	17	$1 - 100$	13
	4.0	120	33	$1 - 100$	13
	6.0	120	51	$1 - 100$	13
Stover [160]	1.61	95	16.9	$0.319 - 0.471$	1
	2.68	84	31.9	$0.447 - 0.472$	1
Petrich [129]	0.65	13	50	0.50	27.5
	0.55	11	50	0.50	27.5
Present study	2.16	120	18	300	13
	3.84	120	32	300	13
	6.24	120	52	100	13

Table 6.4: Fiber parameters, dynamic viscosity μ and shear rate $\dot{\gamma}$ of various experimental studies and present study. The parameters l_f and d_f correspond to the fiber length and diameter respectively.

Table 6.4 gives the details of the experimental studies in comparison. The fiber parameters in the present study are based on the experimental study of Bibbo [16], except for the shear rate $\dot{\gamma}$. From table 6.4, it is observed that the shear rate ($\dot{\gamma}$) ranges from 10^{-2} to 10^2 s^{-1}. The shear rate in the present study was set to $\dot{\gamma} = 300s^{-1}$ and $\dot{\gamma} = 100s^{-1}$. Despite of a higher shear rate, the fiber Reynolds numbers based on the fiber diameter and normal component of the relative velocity was in the Stokesian regime as shown in figure 6.8. The Reynolds number based on the shear rate and the fiber diameter was found to be 3×10^{-4}. The relative viscosity μ_{rel} and the normal stress differences were calculated directly using equation (6.15) and using the semi-dilute [146] theory with the suspension microstructure obtained from the simulations. In order to avoid the wall effects, fibers close to the wall were neglected in the calculation using equation (6.15). The value of the fiber-wall distance corresponds to $0.25l_f$.

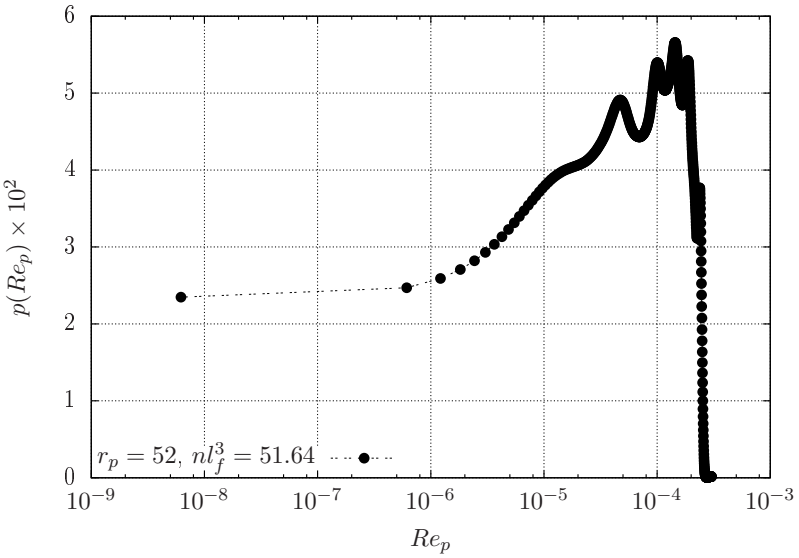

Figure 6.8: PDF of fiber Reynolds number $r_p = 52$, $nl_f^3 = 51.64$

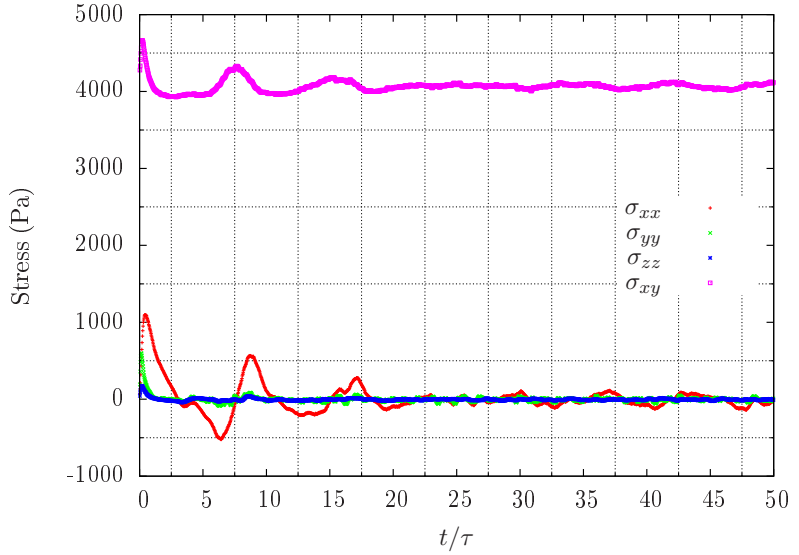

Figure 6.9: Convergence of fiber stress components for $r_p = 32$, $c_v = 0.0075$ as a function of t/τ.

Figures 6.9, 6.10(a) and 6.10(b) show the convergence of the individual stress components, first and second normal stress difference obtained from the direct stress calculation and using the analytical theory of Shaqfeh and Fredrickson [146]. Comparison of the relative viscosity obtained by the direct calculation and the semi-dilute theory is shown in figure 6.10(c).

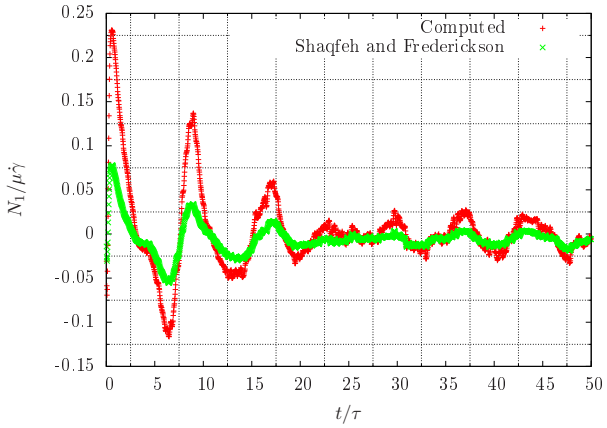

(a) Convergence of first normal stress difference N_1 for $r_p = 32$, $c_v = 0.0075$.

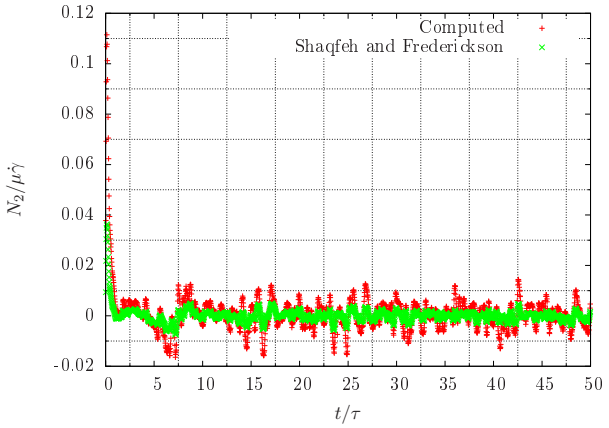

(b) Convergence of second normal stress difference N_1 for $r_p = 32$, $c_v = 0.0075$.

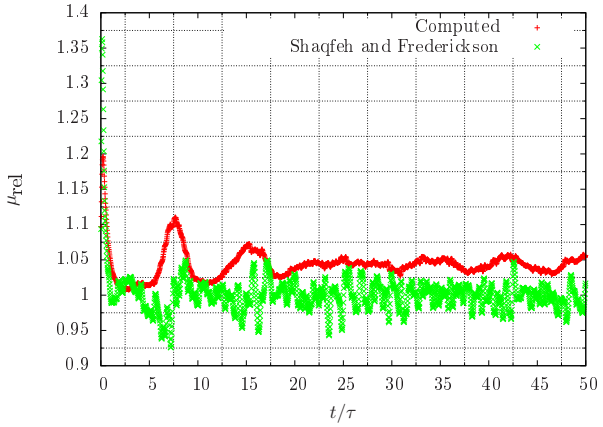

(c) Convergence of relative viscosity for $r_p = 32$, $c_v = 0.0075$

Figure 6.10: Convergence of the rheological properties of fiber suspension $c_v = 0.0075$, $r_p = 32$ as a function of t/τ

Figure 8.5 shows the comparison of the relative viscosity μ_{rel} between the experimental studies and the present numerical work. From the figure it is observed that the numerical results agree reasonably with the experimental results of Stover *et al.* for $r_p = 32$. Reasonable agreement is also observed with the results of Petrich *et al.* [129].

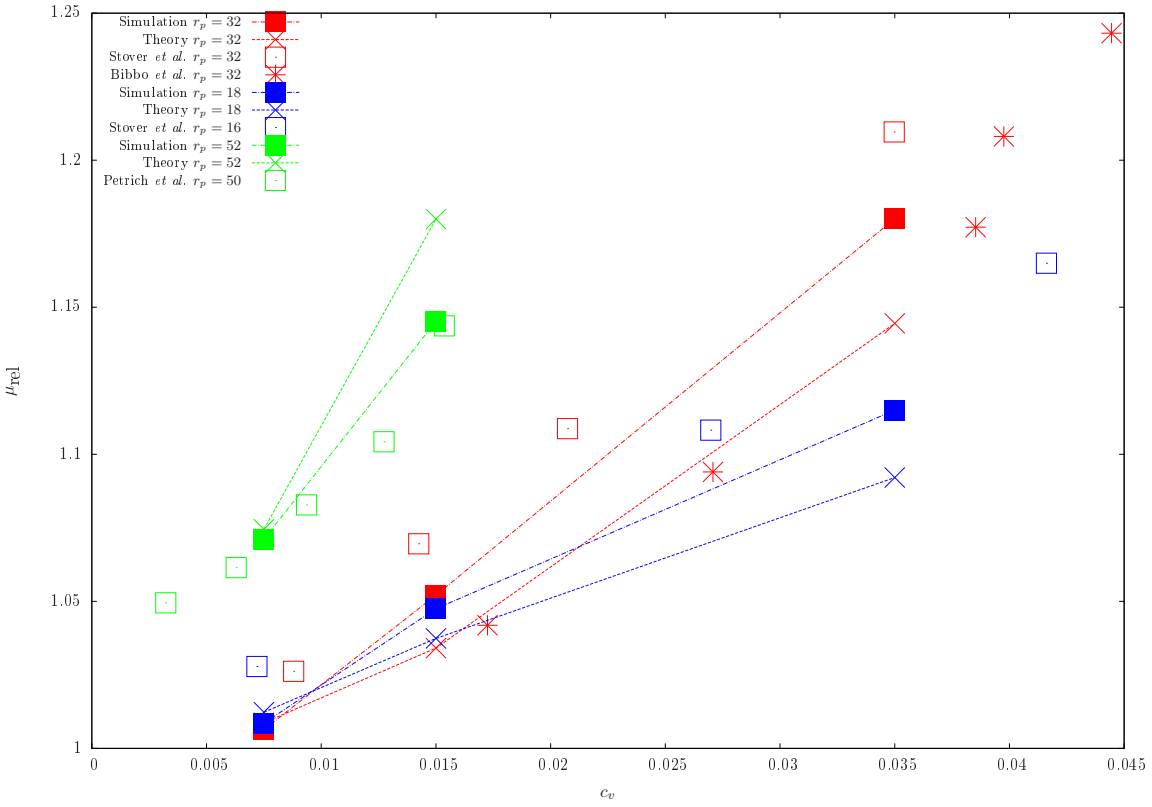

Figure 6.11: Comparison of the computed fiber suspension relative viscosity μ_{rel} with experimental results.

6.4 Conclusion

In this chapter, the evolution ot the microstructure and the rheological properties of semi dilute rigid fiber suspensions in shear flow was studied. Three fiber aspect ratios ($r_p = 18, 32, 52$) were considered and the concentration was varied from ($1 < nl_f^3 < r_p$). The results of the numerical simulations were compared with several experimental results and predictions of Batchelor and Shaqfeh and Fredrickson. It was observed that the developed numerical model takes into account the long range and short hydrodynamic interactions between the fibers. The effect of the interactions is evident the PDF of the ϕ orientation angle and orbit constant C_b distribution. Finally the rheological properties of the suspensions obtained from the numerical studies were compared with previous experimental results and the semi dilute suspension theory using the suspension microstructure parameters obtained frim numerical simulation. The developed numerical model was able to reproduce the evolution of the relative viscosity μ_{rel} of semi dilute fiber suspensions as a function of their concentrations with a reasonable accuracy.

CHAPTER 7

DRAG REDUCTION IN TURBULENT PIPE FLOW BY FIBROUS ADDITIVES

Contents

7.1 Introduction

The flow of fiber suspensions is critical in several applications such as in the manufacture of fiber based composites [43, 42], paper making [106] and as potential drag reducing agents [171]. The flow of fiber suspensions in these applications are usually in the inertial regime, ie. the Reynolds number and the Stokes number at the fiber scale are finite. One of the most important effects in these flows are the ability of the suspended fibers to enhance/damp turbulence. Robertson and Mason [135] performed experimental studies on the flow of dilute fiber suspensions in a pipe flow. The volume fraction of the fibers were varied from 0.1% to 1%. For fiber volume fractions greater than 0.2%, three different flow regimes were identified : plug flow, mixed turbulent flow and turbulent flow. For low bulk flow Reynolds numbers ($Re_{\text{bulk}} < 1500$), the plug flow regime was dominant for up to volume concentrations of 0.3%. In the regime between $2000 < Re_{\text{bulk}} < 3000$, transition to turbulence was observed. In fact the presence of fibers enhanced the turbulence for volume concentrations greater than 0.5%. For concentrations less than 0.7%, and in the regime between $6000 < Re_{\text{bulk}} < 50000$, drag reducing effects were observed (characterized by lower pressure drop and lower wall shear stress). For higher concentrations the flow was similar to a turbulent flow with reduced turbulence intensity in the streamwise direction but increased wall shear stress, the fibers formed a plug like annular structure for higher concentrations. For higher bulk flow Reynolds numbers ($Re > 60000$) the presence of fibers did not affect the velocity profiles of the flow and the flow was similar to a single phase turbulent pipe flow. Such phenomena have been observed in several studies of fiber suspensions in channel and pipe flows [182, 171, 92]. The effect of fiber aspect ratio on the drag reduction characteristics was studied experimentally in refs [78, 92]. In these studies it was found that fibers with higher aspect ratios ($30 < r_p < 300$) and dilute concentrations proved to be better drag reducing agents compared to short aspect ratios ($r_p < 30$) for the same volume fraction. The mechanism of drag reduction in turbulent channel flows was numerically studied by Paschkewitz *et al.* [122, 123]. The contribution of the fiber

stress were calculated using the constitutive equations involving the fiber orientation moments ($\int \vec{p} \otimes \vec{p}$ and $\int \vec{p} \otimes \vec{p} \otimes \vec{p} \otimes \vec{p}$) and closure approximations from the studies in refs. [36, 1]. The extra fiber stress term were added with Newtonian stress tensor in the NS equations. In their study, drag reduction of up to 26% were obtained and the drag reduction mechanism was found to be qualitatively similar to those that are induced by the use of polymers for drag reduction [49]. The streamwise fluctuating component of the velocity had a higher peak in the suspension compared to the single phase flow which is commonly observed in polymer solutions.
In this chapter, numerical simulations of dilute fiber suspensions in turbulent pipe flow were performed. Two fiber volume concentration $c_v = 0.0025$ and $c_v = 0.005$ were considered and the flow Reynolds number based on the pipe diameter was $Re = 6000$. The effect of fibers on the flow characteristics were obtained and the fiber microstructure was studied. Preliminary qualitative results such as the velocity profiles, root mean square of the fluctuating velocity components are presented. Due to the heavy time requirements of the simulation, the statistics were collected only for short duration ($\approx$ two flow through times.). Therefore high order statistics needed for the stress and energy budget did not reach the statistically stationary state and these results have not been presented.

7.2 Numerical Setup

The flow domain consisted of a pipe geometry with diameter $D_\mathrm{p} = 5l_f$ (l_f is the fiber length, $D_p = 0.006$ m) and the length of the pipe was set to $L_\mathrm{p} = 5D_\mathrm{p}$ (similar to the DNS studies of Eggels *et al.* [54]). The pipe geometry was discretized into a hybrid unstructured mesh consisting of 3.7×10^6 cells, with 20 layers of hexahedral cells in the wall normal direction starting from $y^+ = 0.05$ with a growth ratio of 1.20. Periodic boundary condition was applied in the streamwise **x** direction and the no slip wall boundary condition was imposed over the pipe surface. The density ρ_fluid and dynamic viscosity μ of the fluid were set to 1000 kg/m^3 and 0.001 Pa s respectively. Figure 7.1 shows the initial fiber microstructure and the flow domain. Table

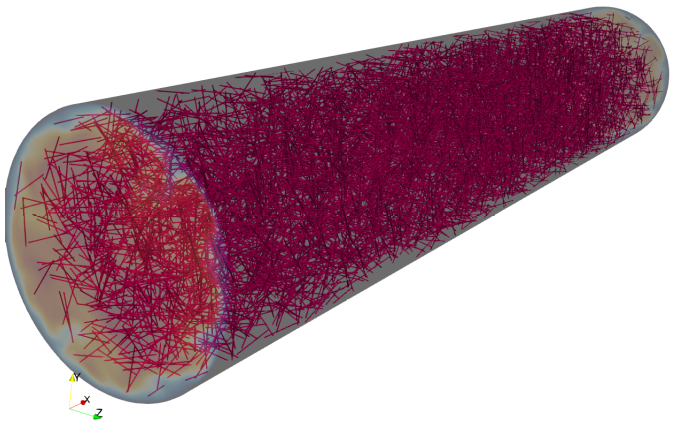

Figure 7.1: Flow domain and fibers. The fibers are shown in pink and the contours correspond to the flow velocity magnitude. The initial fiber positions and orientations were randomly generated inside a cylindrical geometry.

7.1 gives the fiber properties used in the present study. The aspect ratio r_p of the fibers was set to $r_p = 50$.
The single phase turbulent pipe flow was driven using a forcing $\vec{f_x}$ in the stream-wise direction X to maintain a constant pressure gradient at a bulk Reynolds number $Re_{D_p} = 6000$ (equation

c_v	N_f	N_{seg}	l_f (mm)	d_f (μm)	r_p	nl_f^3	E_Y(GPa)
0.0025	3905	20	1.20	24	50	7.95	2.1
0.005	7804					15.91	

Table 7.1: Fiber properties and discretization used in the present study. The fibers are considered to be neutrally buoyant.

(7.1)). The corresponding Reynolds number based on the friction velocity u_τ ($u_\tau = \sqrt{\tau_w/\rho}$, with τ_w the wall shear stress) was $Re_\tau = 367$.

$$\frac{\partial \vec{U}}{\partial t} + \nabla\left(\vec{U} \otimes \vec{U}\right) = \vec{f_x} - \frac{\nabla p}{\rho_{\text{fluid}}} + \nu \nabla^2 \vec{U}. \tag{7.1}$$

Initially the forcing $\vec{f_x}$ was calculated using the analytical expressions from boundary layer theory in ref [143]. To do so, first, the friction factor f for turbulent pipe flows in smooth pipes was calculated using the Colebrook equation [176]:

$$\frac{1}{\sqrt{f}} = 2\log_{10}\left(\sqrt{f} Re_{D_p}\right) - 0.8. \tag{7.2}$$

The an estimate of the wall shear stress τ_w was obtained using

$$\tau_w = \frac{1}{2}\rho_{\text{fluid}}\left(\vec{U}\right)^2 C_f, \tag{7.3a}$$

and

$$f = 4C_f \tag{7.3b}$$

For fully developed turbulent pipe flow, the force balance equation reads as

$$\vec{F_x} = \tau_w \pi D_p L_p = -\frac{1}{4}\frac{dp}{dx}\pi D_p^2 L_p. \tag{7.4a}$$

Finally, for constant pressure gradient, the volumetric forcing term is:

$$\vec{f_x} = \frac{\vec{F_x}}{\rho_{\text{fluid}} V_{\text{fluid}}}. \tag{7.4b}$$

For the fiber suspension case, the value of $\vec{f_x}$ obtained from single phase flow simulation was used and the simulations were run until a convergence in the fluid bulk velocity was observed. The viscous length scale δ_v is defined as follows:

$$\delta_v = \frac{\nu}{u_\tau}, \tag{7.5}$$

where ν is the fluid kinematic viscosity. In the present study, the diameter d_f of the fiber is comparable to the the viscous length scale δ_v as $d_f/\delta_v = 1.47$.

7.3 Results and discussion

Figure 7.2 shows the comparison of the mean velocity profile in the streamwise direction X direction between the present study ($Re = 6000$) and the experimental/DNS results of Eggels *et. al* [54] ($Re = 5300$) for single phase flow ($c_v = 0$) simulation. The mean velocity $\langle U_x \rangle$ in the streamwise direction was normalized by the friction velocity u_τ that numerically obtained from the wall shear stress, i.e. $u_\tau = \sqrt{\tau_w/\rho}$. The velocity profile obtained from the DNS in the present study is in reasonable agreement with the DNS results reported by Eggels *et al.* [54].

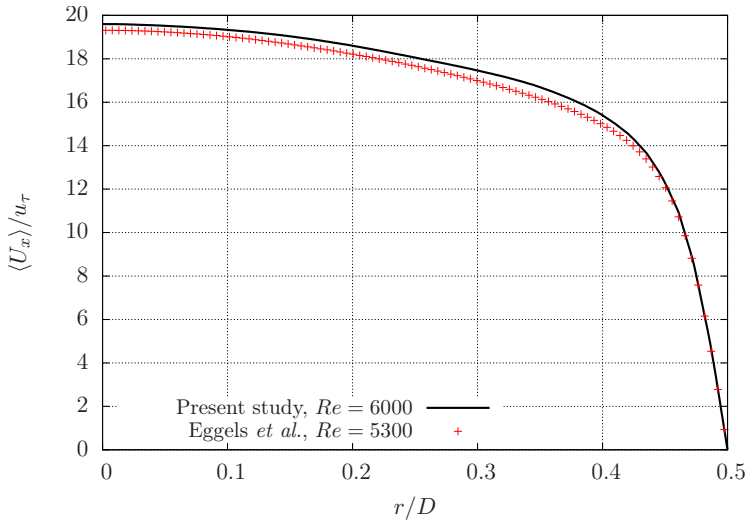

Figure 7.2: Comparison of mean velocity profiles between present DNS (single phase) and Eggels *et al.* [54]

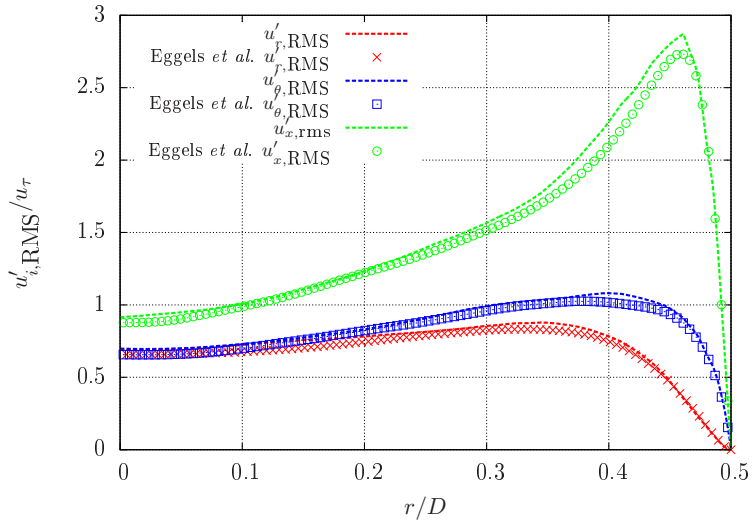

Figure 7.3: Comparison of u'_i RMS components between present DNS (single phase) and Eggels *et al.* [54] numerical results.

Figure 7.3 shows the root mean square(RMS) of the fluctuating fluid velocity components. The RMS components give an indication of the turbulence intensity. The RMS profiles obtained in the present study are also in good agreement with the DNS results of Eggels *et al.* [54]
The velocity field of the single phase DNS was used as the initial condition for the simulation of the fiber suspension flow. In figure 8.9, the velocity profiles of the single phase flow and fiber suspension flow are shown in wall units y^+ (inner units). The y^+ can be seen as a local Reynolds number and it is defined as

$$y_i^+ = \frac{\rho u_\tau y_i}{\mu}, \tag{7.6}$$

where in equation (7.6), y_i is the wall normal coordinate. The mean velocity is normalized by the friction velocity u_τ so as to obtain $u^+ = \langle U_f \rangle / u_\tau$. Figure 8.9 shows that in the case of the suspension flow, there appears to be a thickening in the viscous sublayer ($y^+ < 5$) and closely follows the trend given by $u^+ = y^+$ for y^+ up to 10 or more precisely up to a portion of the

buffer layer $5 < y^+ < 30$. Laminar flows follow the trend of $u^+ = y^+$ for the entire y^+. The deviation from this trend gives an indication of the drag reduction in the near wall region. In addition, it was also observed that the friction velocity u_τ for the flow of the fiber suspension was lower compared to the single phase flow implying, a reduction in the wall shear stress τ_w.

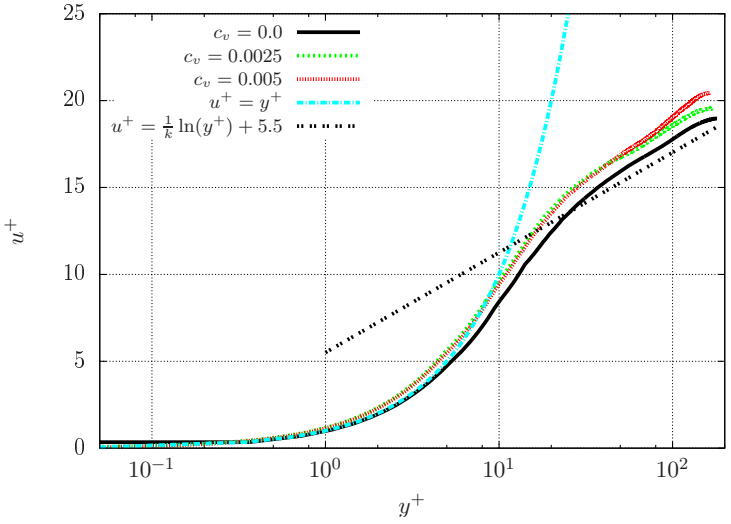

Figure 7.4: Comparison between mean velocities obtained for single phase flow and fiber suspension flow in wall units.

Similar trends in the velocity profiles were obtained in the numerical study of Paschkewitz *et al.* [122]. Significant differences in the velocity profiles were observed in the log-law layer ($y^+ > 30$) and the outer layer ($y^+ > 50$) between the fiber suspension flow and and the single phase flow. In the case of single phase flow, the velocity profile follows the log-law of:

$$u^+ = \frac{1}{k}\ln y^+ + B, \tag{7.7}$$

where in equation (7.7), k is the von-Kármán constant and for pipe flow, $k = 0.40$ [188]. B is the the additive constant, $B = 5.5$. The velocity profiles of the fiber suspension flow were comparatively higher in these regions.
Figure 7.5 shows the comparison of the root means square (RMS) of the fluctuating velocity components u'_x (streamwise direction), u'_θ (azimuthal direction) and u'_r (radial direction) with respect to the outer units (r/D_p). The RMS of the fluctuating velocity components indicates the turbulence intensity.
In figure 7.5(a), the RMS of the streamwise fluctuating component u'_x was found to be higher for the fiber suspension flow. This behavior has been observed both numerically and experimentally in the drag reducing flows by polymer additives in Newtonian fluids [49, 105]. However the mechanism of the drag reduction by polymer additives are different, the drag reduction in such suspensions are essentially associated to the change of shape of the polymer, *i,e.* initially coiled polymers are stretched in the near wall region. Drag reducing trends have been observed for rigid fiber suspensions in the experimental study of Xu and Aidun [182]. In the later section of this chapter, an attempt to explain this behavior using the fiber microstructure is presented. It is also observed that the RMS components of the fiber suspension flow are reduced in the azimuthal and radial directions (figures 7.5(c) and 7.5(b)). Such trends have been observed in particle laden turbulent channel flows [101, 9].

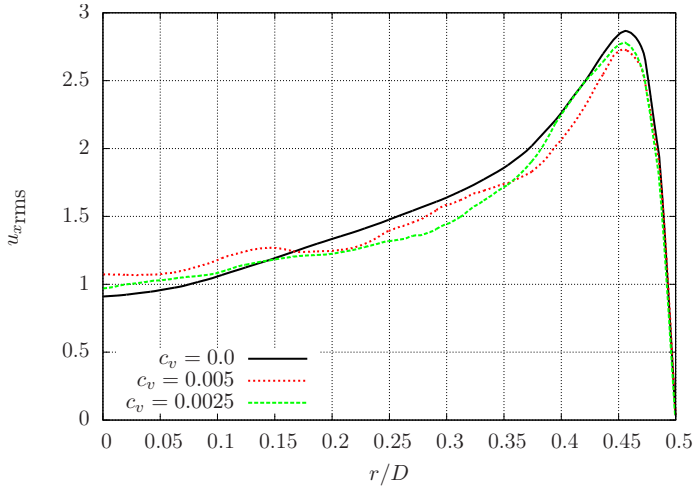

(a) $u'_{x,rms}$

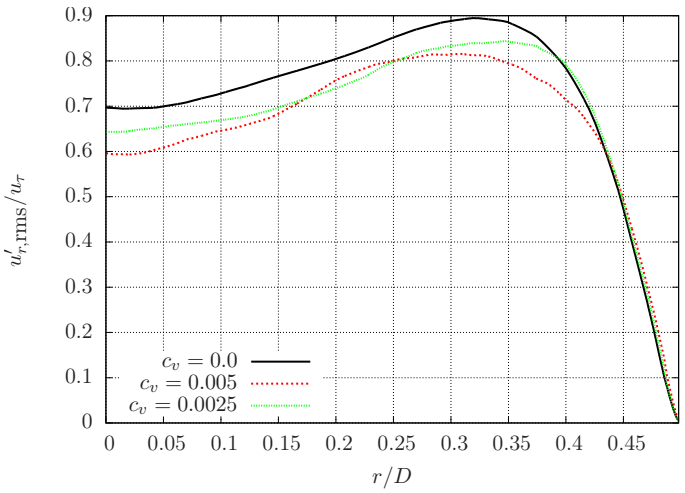

(b) $u'_{r,rms}$

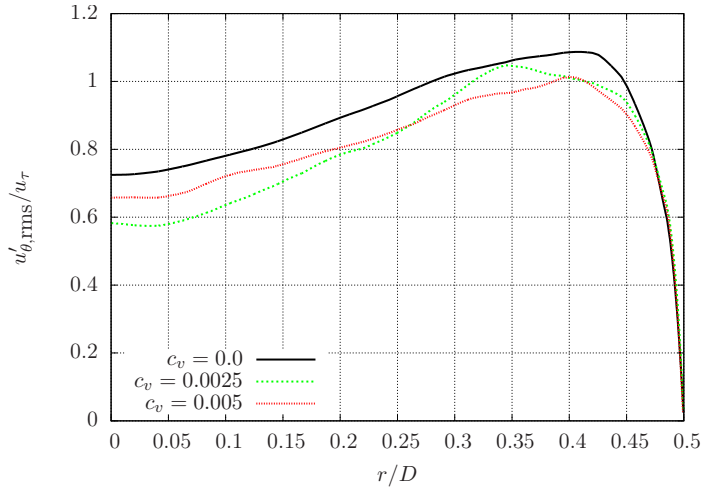

(c) $u'_{\theta,rms}$

Figure 7.5: Comparison of velocity fluctuations between single phase flow and fiber suspensions.

Figure 7.6(a) show the profile of the fluid stress (for both the single phase and fiber suspension cases) in the velocity gradient direction normalized by the wall shear stress τ_w of the single phase

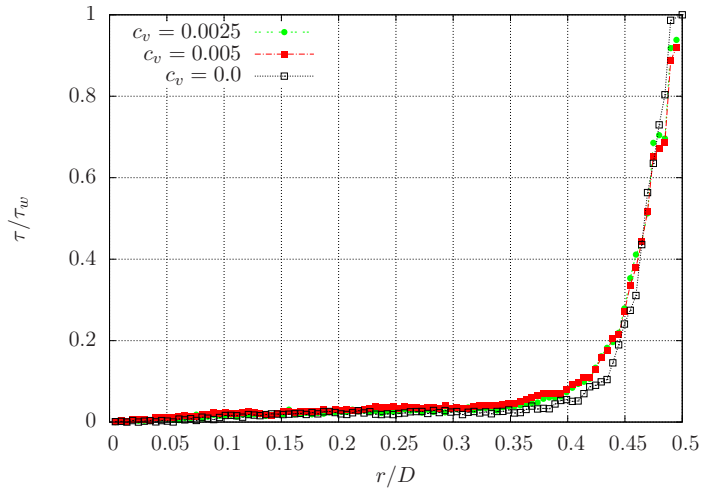

(a) Profile of the stress in the wall normal direction for fluid, normalized by wall shear stress τ_w of the single phase fluid.

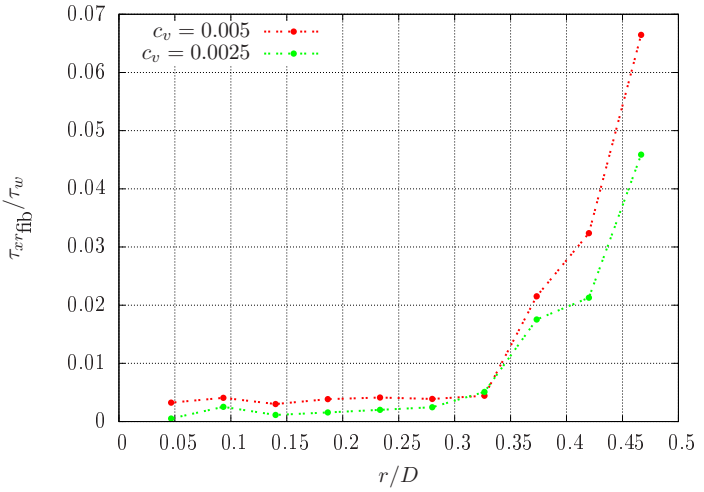

(b) Component of the fiber stress τ_{xr}

Figure 7.6: Stress profiles in the velocity gradient direction.

flow with respect to the outer units. Figure 7.6 shows that the presence of fibers reduced the stress in the near wall region (for $r/D_p \approx 0.47$ to 0.5) and an increase in the stress in the log-law region was observed. Figure 7.6(b) shows the variation of the fiber contribution to the stress for the two concentrations studied. In order to calculate the fiber stress, the pipe domain was divided in to 10 annuli with varying radii. The stress was calculated using the following equation (as explained previously in Chapter 6.).

$$\tau_{\text{fib}} = \left(\sum_{i=1}^{N_{\text{fiber}}} \sum_{j=1}^{N_{\text{seg}}} \left(\vec{F}_{\text{int}i,j} \otimes \vec{p}_{i,j} \right) \right) \frac{1}{V_{\text{i}}} \tag{7.8}$$

where in equation (7.8), $\vec{F}_{\text{int}}$ corresponds to the internal force on the fiber segments, $\vec{p}$ is the orientation of the fiber segments and V_i is the volume of the considered annular region.
The percentage in drag reduction ($DR\%$) was defined as [122]:

$$DR\% = 1 - \left(\frac{u_{\tau,\text{susp}}}{u_{\tau,\text{sp}}} \right)^2 \times 100 \tag{7.9}$$

where in equation (7.9), $u_{\tau,\text{susp}}$ is the friction velocity obtained from the fiber suspension flow and

$u_{\tau,\mathrm{sp}}$ is the friction velocity obtained for single phase flow (both these velocities were obtained using the relation $u_\tau = \sqrt{\tau_w/\rho}$). In the present study the percentage in drag reduction was found to be 7.75% for $c_v = 0.0025$ ($nl^3 = 7.95$) and 12.8% for $c_v = 0.005$ ($nl^3 = 15.91$), thereby showing a clear effect of the increase in fiber concentration on the drag reduction. Figure 7.7

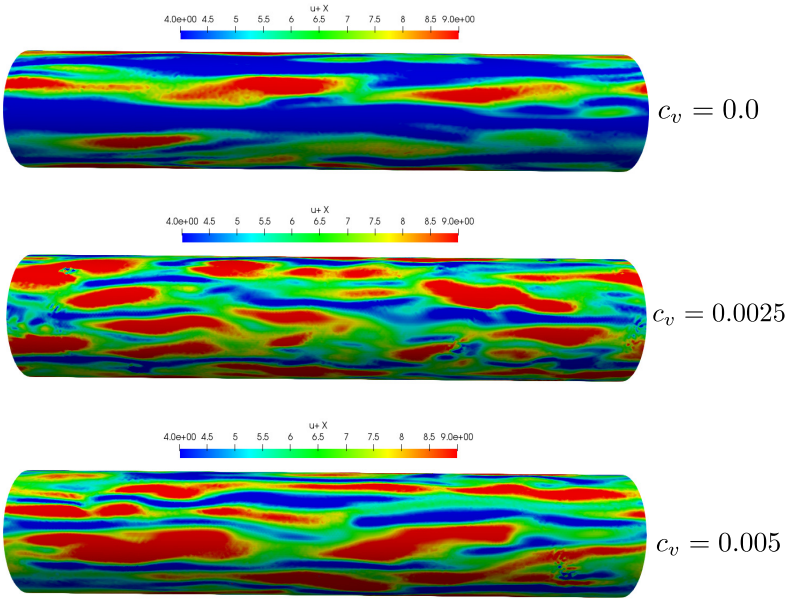

Figure 7.7: Comparison of instantaneous velocity contours at $y^+ = 6$

shows the instantaneous contours of the flow velocity on the iso-surface at the near wall region ($y^+ = 6$). It is observed that the fibers strongly modulate the flow in this region as seen in the velocity profile (figure 8.9) and the presence of high speed streaks (shown in red) in figure 7.7. Figure 7.8 shows the comparison of the PDF of the fiber segment orientation between the two volume fractions considered in the present study where θ is the angle between the fiber segment axis and the flow direction and the angle ϕ is normal to the flow direction.

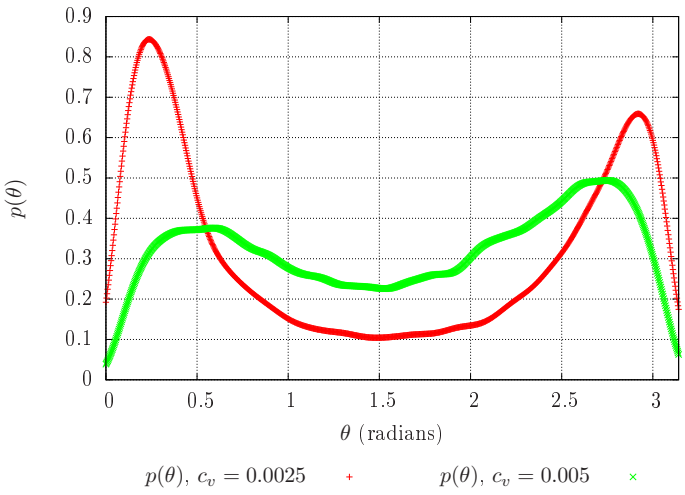

Figure 7.8: Comparison of PDF of θ

Figure 7.8 shows that for low volume fraction ($c_v = 0.0025$), the fibers tend to align with the flow direction whereas in the case of $c_v = 0.005$, the distribution was comparatively isotropic i.e. showing a more random orientation. In order to get a clearer idea of the orientation distribu-

tion, the pipe domain was divided into 10 annular regions with varying radii. The orientation distribution of the fiber segments in each of these regions are shown in figures 7.9 and 7.10.

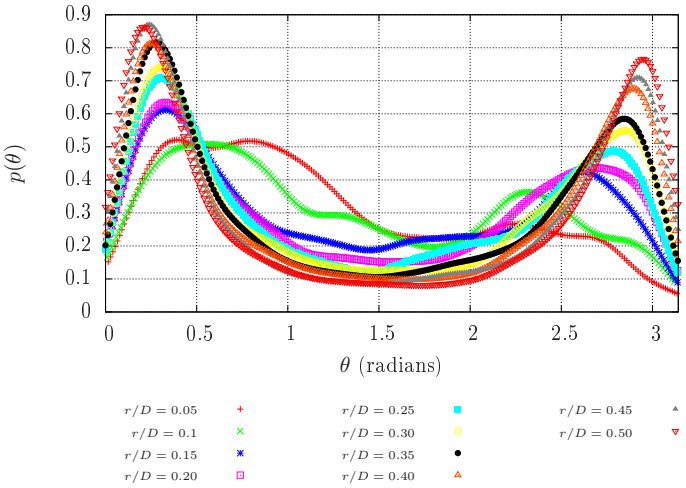

(a) $p(\theta)$ for varying r

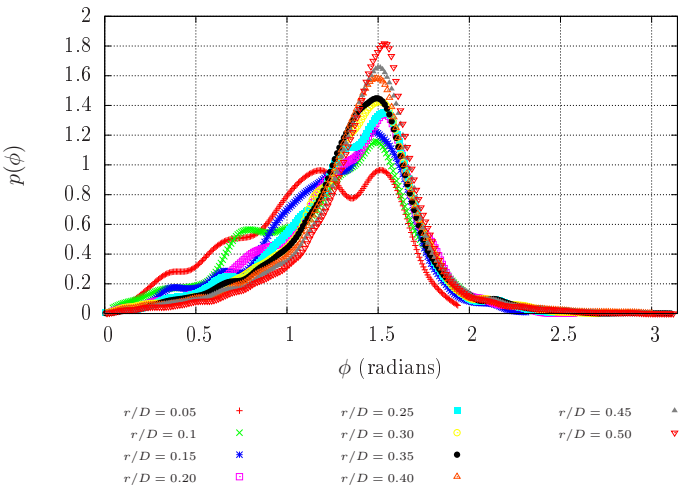

(b) $p(\phi)$ for varying r

Figure 7.9: Comparison of PDF of θ and ϕ for varying annular regions within the pipe, $c_v = 0.0025$

In figure 7.9, preferential alignment was observed for the fiber segments at the near wall region and the orientation distribution tends to be isotropic towards the core of the pipe. However in the case of $c_v = 0.005$ near isotropic distribution were seen throughout the pipe domain with slight preferential alignment in the near wall region. Such an effect is mainly due to the fiber-fiber interactions and fiber deformation. Evidence of fiber deformation is shown in figure 7.11. Figure 7.11 shows the PDF of the end-to-end vector $\vec{Z}_e$ for the two studied concentrations. It was observed that for the case with $c_v = 0.005$, the fibers tend to undergo more deformation, as the peak of the PDF is lower. It should be noted that the fibers are not very flexible, as the maxima of $\langle \vec{Z}_e^2 \rangle / \vec{Z}_e^2$ is around 1.02 (for rigid fibers, $l_f^2 = \vec{Z}_e^2$). Note that similar PDF profiles were obtained in the experimental study of Brouzet *et al.* [28] for nearly rigid fibers in homogeneous isotropic turbulent flow.

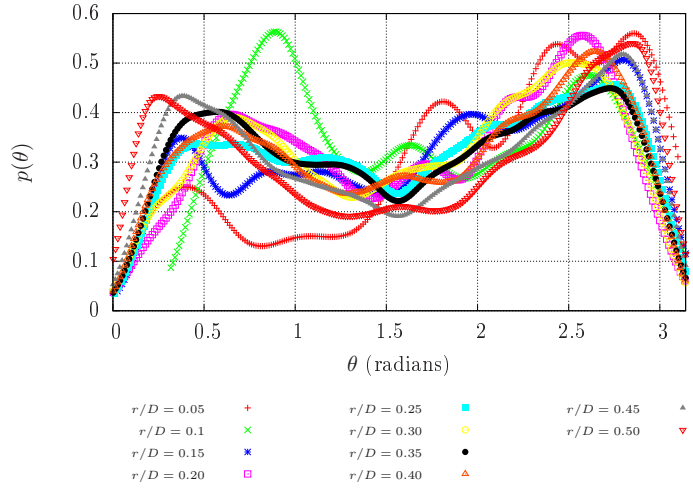

(a) $p(\theta)$ for varying r

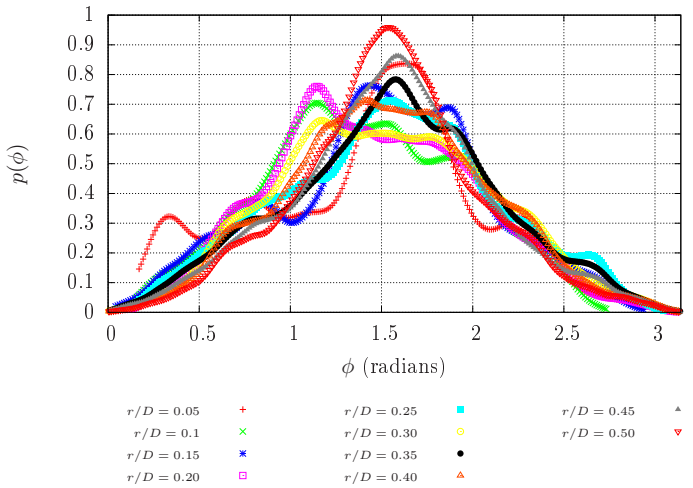

(b) $p(\phi)$ for varying r

Figure 7.10: Comparison of PDF of θ and ϕ for varying annular regions within the pipe, $c_v = 0.005$

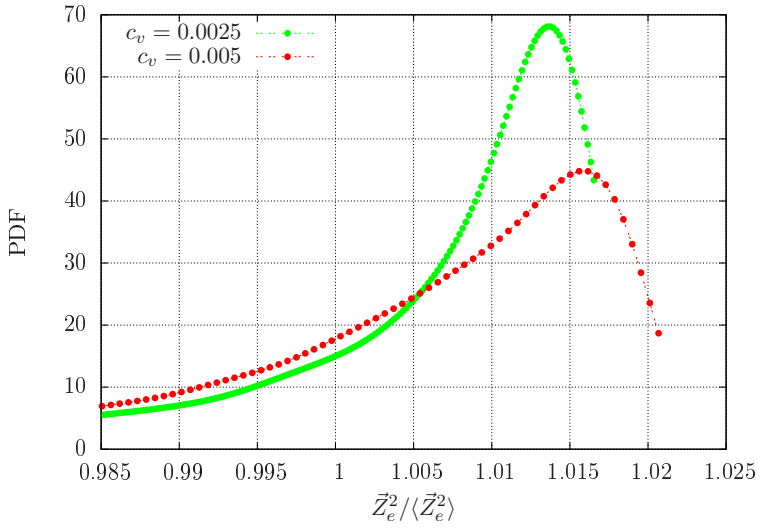

Figure 7.11: PDF of end to end vector $\vec{Z}_e$ for the two studied suspensions with $c_v = 0.0025$ and $c_v = 0.005$.

Figure 7.12 shows the instantaneous fiber microstructure for the two volume fractions. In the case of $c_v = 0.005$ fiber flocculation was observed intermittently and floc formation was qualitatively observed to increase the deformation of the fibers.

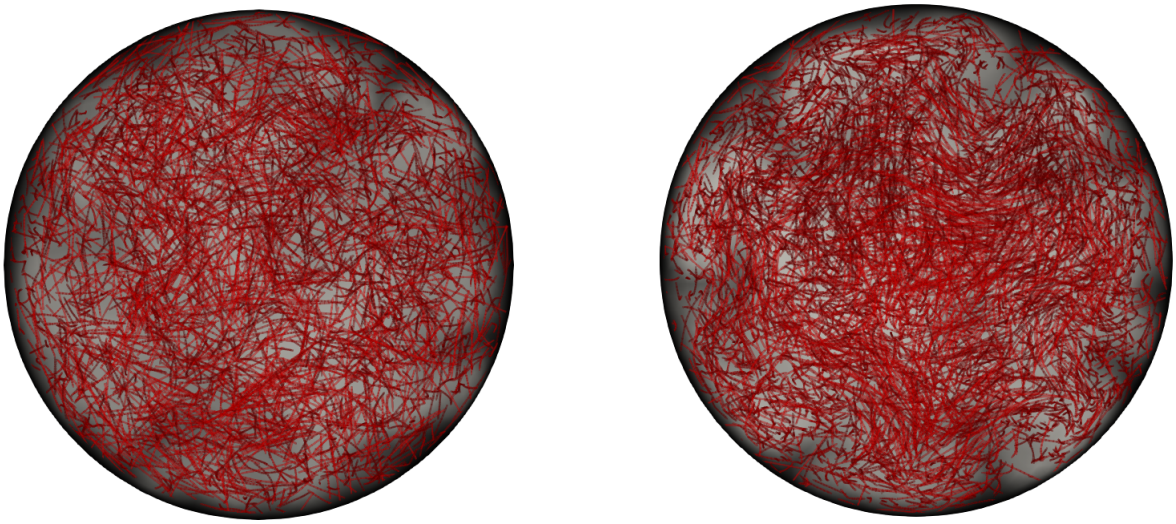

(a) 2D projected fiber conformation for $c_v = 0.0025$

(b) 2D projected fiber confirmation for $c_v = 0.005$

Figure 7.12: Fiber conformation, fibers shown in red. Contours of Instantaneous velocity in grayscale.

7.4 Conclusion

In this chapter preliminary results on the effect of fibrous additives in turbulent pipe flow for $Re = 6000$ have been presented. The obtained results are in reasonable agreement with previous theoretical and numerical studies on drag reduction by particle laden flows. Due to the heavy time requirement of the simulations, complete physical analysis on the mechanism of drag reduction has not been performed as the higher order statistics such as $\langle u_i' u_j' \rangle$ and $\langle u_i' u_j' u_k' \rangle$ did not reach a fully statistically stationary state. However, these components are necessary to understand the energy budget and stress budget of the drag reduced flows. Future work would include these results.

CHAPTER 8

CONCLUSION AND PERSPECTIVES

Conclusion

This thesis was primary concerned with the numerical modeling of high aspect ratio flexible fibers in inertial flows. The fibers were modeled as discrete beam segments that can twist, bend and rotate. The equations of the fiber motion were solved using an open source discrete element solver YADE [174]. The three dimensional incompressible Navier-Stokes equations governing the fluid motion were solved based on a node centered finite volume solver YALES2 [117]. The coupling between the phases were obtained by means of a pseudo immersed boundary method as the hydrodynamic interaction between the phases were calculated using analytical expressions from the literature. A 'per unit length' hydrodynamic torque model for the fibers was derived from explicit numerical simulations of shear flow past a high aspect ratio cylinder. For Reynolds numbers at the inertial regime ($10^{-2} \leq Re < 10^2$, Re at the fiber scale), non linear drag force formulations [164, 109, 163] for flow past an infinite cylinder was used. For rigid fibers in creeping flow, the drag force formulation from the slender body theory [12] was used.
The developed model was validated against several experimental studies and analytical theories ranging from the creeping flow regime (for rigid fibers) to inertial regimes. In the creeping flow regime, numerical simulations of semi dilute rigid fiber suspensions in shear were performed. The developed model was able to capture the fiber-fiber hydrodynamic and non-hydrodynamic interactions. The numerically obtained fiber microstructure and rheological properties were in reasonable agreement with previous experimental observations and analytical theories [160, 16, 146, 70]. The elasto-hydrodynamic interactions at finite Reynolds was validated with against two test cases. In the first test case, the deflection of the free end of a fiber in an uniform flow field was obtained numerically and the results were compared with the experiment of Tritton [168]. In the second test case the conformation of long flexible fibers in homogeneous isotropic turbulence was obtained numerically and the results were compared with the experiments of Brouzet *et al.* [28] as well as Verhille and Bartoli [172]. Two numerical studies were performed to verify the effects of the suspended fibers on carrier phase turbulence. Turbulence modulations by 1% concentration fiber suspension (by volume) were observed in turbulent channel flow at $Re = 2000$ and it was observed that the laminar velocity profile of the flow was altered to a blunt velocity bearing resemblance to the 1/7 power law profile. At $Re = 6000$ a mixed turbulent flow was observed. The numerical results were validated against the experimental work of Xu and Aidun [182]. Preliminary results of the drag reducing effects of semi dilute fiber suspensions in turbulent pipe were obtained. Two fiber volume concentrations were considered and the obtained results such as reduction in the wall shear stress, increased turbulence intensity in the streamwise direction agreed qualitatively with previous studies [122, 92, 171]. However, the results are not

conclusive as more analysis on the drag reduction mechanism needs to be performed.

Future Works

Model Improvements

One of the major issues in the present work is the numerical noise induced by the fiber segments onto the fluid grid. The interpolation of the velocity (translational and rotational) and forces between the fiber segments and the fluid grid can be improved by using a Gaussian envelope so as to have a better interpolation of the fluid velocity around the fiber segment interface [10] (and the segment hydrodynamic force interpolation back to the fluid grid). Another approach would be to utilize the force coupling method (FCM) [175, 114], as this method provides nearly exact description of the hydrodynamic force on the particles at low finite particle Reynolds numbers. However the existing FCM may need to be modified to take into account of the fiber shape and flexibility. Implementation of Immersed Boundary Method (IBM) with the direct forcing approach [169] in the present numerical model is quite straightforward. However, such an implementation would require additional Lagrangian points around the circumference of the fiber segment and the computational cost for simulating long fibers would be significantly expensive compared to the present model (Prosperetti [132] gives an interesting commentary on the fully resolved IB methods and the computational cost). The IB method explicitly enforces the no slip boundary condition over the fiber resulting in a very accurate coupling between the flow and the fiber. Figure 8.10 shows the streamlines around a rigid fiber at finite Reynolds number the IB method of Uhlmann was used.

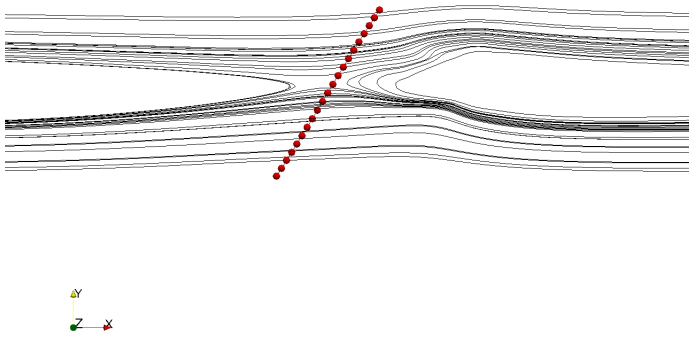

Figure 8.1: Streamlines past fiber (in red) in shear at finite Reynolds number obtained by immersed boundary method of Uhlmann [169].

Physical modeling

In terms of understanding new physics, the developed model could be used to understand the rheology of concentrated rigid fiber suspensions. From the experiments of Snook *et al.* [156] and Bounoua *et al.* [17], a negative second normal stress difference was observed. These experimental results are in qualitative agreement and perhaps numerical simulations of rigid fiber suspensions could provide some insight on the origin of the negative second normal stress difference. More

physics can be included between the fiber-fiber interactions, this would include for instance implementing van der Waals force model between the fibers, colloidal forces and Brownian motion. Such interactions dictate the rheology and microstructure formation in high aspect ratio cellulose nano fiber suspensions as shown in the experimental studies of Martoïa *et al.* [110, 111].
The dynamics of flexible fibers in isotropic turbulent flows can be used to study the very nature of turbulent flows as shown in the experimental studies of Brouzet *et al.* [28], [172]. In a recent numerical study, Rosti *et al.* [139] correlated the deformation of flexible fibers in homogeneous isotropic turbulent (HIT) flows to the second-order velocity structure function and showed that reasonable prediction of the flow field could be obtained by studying the fiber deformation. The developed model could be used to study similar phenomena.

Résumé

Un modèle numérique décrivant le comportement de fibres flexibles transportées par un écoulement a été développé. Ce modèle s'appuie sur le couplage du code "open-source" YADE, basé sur une méthode d'éléments discrets pour la prédiction du comportement mécanique des fibres, avec le code communautaire YALES2 pour la prédiction de l'écoulement. Chaque fibre est discrétisée en plusieurs segments, ce qui leur permet de se plier, de se vriller et de se tourner. Les équations du mouvement des fibres sont résolues en utilisant des schémas explicites du second ordre en temps et en espace. Pour l'écoulement, les équations de Navier-Stokes incompressibles sont résolues à partir d'une discrétisation volumes finis d'ordre 4 en temps et en espace.
La figure 8.2 illustre la géométrie et la discrétisation d'une fibre. La fibre est composée de plusieurs segments $\{b_1, b_2, b_3, ..., b_n\}$ et $\{c_1, c_2, c_3, ..., c_{n+1}\}$ sont les nœuds de ces segments.

$\{\vec{O}_1, \vec{O}_2, \vec{O}_3, ..., \vec{O}_{n+1}\}$ sont les vecteurs positions de ces nœuds et $\vec{Z}e$ est le vecteur "bord à bord" de la fibre. Les vecteurs (e_x, e_y, e_z) forment une base ortho-normée qui est fixée au segment considéré et $\vec{p}$ est le vecteur orientation de ce segment.

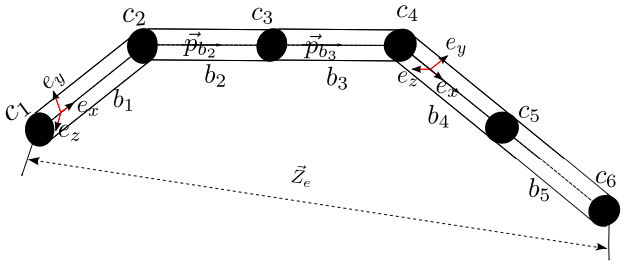

Figure 8.2: Géométrie d'une fibre

Le couplage entre la phase composée des fibres et la phase fluide est obtenu par une méthode type "frontière immergée", où les forces hydrodynamiques qui s'appliquent sur les segments des fibres sont calculées à partir de différentes expressions analytiques. La figure 8.3 schématise le

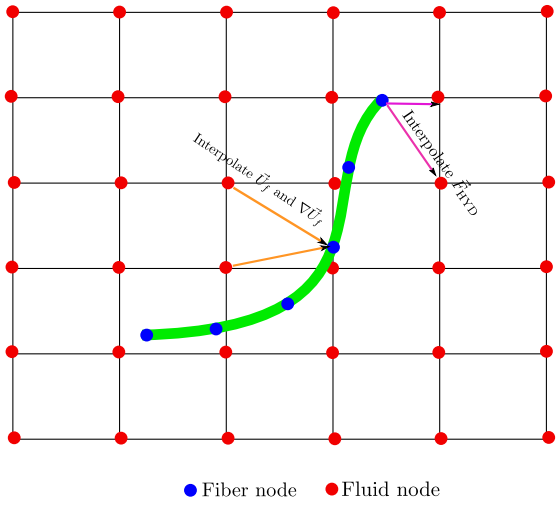

Figure 8.3: Représentation graphique du couplage. La fibre est représentée en vert, les nœuds des fibres sont en bleu, les nœuds du maillage fluide sont en rouge.

couplage utilisé dans cette étude. Le vecteur vitesse et le tenseur des gradients de vitesse calculés sur les nœuds du maillage fluide à proximité des segments des fibres sont interpolés sur la fibre et des modèles analytiques et/ou empiriques sont utilisés pour déterminer la force hydrodynamique s'appliquant sur les segments des fibres. Différents modèles de force hydrodynamique ont été

analysés et leurs limitations ont été déterminées. Pour un nombre de Reynolds, basé sur l'échelle de la fibre, situé dans le régime inertiel ($(10^{-2} \leq Re \leq 10^{2})$, une formulation non-linéaire de la force de trainée basée sur les résultats d'un écoulement autour d'un cylindre infini oblique est utilisée. La figure 8.4 compare les composantes des modèles de forces hydrodynamiques utilisés avec des résultats de simulations explicites d'écoulements autour d'un cylindre infini.

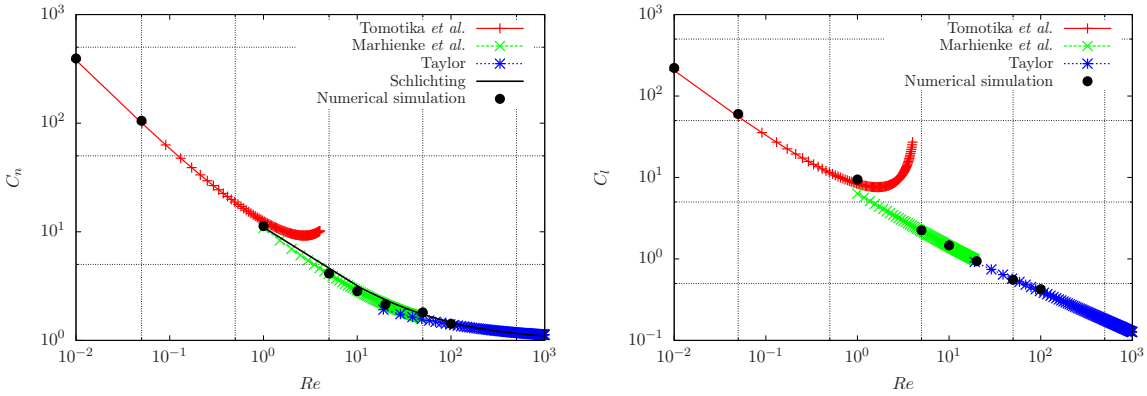

(a) C_n vs. Re (b) C_l vs. Re

Figure 8.4: Coefficients de la force hydrodynamique en fonction du nombre de Reynolds. "Numerical simulation" fait référence aux simulations explicites d'écoulements autour d'un cylindre infini.

Dans le cas de fibres rigides dans un écoulement de Stokes, la formulation de la force de trainée utilisée est celle issue de la théorie "slender body". Un modèle de couple hydrodynamique par unité de longueur de fibre a été dérivé à partir de simulations numériques explicites d'un cylindre à grand rapport d'aspect placé dans un écoulement cisaillé. Le modèle ainsi développé a été validé en le confrontant à différentes études expérimentales et résultats analytiques allant des écoulements de Stokes (pour des fibres rigides) à des régimes inertiels. Pour les écoulements de Stokes, des simulations numériques de suspension de fibres rigides dans un écoulement cisaillé ont été réalisées. Le modèle développé est capable de prédire les interactions entre fibres. Les résultats numériques obtenus sur la microstructure des fibres et les propriétés rhéologiques sont en accord avec les observations expérimentales précédentes et les théories analytiques [160, 16, 146, 70], comme l'illustre la figure 8.5.

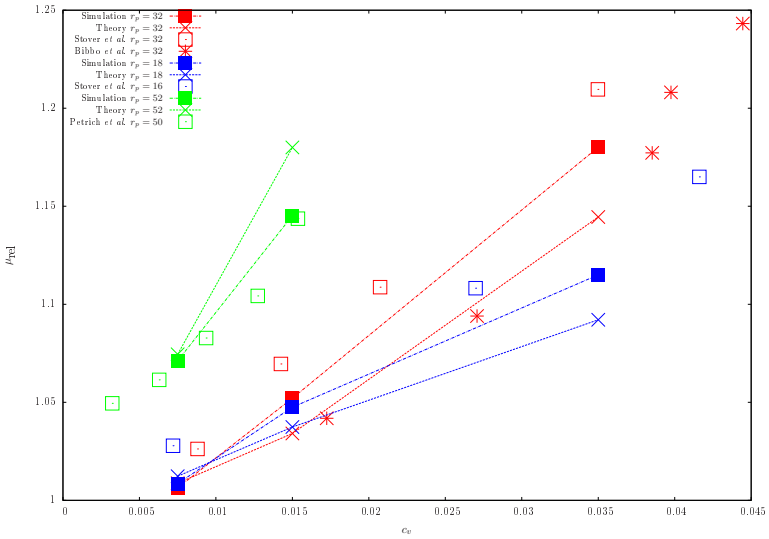

Figure 8.5: Comparaison de la viscosité effective, μ_{rel}, évaluée à partir des simulations numériques et de résultats expérimentaux ou théoriques pour différents rapports d'aspect des fibres.

Les interactions elasto-hydrodynamiques ont été validées à partir de deux cas tests. Dans le premier cas test, la déviation d'une fibre fixée à un bord et libre de l'autre dans un écoulement uniforme a été simulée et comparée aux résultats expérimentaux de Tritton [168]. La figure 8.6 montre cette comparaison entre le modèle développé dans ce travail, les résultats expérimentaux, mais également entre un modèle de force précédemment proposé (*prolate-spheroid model*) et un résultat analytique.

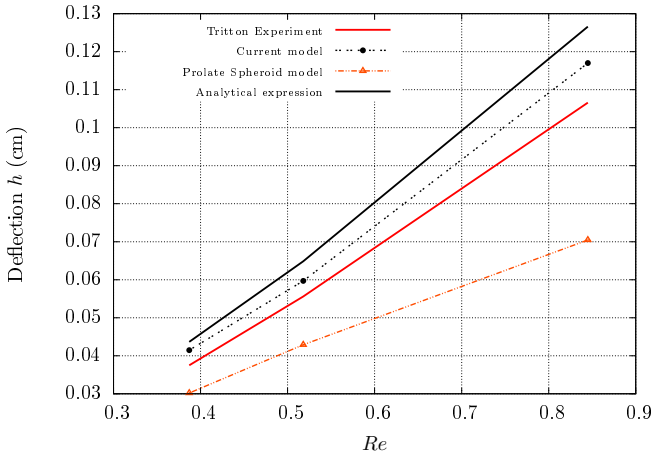

Figure 8.6: Comparaison de la déviation h issue de résultats expérimentaux, numériques (*prolate-spheroid model* et le modèle développé dans ce travail) et analytiques.

Le second cas test considéré consiste à prédire le comportement de fibres flexibles dans une turbulence homogène et isotrope. Les résultats sont comparés aux résultats expérimentaux de Brouzet *et al.* [28] et Verhille et Bartoli [172]. A titre d'illustration, la figure 8.7 compare la densité de probabilité (PDF) de la norme du vecteur "bord-à-bord" obtenu numériquement, à celle mesuré expérimentalement par Brouzet *et al.* [28].

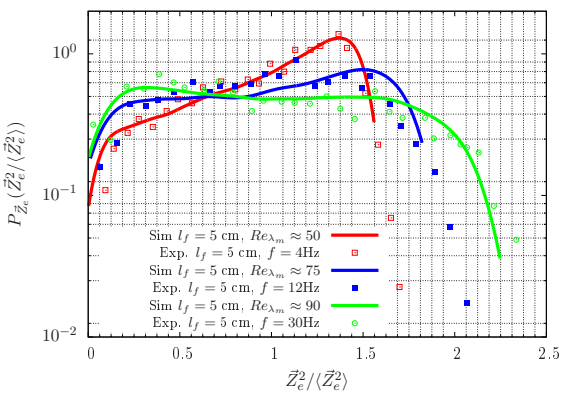

(a) PDF de $\vec{Z}_e^2/\langle\vec{Z}_e^2\rangle$ pour une longueur de fibre $l_f =$ 5cm.

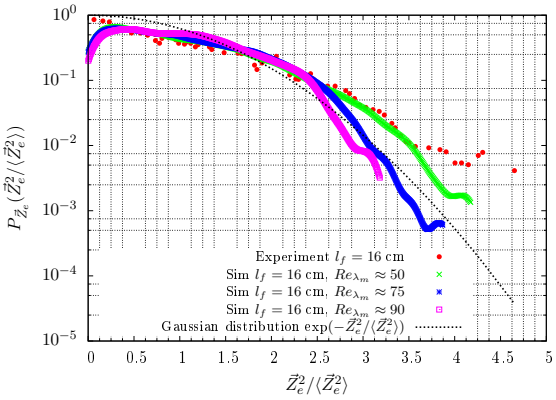

(b) PDF de $\vec{Z}_e^2/\langle\vec{Z}_e^2\rangle$ pour une longueur de fibre $l_f =$ 16cm.

Figure 8.7: PDF de la norme du vecteur "bord-à-bord" pour des fibres flexibles dans une turbulence homogène et isotrope.

Deux autres études numériques ont été menées pour mesurer les effets des fibres en suspension sur l'écoulement turbulent porteur. La modulation de la turbulence par une suspension de fibres (concentration de 1% en volume) a été observée dans un canal turbulent à un nombre de Reynolds $Re = 2000$. Ainsi, le profil de vitesse initialement laminaire est modifié en un profil plus plat ressemblant à un profil plus turbulent. Les résultats numériques ont été validés par comparaison aux travaux expérimentaux de Xu and Aidun [182]. La figure 8.8 montre la comparaison des profils de vitesse pour le régime turbulent, $Re = 6000$.

Figure 8.8: Comparaison des profils de vitesse entre une configuration sans fibre et une configuration avec une suspension de fibres (concentration de 1% en volume) à $Re = 6000$.

Des résultats préliminaires des effets de réduction de trainée d'une suspension de fibres dans un écoulement turbulent dans une conduite ont finalement été obtenus. Deux concentrations de fibres différentes ont été considérées et les résultats obtenus sur la réduction du cisaillement pariétal et l'augmentation de l'intensité turbulente dans la direction de l'écoulement sont en accord avec les précédentes études [122, 92, 171]. Les profils de vitesse (figure 8.9) sont en accord avec les résultats observés dans de précédentes études et indiquent un effet de réduction de trainée due aux fibres. La réduction de trainée évaluée à partir de la vitesse de frottement u_τ est de 7.75% pour la concentration $c_v = 0.0025$ et de 12.8% pour $c_v = 0.005$. Cependant, une étude plus approfondie des mécanismes de réduction de trainée doit être menée.

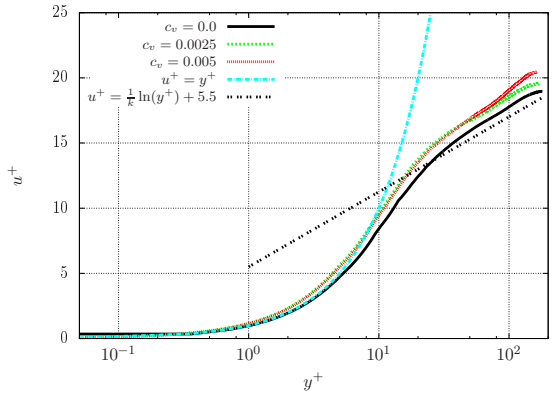

Figure 8.9: Comparaison des profils de vitesse moyenne (en unité de parois) entre un écoulement sans et avec fibres.

Perspectives

Développement du modèle

Une amélioration nécessaire à l'actuelle implémentation est de réduire le bruit numérique induit par les segments des fibres sur le maillage fluide. Une enveloppe Gaussienne peut être utilisée de façon à avoir une meilleure interpolation de la vitesse du fluide autour des fibres [10], ainsi qu'une meilleure interpolation des forces hydrodynamiques sur le maillage fluide. Une autre approche serait d'utiliser la méthode "force coupling" (FC) [175, 114], qui permet une description quasi-exacte de la force hydrodynamique sur les particules à bas nombre de Reynolds particulaire. Cependant, la méthode FC existante nécessite une adaptation pour prendre en compte la forme des fibres et leur flexibilité. L'implémentation d'une méthode de frontières immergées (IB) avec une approche de forçage direct [169] est quasi immédiate dans la méthode actuelle. La méthode IB force explicitement la condition de non-glissement sur des fibres, permettant un couplage très précis entre les fibres et le fluide. La figure 8.10 montre les lignes de courant autour d'une fibre rigide calculée à partir d'une méthode IB. Cependant, une telle implémentation nécessite des points Lagrangiens supplémentaires autour des segments de fibres et le coût des simulations pour des fibres longues serait sensiblement augmenté par rapport au modèle actuel (Prosperetti [132] commente le coût computationnel d'une approche entièrement résolue par méthode IB).

Analyse physique

En terme d'analyse physique, le modèle développé pourrait être utilisé pour comprendre la rhéologie de suspension de fibres rigides. En effet, dans les expériences de Snook *et al.* [156] et Bounoua *et al.* [17], une différence de tension normale négative est observée. Ces expériences sont cohérentes entre elles et peut-être que des simulations numériques de suspension de fibres rigides pourraient apporter un éclairage supplémentaire sur l'origine de cette différence. Plus de physique pourrait être prise en compte dans les interactions entre fibres. Cela pourrait inclure un modèle de force de van der Waals entre les fibres, les forces colloïdales et des mouvements Browniens. De telles interactions contrôlent la rhéologie et la formation de microstructures dans les suspensions de nano fibres de celluloses à fort rapport d'aspect, comme l'ont montré les expériences de Martoïa *et al.* [110, 111].
La dynamique de fibres flexibles en turbulence homogène isotrope peut être utilisée pour l'étude fondamentale de la turbulence, comme cela a été montré par les études expérimentales de Brouzet *et al.* [28], [172]. Dans une étude numérique récente, Rosti *et al.* [139] rapprochait la déformation de fibres flexibles dans une turbulence homogène isotrope à la fonction de structure du second ordre de la vitesse. Une prédiction raisonnable de l'écoulement peut être obtenue en étudiant la

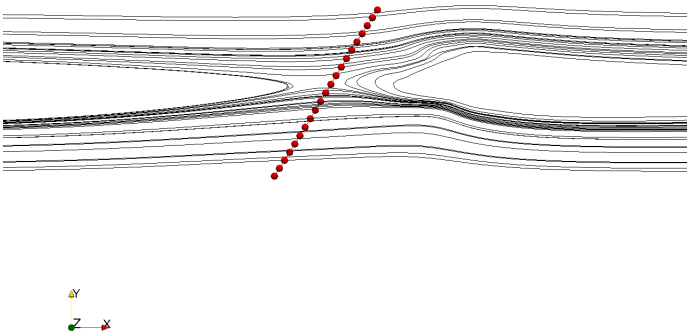

Figure 8.10: Lignes de courant autour d'une fibre (en rouge) dans un écoulement cisaillé. Résultat obtenu à partir d'une simulation utilisant une méthode IB [169].

déformation des fibres. Le modèle développé pourrait être utilisé pour des études similaires.

BIBLIOGRAPHY

[1] S. G. Advani and C. L. Tucker III. Closure approximations for three-dimensional structure tensors. *Journal of Rheology*, 34(3):367–386, 1990.

[2] C. K. Aidun and J. R. Clausen. Lattice-boltzmann method for complex flows. *Annual review of fluid mechanics*, 42:439–472, 2010.

[3] E. Anczurowski, R. Cox, and S. Mason. The kinetics of flowing dispersions: Iv. transient orientations of cylinders. *Journal of Colloid and Interface Science*, 23(4):547–562, 1967.

[4] E. Anczurowski and S. Mason. The kinetics of flowing dispersions: Iii. equilibrium orientations of rods and discs (experimental). *Journal of Colloid and Interface Science*, 23(4):533–546, 1967.

[5] J. Andrić, S. Lindström, S. Sasic, and H. Nilsson. Ballistic deflection of fibres in decelerating flow. *International Journal of Multiphase Flow*, 2016.

[6] J. Andrić, S. B. Lindström, S. Sasic, and H. Nilsson. Rheological properties of dilute suspensions of rigid and flexible fibers. *Journal of Non-Newtonian Fluid Mechanics*, 212:36–46, 2014.

[7] J. S. Andrić, S. B. Lindström, S. M. Sasic, and H. Nilsson. Particle-level simulations of flocculation in a fiber suspension flowing through a diffuser. *Thermal Science*, (00):185–185, 2016.

[8] M. N. Ardekani, P. Costa, W. P. Breugem, and L. Brandt. Numerical study of the sedimentation of spheroidal particles. *International Journal of Multiphase Flow*, 87(Supplement C):16 – 34, 2016.

[9] M. N. Ardekani, P. Costa, W.-P. Breugem, F. Picano, and L. Brandt. Drag reduction in turbulent channel flow laden with finite-size oblate spheroids. *Journal of Fluid Mechanics*, 816:43–70, 2017.

[10] S. Balachandar. A scaling analysis for point–particle approaches to turbulent multiphase flows. *International Journal of Multiphase Flow*, 35(9):801–810, 2009.

[11] S. Balachandar and J. K. Eaton. Turbulent dispersed multiphase flow. *Annual Review of Fluid Mechanics*, 42:111–133, 2010.

[12] G. Batchelor. Slender-body theory for particles of arbitrary cross-section in stokes flow. *Journal of Fluid Mechanics*, 44(03):419–440, 1970.

[13] G. Batchelor. The stress generated in a non-dilute suspension of elongated particles by pure straining motion. *Journal of Fluid Mechanics*, 46(4):813–829, 1971.

[14] G. Batchelor and J.-T. Green. The hydrodynamic interaction of two small freely-moving spheres in a linear flow field. *Journal of Fluid Mechanics*, 56(2):375–400, 1972.

[15] M. A. Bibbó. *Rheology of semiconcentrated fiber suspensions*. PhD thesis, Massachusetts Institute of Technology, 1987.

[16] M. A. Bibbo, S. M. Dinh, and R. C. Armstrong. Shear flow properties of semiconcentrated fiber suspensions. *Journal of Rheology*, 29(6):905–929, 1985.

[17] S. Bounoua, P. Kuzhir, and E. Lemaire. Normal stress differences in non-brownian fiber suspensions. *Journal of rheology*, 60(4):661–671, 2016.

[18] F. Bourrier, F. Kneib, B. Chareyre, and T. Fourcaud. Discrete modeling of granular soils reinforcement by plant roots. *Ecological engineering*, 61:646–657, 2013.

[19] J. F. Brady. The rheological behavior of concentrated colloidal dispersions. *The Journal of Chemical Physics*, 99(1):567–581, 1993.

[20] J. F. Brady and G. Bossis. Stokesian dynamics. *Annual review of fluid mechanics*, 20(1):111–157, 1988.

[21] H. Brenner. The oseen resistance of a particle of arbitrary shape. *Journal of Fluid Mechanics*, 11(4):604–610, 1961.

[22] H. Brenner. The stokes resistance of an arbitrary particle. *Chemical Engineering Science*, 18(1):1–25, 1963.

[23] H. Brenner. Rheology of a dilute suspension of axisymmetric brownian particles. *International Journal of Multiphase Flow*, 1(2):195–341, 1974.

[24] F. P. Bretherton. The motion of rigid particles in a shear flow at low reynolds number. *Journal of Fluid Mechanics*, 14(02):284–304, 1962.

[25] W.-P. Breugem. A second-order accurate immersed boundary method for fully resolved simulations of particle-laden flows. *Journal of Computational Physics*, 231(13):4469–4498, 2012.

[26] S. Broersma. Rotational diffusion constant of a cylindrical particle. *The Journal of Chemical Physics*, 32(6):1626–1631, 1960.

[27] S. Broersma. Viscous force constant for a closed cylinder. *The Journal of Chemical Physics*, 32(6):1632–1635, 1960.

[28] C. Brouzet, G. Verhille, and P. Le Gal. Flexible fiber in a turbulent flow: A macroscopic polymer. *Physical review letters*, 112(7):074501, 2014.

[29] G. L. Brown and A. Roshko. On density effects and large structure in turbulent mixing layers. *Journal of Fluid Mechanics*, 64(4):775–816, 1974.

[30] J. Burgers. Second report on viscosity and plasticity. *Nordemann, New York*, page 113, 1938.

[31] J. E. Butler and B. Snook. Microstructural dynamics and rheology of suspensions of rigid fibers. *Annual Review of Fluid Mechanics*, (0), 2018.

[32] E. Catalano. *A pore–scale coupled hydromechanical model for biphasic granular media. Application to granular sediment hydrodynamics*. PhD thesis, PhD thesis, Université de Grenoble, 2012.

[33] N. R. Challabotla, L. Zhao, and H. I. Andersson. On fiber behavior in turbulent vertical channel flow. *Chemical Engineering Science*, 153:75–86, 2016.

[34] B. Chareyre and P. Villard. Dynamic spar elements and discrete element methods in two dimensions for the modeling of soil-inclusion problems. *Journal of engineering mechanics*, 131:689, 2005.

[35] A. J. Chorin. Numerical solution of the navier-stokes equations. *Mathematics of computation*, 22(104):745–762, 1968.

[36] D. H. Chung and T. H. Kwon. Improved model of orthotropic closure approximation for flow induced fiber orientation. *Polymer composites*, 22(5):636–649, 2001.

[37] I. L. Claeys and J. F. Brady. Suspensions of prolate spheroids in stokes flow. part 1. dynamics of a finite number of particles in an unbounded fluid. *Journal of Fluid Mechanics*, 251:411–442, 1993.

[38] I. L. Claeys and J. F. Brady. Suspensions of prolate spheroids in stokes flow. part 2. statistically homogeneous dispersions. *Journal of Fluid Mechanics*, 251:443–477, 1993.

[39] R. Clift, J. R. Grace, and M. E. Weber. *Bubbles, drops, and particles*. Courier Corporation, 2005.

[40] E. Climent and M. R. . The force coupling method: a flexible approach for the simulation of particulate flows. 2009.

[41] R. Cox. The motion of long slender bodies in a viscous fluid part 1. general theory. *Journal of Fluid mechanics*, 44(04):791–810, 1970.

[42] R. Crowson and M. Folkes. Rheology of short glass fiber-reinforced thermoplastics and its application to injection molding. ii. the effect of material parameters. *Polymer Engineering & Science*, 20(14):934–940, 1980.

[43] R. Crowson, M. Folkes, and P. Bright. Rheology of short glass fiber-reinforced thermoplastics and its application to injection molding i. fiber motion and viscosity measurement. *Polymer Engineering & Science*, 20(14):925–933, 1980.

[44] B. Delmotte, E. Climent, and F. Plouraboué. A general formulation of bead models applied to flexible fibers and active filaments at low reynolds number. *Journal of Computational Physics*, 286:14–37, 2015.

[45] B. Delmotte, E. E. Keaveny, E. Climent, and F. Plouraboué. Simulations of brownian tracer transport in squirmer suspensions. *arXiv preprint arXiv:1711.01442*, 2017.

[46] B. Delmotte, E. E. Keaveny, F. Plouraboué, and E. Climent. Large-scale simulation of steady and time-dependent active suspensions with the force-coupling method. *Journal of Computational Physics*, 302(Supplement C):524 – 547, 2015.

[47] M. Do-Quang, G. Amberg, G. Brethouwer, and A. V. Johansson. Simulation of finite-size fibers in turbulent channel flows. *Physical Review E*, 89(1):013006, 2014.

[48] S. Dong, D. Liu, M. R. Maxey, and G. E. Karniadakis. Spectral distributed lagrange multiplier method: algorithm and benchmark tests. *Journal of Computational Physics*, 195(2):695–717, 2004.

[49] Y. Dubief, C. M. White, V. E. Terrapon, E. S. Shaqfeh, P. Moin, and S. K. Lele. On the coherent drag-reducing and turbulence-enhancing behaviour of polymers in wall flows. *Journal of Fluid Mechanics*, 514:271–280, 2004.

[50] A. Dufresne. *Nanocellulose: from nature to high performance tailored materials*. Walter de Gruyter GmbH & Co KG, 2017.

[51] P. Dumont, J.-P. Vassal, L. Orgéas, V. Michaud, D. Favier, and J.-A. E. Månson. Processing, characterisation and rheology of transparent concentrated fibre-bundle suspensions. *Rheologica acta*, 46(5):639–651, 2007.

[52] J. K. Eaton. Two-way coupled turbulence simulations of gas-particle flows using point-particle tracking. *International Journal of Multiphase Flow*, 35(9):792–800, 2009.

[53] A. Effeindzourou, B. Chareyre, K. Thoeni, A. Giacomini, and F. Kneib. Modelling of deformable structures in the general framework of the discrete element method. *Geotextiles and Geomembranes*, 44(2):143–156, 2016.

[54] J. Eggels, F. Unger, M. Weiss, J. Westerweel, R. Adrian, R. Friedrich, and F. Nieuwstadt. Fully developed turbulent pipe flow: a comparison between direct numerical simulation and experiment. *Journal of Fluid Mechanics*, 268:175–210, 1994.

[55] J. Einarsson, F. Candelier, F. Lundell, J. Angilella, and B. Mehlig. Rotation of a spheroid in a simple shear at small reynolds number. *Physics of Fluids*, 27(6):063301, 2015.

[56] A. Einstein. Über die von der molekularkinetischen theorie der wärme geforderte bewegung von in ruhenden flüssigkeiten suspendierten teilchen. *Annalen der physik*, 322(8):549–560, 1905.

[57] H. Faxén. Der widerstand gegen die bewegung einer starren kugel in einer zähen flüssigkeit, die zwischen zwei parallelen ebenen wänden eingeschlossen ist. *Annalen der Physik*, 373(10):89–119, 1922.

[58] O. Forgacs and S. Mason. Particle motions in sheared suspensions: Ix. spin and deformation of threadlike particles. *Journal of colloid science*, 14(5):457–472, 1959.

[59] N. Frankel and A. Acrivos. The constitutive equation for a dilute emulsion. *Journal of Fluid Mechanics*, 44(01):65–78, 1970.

[60] G. H. Ganser. A rational approach to drag prediction of spherical and nonspherical particles. *Powder Technology*, 77(2):143–152, 1993.

[61] M. Germano, U. Piomelli, P. Moin, and W. H. Cabot. A dynamic subgrid-scale eddy viscosity model. *Physics of Fluids A: Fluid Dynamics*, 3(7):1760–1765, 1991.

[62] R. Glowinski, T.-W. Pan, T. I. Hesla, and D. D. Joseph. A distributed lagrange multiplier/fictitious domain method for particulate flows. *International Journal of Multiphase Flow*, 25(5):755–794, 1999.

[63] H. Goldsmith and S. Mason. The microrheology of dispersions. In *Rheology, Volume 4*, pages 85–250. Elsevier, 1967.

[64] E. Guazzelli and J. F. Morris. A physical introduction to suspension dynamics, 2011.

[65] J. Hämäläinen, S. B. Lindström, T. Hämäläinen, and H. Niskanen. Papermaking fibre-suspension flow simulations at multiple scales. *Journal of Engineering Mathematics*, 71(1):55–79, 2011.

[66] J. Happel and H. Brenner. *Low Reynolds number hydrodynamics: with special applications to particulate media*, volume 1. Springer Science & Business Media, 2012.

[67] A. Hölzer and M. Sommerfeld. New simple correlation formula for the drag coefficient of non-spherical particles. *Powder Technology*, 184(3):361–365, 2008.

[68] A. Hölzer and M. Sommerfeld. Lattice boltzmann simulations to determine drag, lift and torque acting on non-spherical particles. *Computers & Fluids*, 38(3):572–589, 2009.

[69] R. A. Hosn, L. Sibille, N. Benahmed, and B. Chareyre. Discrete numerical modeling of loose soil with spherical particles and interparticle rolling friction. *Granular Matter*, 19(1):4, 2017.

[70] G. B. Jeffery. The motion of ellipsoidal particles immersed in a viscous fluid. In *Proceedings of the Royal Society of London A: Mathematical, Physical and Engineering Sciences*, volume 102, pages 161–179. The Royal Society, 1922.

[71] R. E. Johnson. An improved slender-body theory for stokes flow. *J. Fluid Mech*, 99(02):411–431, 1980.

[72] C. Joung, N. Phan-Thien, and X. Fan. Direct simulation of flexible fibers. *Journal of non-newtonian fluid mechanics*, 99(1):1–36, 2001.

[73] M. Junk and R. Illner. A new derivation of jeffery's equation. *Journal of Mathematical Fluid Mechanics*, 9(4):455–488, 2007.

[74] S. Kaplun. Low reynolds number flow past a circular cylinder. *Journal of Mathematics and Mechanics*, pages 595–603, 1957.

[75] S. Kaplun and P. Lagerstrom. Asymptotic expansions of navier-stokes solutions for small reynolds numbers. *Journal of Mathematics and Mechanics*, pages 585–593, 1957.

[76] G. Karypis and V. Kumar. A fast and high quality multilevel scheme for partitioning irregular graphs. *SIAM Journal on scientific Computing*, 20(1):359–392, 1998.

[77] J. B. Keller and S. I. Rubinow. Slender-body theory for slow viscous flow. *J. Fluid Mech*, 75(4):705–714, 1976.

[78] R. Kerekes and R. Garner. Measurement of turbulence in pulp suspensions by laser anemometry. *PULP & PAPER-CANADA*, 83(9):TR53–TR59, 1982.

[79] R. Khayat and R. Cox. Inertia effects on the motion of long slender bodies. *Journal of Fluid Mechanics*, 209:435–462, 1989.

[80] S. Kim and S. J. Karrila. *Microhydrodynamics: principles and selected applications*. Courier Corporation, 2013.

[81] C. Kloss, C. Goniva, A. Hager, S. Amberger, and S. Pirker. Models, algorithms and validation for opensource dem and cfd–dem. *Progress in Computational Fluid Dynamics, an International Journal*, 12(2-3):140–152, 2012.

[82] D. L. Koch. A model for orientational diffusion in fiber suspensions. *Physics of Fluids*, 7(8):2086–2088, 1995.

[83] M. Kraushaar. *Application of the compressible and low-Mach number approaches to Large-Eddy Simulation of turbulent flows in aero-engines*. PhD thesis, Institut National Polytechnique de Toulouse-INPT, 2011.

[84] A. Kumar and J. J. Higdon. Dynamics of the orientation behavior and its connection with rheology in sheared non-brownian suspensions of anisotropic dicolloidal particles. *Journal of Rheology*, 55(3):581–626, 2011.

[85] A. J. Ladd. Numerical simulations of particulate suspensions via a discretized boltzmann equation. part 1. theoretical foundation. *Journal of fluid mechanics*, 271:285–309, 1994.

[86] A. J. Ladd. Numerical simulations of particulate suspensions via a discretized boltzmann equation. part 2. numerical results. *Journal of fluid mechanics*, 271:311–339, 1994.

[87] O. A. Ladyzhenskaya. *The mathematical theory of viscous incompressible flow*, volume 12. Gordon & Breach New York, 1969.

[88] H. Lamb. *Hydrodynamics*. Cambridge university press, 1932.

[89] L. D. Landau and E. M. Lifshitz. *Fluid mechanics: Landau and Lifshitz: course of theoretical physics*, volume 6. Elsevier, 2013.

[90] E. Lauga and T. R. Powers. The hydrodynamics of swimming microorganisms. *Reports on Progress in Physics*, 72(9):096601, 2009.

[91] L. Leal and E. Hinch. The effect of weak brownian rotations on particles in shear flow. *Journal of Fluid Mechanics*, 46(4):685–703, 1971.

[92] P. F. Lee and G. G. Duffy. Relationships between velocity profiles and drag reduction in turbulent fiber suspension flow. *AIChE Journal*, 22(4):750–753, 1976.

[93] D. Leith. Drag on nonspherical objects. *Aerosol science and technology*, 6(2):153–161, 1987.

[94] L. Li, H. Manikantan, D. Saintillan, and S. E. Spagnolie. The sedimentation of flexible filaments. *arXiv preprint arXiv:1306.4692*, 2013.

[95] S. Lim, A. Ferent, X. S. Wang, and C. S. Peskin. Dynamics of a closed rod with twist and bend in fluid. *SIAM Journal on Scientific Computing*, 31(1):273–302, 2008.

[96] A. Lindner and M. Shelley. Elastic fibers in flows. *Fluid-Structure Interactions in Low-Reynolds-Number Flows*, page 168, 2015.

[97] S. B. Lindström and T. Uesaka. Simulation of the motion of flexible fibers in viscous fluid flow. *Physics of Fluids (1994-present)*, 19(11):113307, 2007.

[98] S. B. Lindström and T. Uesaka. Particle-level simulation of forming of the fiber network in papermaking. *International Journal of Engineering Science*, 46(9):858–876, 2008.

[99] S. B. Lindström and T. Uesaka. Simulation of semidilute suspensions of non-brownian fibers in shear flow. *The Journal of chemical physics*, 128(2):024901, 2008.

[100] S. B. Lindström and T. Uesaka. A numerical investigation of the rheology of sheared fiber suspensions. *Physics of fluids*, 21(8):083301, 2009.

[101] V. Loisel, M. Abbas, O. Masbernat, and E. Climent. The effect of neutrally buoyant finite-size particles on channel flows in the laminar-turbulent transition regime. *Physics of Fluids (1994-present)*, 25(12):123304, 2013.

[102] S. Lomholt and M. R. Maxey. Force-coupling method for particulate two-phase flow: Stokes flow. *Journal of Computational Physics*, 184(2):381–405, 2003.

[103] D. Lopez and E. Guazzelli. Inertial effects on fibers settling in a vortical flow. *Physical Review Fluids*, 2(2):024306, 2017.

[104] E. Loth, G. Tryggvason, Y. Tsuji, S. Elghobashi, C. T. Crowe, A. Berlemont, M. Reeks, O. Simonin, T. Frank, Y. Onishi, et al. 13.1 overview of multiphase modeling. 2006.

[105] J. L. Lumley. Drag reduction by additives. *Annual review of fluid mechanics*, 1(1):367–384, 1969.

[106] F. Lundell, L. D. Söderberg, and P. H. Alfredsson. Fluid mechanics of papermaking. *Annual Review of Fluid Mechanics*, 43:195–217, 2011.

[107] M. Malandain, N. Maheu, and V. Moureau. Optimization of the deflated conjugate gradient algorithm for the solving of elliptic equations on massively parallel machines. *Journal of Computational Physics*, 238:32–47, 2013.

[108] C. Marchioli, M. Fantoni, and A. Soldati. Orientation, distribution, and deposition of elongated, inertial fibers in turbulent channel flow. *Physics of fluids*, 22(3):033301, 2010.

[109] N. Marheineke and R. Wegener. Modeling and application of a stochastic drag for fibers in turbulent flows. *International Journal of Multiphase Flow*, 37(2):136–148, 2011.

[110] F. Martoïa, P. Dumont, L. Orgéas, M. Belgacem, and J.-L. Putaux. Micro-mechanics of electrostatically stabilized suspensions of cellulose nanofibrils under steady state shear flow. *Soft Matter*, 12(6):1721–1735, 2016.

[111] F. Martoïa, C. Perge, P. Dumont, L. Orgéas, M. Fardin, S. Manneville, and M. Belgacem. Heterogeneous flow kinematics of cellulose nanofibril suspensions under shear. *Soft Matter*, 11(24):4742–4755, 2015.

[112] S. Mason and R. S. J. Manley. Particle motions in sheared suspensions: orientations and interactions of rigid rods. In *Proceedings of the Royal Society of London A: Mathematical, Physical and Engineering Sciences*, volume 238, pages 117–131. The Royal Society, 1956.

[113] M. Maxey. Simulation methods for particulate flows and concentrated suspensions. *Annual Review of Fluid Mechanics*, 49:171–193, 2017.

[114] M. Maxey and B. Patel. Localized force representations for particles sedimenting in stokes flow. *International journal of multiphase flow*, 27(9):1603–1626, 2001.

[115] Y. Morinishi, S. Tamano, and E. Nakamura. New scaling of turbulence statistics for incompressible thermal channel flow with different total heat flux gradients. *International journal of heat and mass transfer*, 50(9):1781–1789, 2007.

[116] R. D. Moser, J. Kim, and N. N. Mansour. Direct numerical simulation of turbulent channel flow up to re= 590. *Phys. Fluids*, 11(4):943–945, 1999.

[117] V. Moureau, P. Domingo, and L. Vervisch. Design of a massively parallel cfd code for complex geometries. *Comptes Rendus Mecanique*, 339(2):141–148, 2011.

[118] E. Nazockdast, A. Rahimian, D. Needleman, and M. Shelley. Cytoplasmic flows as signatures for the mechanics of mitotic positioning. *Molecular biology of the cell*, 28(23):3261–3270, 2017.

[119] C. Nilsen, H. I. Andersson, and L. Zhao. A voronoï analysis of preferential concentration in a vertical channel flow. *Physics of Fluids*, 25(11):115108, 2013.

[120] A. Oberbeck. Ueber stationäre flüssigkeitsbewegungen mit berücksichtigung der inneren reibung. *Journal für die reine und angewandte Mathematik*, 81:62–80, 1876.

[121] C. Oseen. Ueber die stokes' sche formel, und iiber eine venvandt. e aufgabe in der hydrodynamik. *Ark. Math. Astronom. Fys*, 6, 1910.

[122] J. Paschkewitz, Y. Dubief, C. D. Dimitropoulos, E. S. Shaqfeh, and P. Moin. Numerical simulation of turbulent drag reduction using rigid fibres. *Journal of Fluid Mechanics*, 518:281–317, 2004.

[123] J. Paschkewitz, Y. Dubief, and E. S. Shaqfeh. The dynamic mechanism for turbulent drag reduction using rigid fibers based on lagrangian conditional statistics. *Physics of Fluids*, 17(6):063102, 2005.

[124] N. A. Patankar, P. Singh, D. D. Joseph, R. Glowinski, and T.-W. Pan. A new formulation of the distributed lagrange multiplier/fictitious domain method for particulate flows. *International Journal of Multiphase Flow*, 26(9):1509–1524, 2000.

[125] T. Pedley and J. Kessler. Hydrodynamic phenomena in suspensions of swimming microorganisms. *Annual Review of Fluid Mechanics*, 24(1):313–358, 1992.

[126] C. S. Peskin. Flow patterns around heart valves: a digital computer method for solving the equations of motion. *IEEE Transactions on Biomedical Engineering*, (4):316–317, 1973.

[127] C. S. Peskin. The immersed boundary method. *Acta numerica*, 11:479–517, 2002.

[128] C. S. Peskin and D. M. McQueen. A three-dimensional computational method for blood flow in the heart i. immersed elastic fibers in a viscous incompressible fluid. *Journal of Computational Physics*, 81(2):372–405, 1989.

[129] M. P. Petrich, D. L. Koch, and C. Cohen. An experimental determination of the stress–microstructure relationship in semi-concentrated fiber suspensions. *Journal of non-newtonian fluid mechanics*, 95(2):101–133, 2000.

[130] T. R. Powers. Dynamics of filaments and membranes in a viscous fluid. *Reviews of Modern Physics*, 82(2):1607, 2010.

[131] C. Pozrikidis. *Boundary integral and singularity methods for linearized viscous flow*. Cambridge University Press, 1992.

[132] A. Prosperetti. Life and death by boundary conditions. *Journal of fluid mechanics*, 768:1–4, 2015.

[133] I. Proudman and J. Pearson. Expansions at small reynolds numbers for the flow past a sphere and a circular cylinder. *Journal of Fluid Mechanics*, 2(3):237–262, 1957.

[134] M. Rahnama, D. L. Koch, and E. S. Shaqfeh. The effect of hydrodynamic interactions on the orientation distribution in a fiber suspension subject to simple shear flow. *Physics of Fluids*, 7(3):487–506, 1995.

[135] A. Robertson. The flow characteristics of dilute fiber suspensions. *Tappi*, 40(5):326, 1957.

[136] A. M. Roma, C. S. Peskin, and M. J. Berger. An adaptive version of the immersed boundary method. *Journal of computational physics*, 153(2):509–534, 1999.

[137] C. Rosales and C. Meneveau. Linear forcing in numerical simulations of isotropic turbulence: Physical space implementations and convergence properties. *Physics of Fluids (1994-present)*, 17(9):095106, 2005.

[138] T. Rosén, Y. Kotsubo, C. K. Aidun, M. Do-Quang, and F. Lundell. Orientational dynamics of a triaxial ellipsoid in simple shear flow: Influence of inertia. *Phys. Rev. E*, 96:013109, Jul 2017.

[139] M. E. Rosti, A. A. Banaei, L. Brandt, and A. Mazzino. A flexible fiber reveals the secrets of turbulence. *arXiv preprint arXiv:1801.10194*, 2018.

[140] D. Saintillan, E. Darve, and E. S. Shaqfeh. A smooth particle-mesh ewald algorithm for stokes suspension simulations: The sedimentation of fibers. *Physics of Fluids*, 17(3):033301, 2005.

[141] A. Salahuddin, J. Wu, and C. Aidun. Numerical study of rotational diffusion in sheared semidilute fibre suspension. *Journal of Fluid Mechanics*, 692(1):153–182, 2012.

[142] A. Salinas and J. Pittman. Bending and breaking fibers in sheared suspensions. *Polymer Engineering & Science*, 21(1):23–31, 1981.

[143] H. Schlichting and K. Gersten. *Boundary-Layer Theory*. Springer, 2016.

[144] C. F. Schmid, L. H. Switzer, and D. J. Klingenberg. Simulations of fiber flocculation: Effects of fiber properties and interfiber friction. *Journal of Rheology (1978-present)*, 44(4):781–809, 2000.

[145] M. Shapiro and M. Goldenberg. Deposition of glass fiber particles from turbulent air flow in a pipe. *Journal of aerosol science*, 24(1):65–87, 1993.

[146] E. S. Shaqfeh and G. H. Fredrickson. The hydrodynamic stress in a suspension of rods. *Physics of Fluids A: Fluid Dynamics*, 2(1):7–24, 1990.

[147] M. Shin and D. L. Koch. Rotational and translational dispersion of fibres in isotropic turbulent flows. *Journal of Fluid Mechanics*, 540:143–173, 2005.

[148] M. Shin, D. L. Koch, and G. Subramanian. Structure and dynamics of dilute suspensions of finite-reynolds-number settling fibers. *Physics of Fluids*, 21(12):123304, 2009.

[149] A. J. Sierakowski and A. Prosperetti. Resolved-particle simulation by the physalis method: enhancements and new capabilities. *Journal of computational physics*, 309:164–184, 2016.

[150] A. Sierou and J. F. Brady. Accelerated stokesian dynamics simulations. *Journal of Fluid Mechanics*, 448:115–146, 2001.

[151] A. Sierou and J. F. Brady. Shear-induced self-diffusion in non-colloidal suspensions. *Journal of fluid mechanics*, 506:285–314, 2004.

[152] P. Singh, T. Hesla, and D. Joseph. Distributed lagrange multiplier method for particulate flows with collisions. *International Journal of Multiphase Flow*, 29(3):495–509, 2003.

[153] L. Skinner. Generalized expansions for slow flow past a cylinder. *The Quarterly Journal of Mechanics and Applied Mathematics*, 28(3):333–340, 1975.

[154] P. Skjetne, R. F. Ross, and D. J. Klingenberg. Simulation of single fiber dynamics. *The Journal of chemical physics*, 107(6):2108–2121, 1997.

[155] J. Smagorinsky. General circulation experiments with the primitive equations: I. the basic experiment. *Monthly weather review*, 91(3):99–164, 1963.

[156] B. Snook, L. M. Davidson, J. E. Butler, O. Pouliquen, and E. Guazzelli. Normal stress differences in suspensions of rigid fibres. *Journal of Fluid Mechanics*, 758:486–507, 2014.

[157] B. Snook, E. Guazzelli, and J. E. Butler. Vorticity alignment of rigid fibers in an oscillatory shear flow: Role of confinement. *Physics of Fluids*, 24(12):121702, 2012.

[158] J. M. Stockie and S. I. Green. Simulating the motion of flexible pulp fibres using the immersed boundary method. *Journal of Computational Physics*, 147(1):147–165, 1998.

[159] G. G. Stokes. *On the effect of the internal friction of fluids on the motion of pendulums*, volume 9. Pitt Press, 1851.

[160] C. A. Stover, D. L. Koch, and C. Cohen. Observations of fibre orientation in simple shear flow of semi-dilute suspensions. *Journal of Fluid Mechanics*, 238:277–296, 1992.

[161] R. Sundararajakumar and D. L. Koch. Structure and properties of sheared fiber suspensions with mechanical contacts. *Journal of Non-Newtonian Fluid Mechanics*, 73(3):205–239, 1997.

[162] J. W. Swan and J. F. Brady. Particle motion between parallel walls: Hydrodynamics and simulation. *Physics of Fluids*, 22(10):103301, 2010.

[163] G. Taylor. Analysis of the swimming of long and narrow animals. In *Proceedings of the Royal Society of London A: Mathematical, Physical and Engineering Sciences*, volume 214, pages 158–183. The Royal Society, 1952.

[164] S. Tomotika, T. Aoi, and H. Yosinobu. On the forces acting on a circular cylinder set obliquely in a uniform stream at low values of reynolds number. In *Proceedings of the Royal Society of London A: Mathematical, Physical and Engineering Sciences*, volume 219, pages 233–244. The Royal Society, 1953.

[165] A.-K. Tornberg and M. J. Shelley. Simulating the dynamics and interactions of flexible fibers in stokes flows. *Journal of Computational Physics*, 196(1):8–40, 2004.

[166] S. Tran-Cong, M. Gay, and E. E. Michaelides. Drag coefficients of irregularly shaped particles. *Powder Technology*, 139(1):21–32, 2004.

[167] B. Trevelyan and S. Mason. Particle motions in sheared suspensions. i. rotations. *Journal of Colloid Science*, 6(4):354–367, 1951.

[168] D. Tritton. Experiments on the flow past a circular cylinder at low reynolds numbers. *Journal of Fluid Mechanics*, 6(04):547–567, 1959.

[169] M. Uhlmann. An immersed boundary method with direct forcing for the simulation of particulate flows. *Journal of Computational Physics*, 209(2):448–476, 2005.

[170] S. Vantieghem. *Numerical simulations of quasi-static magnetohydrodynamics using an unstructured finite-volume solver: development and applications*. PhD thesis, Universitée Libre de Bruxelles, 2011.

[171] R. C. Vaseleski and A. Metzner. Drag reduction in the turbulent flow of fiber suspensions. *AIChE Journal*, 20(2):301–306, 1974.

[172] G. Verhille and A. Bartoli. 3d conformation of a flexible fiber in a turbulent flow. *Experiments in Fluids*, 57(7):1–10, 2016.

[173] F. Vermolen, K. Vuik, and G. Segal. *Deflation in Preconditioned Conjugate Gradient Methods for Finite Element Problems*, pages 103–129. Springer Berlin Heidelberg, Berlin, Heidelberg, 2004.

[174] V. Šmilauer et al. *Yade Documentation 2nd ed.* The Yade Project, 2015. http://yade-dem.org/doc/.

[175] G. Wang, M. Abbas, and E. Climent. Modulation of large-scale structures by neutrally buoyant and inertial finite-size particles in turbulent couette flow. *Physical Review Fluids*, 2(8):084302, 2017.

[176] F. M. White and I. Corfield. *Viscous fluid flow*, volume 3. McGraw-Hill New York, 2006.

[177] J. K. Wiens and J. M. Stockie. Simulating flexible fiber suspensions using a scalable immersed boundary algorithm. *Computer Methods in Applied Mechanics and Engineering*, 290:1–18, 2015.

[178] D. C. Wilcox et al. *Turbulence modeling for CFD*, volume 2. DCW industries La Canada, CA, 1998.

[179] C. Wu, O. Ayeni, A. Berrouk, and K. Nandakumar. Parallel algorithms for cfd–dem modeling of dense particulate flows. *Chemical Engineering Science*, 118:221–244, 2014.

[180] J. Wu and C. K. Aidun. A method for direct simulation of flexible fiber suspensions using lattice boltzmann equation with external boundary force. *International Journal of Multiphase Flow*, 36(3):202–209, 2010.

[181] J. Wu and C. K. Aidun. A numerical study of the effect of fibre stiffness on the rheology of sheared flexible fibre suspensions. *Journal of Fluid Mechanics*, 662:123, 2010.

[182] H. J. Xu and C. K. Aidun. Characteristics of fiber suspension flow in a rectangular channel. *International Journal of Multiphase Flow*, 31(3):318–336, 2005.

[183] S. Yamamoto and T. Matsuoka. A method for dynamic simulation of rigid and flexible fibers in a flow field. *The Journal of chemical physics*, 98(1):644–650, 1993.

[184] P. Yeung and S. Pope. An algorithm for tracking fluid particles in numerical simulations of homogeneous turbulence. *Journal of computational physics*, 79(2):373–416, 1988.

[185] P. Yeung and S. Pope. Lagrangian statistics from direct numerical simulations of isotropic turbulence. *Journal of Fluid Mechanics*, 207:531–586, 1989.

[186] G. Youngren and A. Acrivos. Stokes flow past a particle of arbitrary shape: a numerical method of solution. *Journal of fluid Mechanics*, 69(2):377–403, 1975.

[187] Z. Yu, N. Phan-Thien, and R. I. Tanner. Dynamic simulation of sphere motion in a vertical tube. *Journal of Fluid Mechanics*, 518:61–93, 2004.

[188] M. V. Zagarola and A. J. Smits. Mean-flow scaling of turbulent pipe flow. *Journal of Fluid Mechanics*, 373:33–79, 1998.

[189] M. Zastawny, G. Mallouppas, F. Zhao, and B. Van Wachem. Derivation of drag and lift force and torque coefficients for non-spherical particles in flows. *International Journal of Multiphase Flow*, 39:227–239, 2012.

[190] Z. Zhang and A. Prosperetti. A method for particle simulation. *Journal of Applied Mechanics*, 70(1):64–74, 2003.

[191] L. Zhao and H. I. Andersson. Why spheroids orient preferentially in near-wall turbulence. *Journal of Fluid Mechanics*, 807:221–234, 2016.

[192] L. Zhao, C. Marchioli, and H. I. Andersson. Slip velocity of rigid fibers in turbulent channel flow. *Physics of Fluids*, 26(6):063302, 2014.

[193] O. C. Zienkiewicz, R. L. Taylor, and R. L. Taylor. *The finite element method*, volume 3. McGraw-hill London, 1977.